Measurement of the single spin azimuthal asymmetry in the predominantly exclusive electroproduction of photons from the proton.

by

James H. Ely

B. A., Colorado School of Mines, 1997

A thesis submitted to the

Faculty of the Graduate School of the

University of Colorado in partial fulfillment

of the requirements for the degree of

Doctor of Philosophy

Department of Physics

2002

This thesis entitled:
Measurement of the single spin azimuthal asymmetry in the predominantly exclusive electroproduction of photons from the proton.
written by James H. Ely
has been approved for the Department of Physics

Edward R. Kinney

Professor John P. Cumalat

Associate Professor Steven J. Pollock

Date

The final copy of this thesis has been examined by the signatories, and we find that both the content and the form meet acceptable presentation standards of scholarly work in the above mentioned discipline.

Ely, James H. (Ph. D., Physics)

Measurement of the single spin azimuthal asymmetry in the predominantly exclusive electroproduction of photons from the proton.

Thesis directed by Professor Edward R. Kinney

The beam-spin asymmetry in the hard electroproduction of photons has been measured at the HERMES experiment at DESY. The data were collected in interactions from the 27.6 GeV longitudinally polarized positron beam of HERA on an unpolarized hydrogen gas target. The asymmetry in the azimuthal distribution of the photons relative to the positron scattering plane was determined with respect to the helicity of the positron beam. The beam-spin analyzing power was measured to be -0.23 ± 0.04 (stat) ± 0.04 (syst) in the nominal exclusive region. The result is attributed to the interference between the Bethe-Heitler and the deeply virtual Compton scattering processes.

Dedication

For my wife, Elena.

Acknowledgements

I could not have completed this work without the help of many people, some whom I will mention here. No man is an island, and although I contributed much to this analysis, it is by no means all my own.

I would like to thank my advisor Ed Kinney who gave me the opportunity to work on the HERMES experiment and pursue the untested DVCS analysis, which luckily proved to be a good choice. I would also like to thank the rest of my thesis committee, John Cumalat, Steve Pollock, Patricia Rankin, and Andrew Hamilton for wading through this collection of pages. Special thanks to Steve for helping with the theory chapter.

Several people helped on the DVCS analysis at HERMES. I would like to thank Moskov Amarian for initially pursuing this analysis at HERMES, I could not have come up with the idea myself. I thank Moskov also for the useful discussions and ideas along the way. For the actual analysis, I would like to thank Bryan Tipton for the use of the analysis code "dk" and Jeff Martin for showing me how to run it. Many thanks to Brendan Fox for all the invaluable help with sorting out program and analysis problems. I am especially grateful to Brendan for all the conversations about the analysis, and life in general. I would like to thank Gerard van der Steenhoven for his work on the DVCS paper, a lot of his suggestions ended up in my thesis. Finally, I would like to thank my office mate of the last few months Dave Gaskell, who has taken up the DVCS analysis, and with all his questions has made me to obtain a better grasp of all this GPD stuff.

Many thanks goes out to all the people whom I met and interacted with at DESY. There are so many, and I would hate to miss somebody, but you know who you are, and how grateful I am for all your help.

I would like to thank several people from the Nuclear Physics Laboratory, Jeff Brack, who was always helpful with any mechanical problems, Gertjan Hoffman who finished up the test beam analysis and pushed the NIM paper through, and Marc Welliver who helped me with computer problems during this last year. I would also like to thank the NPL support people, Dale Prull, who kept our computers up and running and Susan Spika, who kept all the paperwork in order.

I could not have even started on this path without the help and support of my family. Thanks so much to my parents who gave me moral support all this time, and to all my brothers and sisters, especially Finn and Monica who were around when things got tough.

Finally, I would like to thank my wife, Elena, for putting up with my pursuit of higher education. I really appreciate the support and dedication she has given me, without her I would have never finished.

Contents

Tables

Table

Figures

Figure

Chapter 1

Introduction

1.1 Probing the Structure of Nucleons

The classical way of investigating the microscopic world is by using the microscope: light is directed towards the object (a cell or microbe, for instance) we want to inspect, and by watching how the light is either reflected or transmitted by the object under study we are able to form a picture of its structure.

Unfortunately it is impossible to apply this simple technique when investigating the inner structure of the proton, since the diameter of the proton ($\sim$ 1.5 fm) is much smaller than the wavelength of visible light. The simple solution to this problem is the use of electromagnetic radiation of very small wavelength, i.e. gamma rays of 10 GeV in energy, which have a wavelength of about 0.1 fm. If such a high-energy photon is scattered off a quark - and subsequently observed in our experiment - information can be obtained about the structure of the proton. This photon scattering process is known by the name of Deeply-Virtual Compton Scattering (DVCS), and is schematically depicted in Fig. 1.1 (a).

Gamma rays of with an energy of 10 GeV or more can be generated by scattering high-energy electrons (such as the 27 GeV electrons available at the HERA electron-proton storage ring of DESY) off a proton target. However, when doing so, the detectors will mainly observe the hard bremsstrahlung gamma rays emitted by an electron, rather than the gamma rays produced in the electron-quark interaction. The emission of the bremsstrahlung gamma rays is usually referred to as the Bethe-Heitler (BH) process, which is depicted in Fig. 1.1 (b). Amidst the dominant Bethe-Heitler photons we need to observe the DVCS photons that truly scattered off the inner structures in the proton, i.e. the quarks and gluons.

For the majority of kinematic regimes which are currently accessible, the dominate photon production is from the BH process. Until recently, it was assumed that it would be close to impossible to apply the concept of photon scattering to the study of quarks and gluons in the proton.

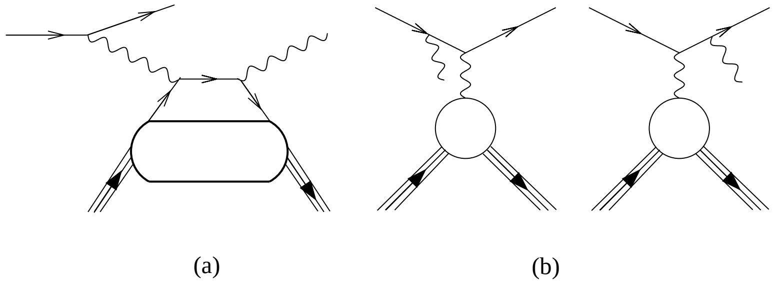

Figure 1.1: Schematic picture of single photon electroproduction from a proton. On the left-hand side (a) the deeply-virtual Compton scattering process is depicted: an electron (single line in the upper-left part of the figure) interacts with a quark (one of three lines close together) through the exchange of a (virtual) photon resulting in the subsequent emission of real photon, where the photons are represented by wiggle lines. On the right-hand side (b) the Bethe-Heitler process is shown: real photons are emitted by the incident or scattered electron in the electromagnetic field of the proton. These photons do not carry information on the quark structure of the proton. The ellipse in (a) and the circles in (b) represent complex quark rearrangements that occur in the scattering process.

However, a few years ago it was noted that the two process shown in Fig. 1.1 would quantum mechanically interfere, as all physical processes do which have the same (indistinguishable) final state. Often, interference effects are a nuisance, for example, in extracting a cross section measurement, but in this case they are a blessing. Due to the interference between the dominant BH process and the DVCS process, the DVCS contribution is more accessible, provided that an experimental observable can be identified which is exclusively sensitive to the BH-DVCS interference. Such an observable is the 'single spin azimuthal asymmetry' quoted in the title of this work. It requires that we extract the azimuthal angular dependence of photons scattered from a proton target, when a polarized positron beam is used. The azimuthal angle is the angle between the lepton plane (defined by the incident and scattered positron) and the photon plane (defined by the virtual photon - the left most curly line in Fig. 1.1 (a) - and the detected photon). The asymmetry, which is the ratio of the difference and the sum of the photon yields for the two orientations of the beam spin direction (or helicity), is shown as a function of the azimuthal angle in Fig. 1.2. A clear dependence of the asymmetry on the azimuthal angle is observed. This is a remarkable observation, as the BH process alone cannot give rise to any significant asymmetry in this plot, as will be demonstrated in chapter 2. Hence, the azimuthal dependence observed in Fig. 1.2 can only be attributed to the interference between the BH and DVCS process.

The data shown in Fig. 1.2 represent the first observation of evidence of photon (or Compton) scattering at the quark level from a beam-spin asymmetry. The scientific significance of this observation is that in due time (when more statistics over a wider kinematic range becomes available) such measurements can be used to extract information on the internal structure of the nucleon.

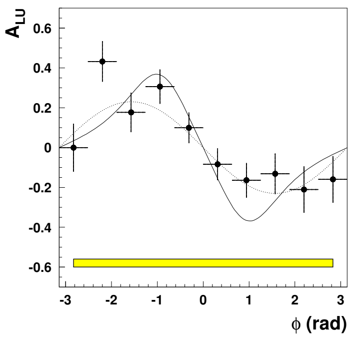

Figure 1.2: Azimuthal dependence of the asymmetry (A_{LU})of the photons produced in the experiment with respect to the orientation of the spin of the positron beam. If the photons had only originated from the Bethe-Heitler process, the azimuthal dependence would have been basically flat. However, the data show a clear $\sin(\phi)$ -type dependence, as is illustrated by the dashed curve. Such a dependence is expected if the photons originate from deeply-virtual Compton scattering, i.e. photon scattering at the quark level. The solid curve represents one of the first complete calculations of this observable [1].

1.2 Scattering

Scattering a particle off a nucleon target and detecting the final state is the primary tool to probe the inner structure of the fundamental building blocks of nature, protons and neutrons. At the beginning of the 20th century, techniques had been developed to allow direct experimental investigation of atoms. Rutherford discovered, by observing scattered α particles from a thin gold foil target, that atoms were composed mostly of empty space with a heavy point-like nucleus [2]. This type of scattering was elastic, that is, the incident particles and target nuclei remained intact, only changing their energy and momentum. Much initial information on elementary particles was obtained from elastic scattering. The electron-like particles (leptons) showed no internal structure. This point-like structure for leptons is still currently observed. However, the protons and neutrons (hadrons) which make up the nucleus of an atom are not point-like, but have an extended structure. This extended structure can be measured and parameterized in elastic scattering with functions known as form factors. The form factors are functions of a single variable, usually expressed in terms of the momentum transfer to the target. The form factors are also calculable in theoretical models and hence the structure of the nucleon can be inferred from the elastic scattering process, assuming the underlying assumptions of the models are correct.

To probe deeper into the structure of the nucleon, probes with shorter wavelengths (higher energy) are used. With higher energy probes the interaction tends to break apart the initial particles and the dominant mechanism becomes inelastic scattering. As in elastic scattering, the extended size of the nucleon is described in terms of functions, called structure functions in inelastic scattering, which are now functions of two variables, the momentum transfer and a variable describing the (in)elasticity of the interaction. With higher energy probes, it was discovered that once again the cross section could be parameterized in terms of one variable. This change in the dependence of the cross section on two variables to one variables is called scaling and is reached in the process known as deep inelastic scattering (DIS). The interpretation of the onset of scaling is that the probe is no longer scattering from the whole target nucleon, but only from a part of the nucleon. Scaling led to the development of the Quark-Parton Model (QPM), where the structure functions could be related to the interior constituents (partons or quarks) of the nucleon.

1.3 The Standard Model

Through many scattering experiments and much theoretical work a coherent theory of the fundamental forces and particles which make up our world emerged, known as the Standard Model.

In the Standard Model, matter is composed of families of quarks and leptons. Isolated quarks have not been observed; they are always confined in a quark-antiquark meson (such as a pion) or three quark baryon (such as a proton or neutron) configuration, an observation known as confinement. There are six quark flavors: u (up), d (down), c (charm), s (strange), t (top), and b (bottom) combined into three generations (u,d), (c,s), and (t,b). For each generation there is an associated lepton pair, a charged lepton and a neutral lepton (neutrino): e (electron), ν_e (electron neutrino), μ (muon), ν_μ (muon neutrino), and τ (tau), ν_τ (tau neutrino). The leptons appear to be true point particles with no structure. Along with the quarks and leptons there are the anti-quarks and anti-leptons which have opposite additive quantum numbers. For instance the anti-electron, commonly called the positron, is similar to the electron with the exception of having a positive charge (and opposite lepton number). There are four fundamental forces; strong, weak, electromagnetic and gravity forces, which initiate interactions between the fundamental particles. The gravitational force has a relatively weak coupling and has no significant contribution to the study of interactions involving the other three forces at normal energy scales. The strong, weak, and electromagnetic forces are described in the Standard Model in terms of field theories, where the forces are mediated by objects known as gauge bosons. The electromagnetic and weak forces appear as different manifestations of the same force and have been combined in an electroweak theory, the Glashow-Weinberg-Salam theory. The gauge boson of the electromagnetic force is the photon and the interaction is well described with the quantum electrodynamic field theory (QED). The weak interaction is effectively much weaker than the strong or electromagnetic interaction due to the three heavy gauge bosons; the W^+, W^-, and

Z^0 bosons (superscript represents the charge) which mediate the weak force. The electroweak theory combines the QED and weak field theories and describes the interactions of leptons and quarks. The strong interaction is described using Quantum Chromodynamics (QCD). It is similar to QED with the charges replaced by three 'colors'. The gauge bosons for QCD are called gluons (the glue which confines quarks). All known fundamental particles except quarks, antiquarks and gluons are colorless and hence are not affected by the strong force. Quarks combine together to form a resulting object which is colorless. The two simplest combinations are a pair configuration (quark, anti-quark pair or meson), where the color cancels out and a three quark combination in which the colors combine to be colorless, similar to the way red, blue, and green light combine to form white light.

Stable matter which makes up our local environment is composed of atoms, which are just different combination of protons, neutrons and electrons. Electrons are fundamental particles as far as we know, however, nucleons (protons and neutrons) are made up of the more fundamental quarks and gluons. Nucleons appear to be composed of three prominent quarks called valence quarks in a combination of (uud) for the proton and (udd) for the neutron. The quarks in addition to having color also carry charge, and therefore interact via the strong, weak and electromagnetic forces. The quarks carry a fraction of the charge of the electron with +2/3 for the up, charm, and top quarks and -1/3 for the down, strange, and bottom quarks. In addition to the quarks, there also appears to be a number of gluons in the nucleon, which serve to bind the quarks together. The gluons carry color but no charge and interact not only with quarks, but also interact strongly with each other. The composition of the nucleons is derived from experiments using techniques such as deep inelastic scattering and the Drell-Yan process.

Even though the Standard Model can describe many of the experimental observations, our understanding of the nucleon structure remains incomplete, and the predictions are often not supported. For example, in a naive picture, the nucleon is made up of three quarks (valence quarks) which move parallel to the momentum of the nucleon, and hence carry no orbital angular momentum. The total spin of the nucleon ($1/2\ \hbar$) is therefore predicted to be solely due to the sum of the spins of the quarks. However, the sum of the quark spins was experimentally shown to be much less than in the naive picture [3] an observation known as the Spin Puzzle. A more sophisticated approach is to include gluons into the model of the nucleon and allow contributions from the spin and orbital angular momenta of both the quarks and gluons to the total spin of the nucleon. The validity of this model would then be determined by the experimental data. However, the measurement of the different contributions has been experimentally challenging, and only the sum of the quarks spins has been measured with some precision. A measurement of the nucleon spin contributions, specifically the total angular momentum of the quarks, is the underlying motivation for this analysis.

1.4 Generalized Parton Distributions

Deeply inelastic scattering is used to measure structure functions which can be written in terms of the distributions of the partons which make up the nucleon as was mentioned previously. In this way, information on the partonic structure of the nucleon can be obtained. Normally DIS is inclusive scattering where only the scattered leptons are detected and all other final states are summed over. Another type of scattering is exclusive scattering, where the total final state is determined. Exclusive scattering at high energies (deep inelastic regime) can also be parameterized in terms of structure functions, which are generalizations of the structure functions used to describe the DIS process. The simplest exclusive process is elastic scattering where no new particles are produced, and is characterized by form factors. The next simplest exclusive reaction is one where a single particle is produced together with the scattered lepton and nucleon. This is inelastic exclusive scattering, as a new particle is produced, but is different from DIS since the nucleon does not break apart. The structure function for this exclusive process is a function of three variables, the momentum transfer to the nucleon, the (in)elasticity of the reaction, and the quantity of momentum transfered to the new particle (or alternatively, the amount of momentum transfered to the final state of the nucleon). Similar to the DIS process, where the structure functions can be related to the partonic structure, these generalized structure functions can also be related to the partonic structure of the nucleon via *generalized* parton distributions. The generalized parton distributions, having dependence on three variables, contain new information which is not present in the parton distributions of the DIS process.

The simplest single particle to produce in lepton-proton exclusive scattering is a real photon and the reaction is known as Deeply Virtual Compton Scattering (DVCS); the main focus of this analysis. The next simplest particle to produce in an exclusive reaction is a meson. A neutral vector meson, having the same quantum numbers as a photon, can be produced, as well as a neutral pseudo-scalar meson such as a π^0 meson. In both of these types of exclusive processes, the proton remains intact in the final state. These exclusive processes can be parameterized in terms of the same generalized parton distribution functions, that is, the generalized parton distributions are global parameters reflecting the target structure and do not depend on the reaction mechanism. When the momentum transfer to the final nucleon state reduces to zero, these generalized parton distributions lose their dependency on the momentum transfer and reduce to the parton distributions of DIS. The exclusive processes where a single new particle is produced also have a relationship to the (exclusive) elastic scattering process, which will be discussed in detail in Chapter 2. With these two relationships, the generalized parton distributions provide a link from the parton distribution functions of DIS to the elastic scattering form factors.

Another intriguing observation of the generalized parton distributions is the fact that they are sensitive to the total angular momentum of the partons in the nucleon. This sensitivity provides an unique method to measure the quark and gluon contributions to the nucleon spin. The measurement of the DVCS process, along with other exclusive processes, should allow a determination of the generalized parton distributions, which in turn will allow a measurement of the quark and gluon contributions to the nucleon spin.

1.5 Deeply Virtual Compton Scattering

Compton scattering is the elastic scattering of light (or photons) off of a target. The process of electro-magnetically scattering a lepton from a target and producing a real photon in the final state is called virtual Compton scattering, as the lepton interacts with the target via a virtual photon. Deeply virtual Compton scattering takes place in the high energy regime where the scattering is off a parton in the nucleon. DVCS is more easily interpreted directly in terms of the generalized parton distributions than meson production, as the final state photon wave function has a simpler form than a meson wave function. However, there is a similar process which has the exact final state as DVCS, that is, a scattered lepton, the recoiling proton, and a real photon. This other process is the so-called "internal" radiation process where a photon is radiated from either the initial or scattered lepton very close to the same space-time locality as the interaction and is known as the Bethe-Heitler (BH) process. The BH process is different from the DVCS process in that the radiation is not produced in the lepton-proton interaction itself and therefore carries no information about the partonic structure of the nucleon.

At most current experimental facilities, the BH process dominates over the DVCS process (as will be illustrated in chapter 2). This makes extracting the DVCS signal challenging, and in fact there have been only two direct experimental observations of the DVCS cross section up to the present date [4, 5]. In both of these observations, the BH signal is approximately the same size as the DVCS signal. The BH contribution was calculated and subtracted from the signal to yield a DVCS cross section measurement. Another approach to gain access to the DVCS process is to form an appropriate asymmetry to cancel out the dominant BH signal. An asymmetry of this type would be sensitive to the interference between the BH and DVCS processes. It will be shown that the interference between the DVCS and BH processes is dependent on the charge and also the polarization of the probe or target. These dependencies allow the formation of two asymmetries, a charge asymmetry and a spin asymmetry, which provide access to the BH-DVCS interference term. The spin asymmetry is the focus of this analysis and can, in principle, allow access to the DVCS amplitude.

This analysis used the data collected at the HERMES experiment during 1996 and 1997 to search for the DVCS process. Specifically this involved selecting reconstructed events which contained a single photon in addition to the scattered lepton. The recoiled proton was not detected due to the acceptance of the spectrometer, but was reconstructed using the invariant missing mass. The finite resolution of the spectrometer prohibits selecting truly exclusive events, therefore an "exclusive" region was formed by constraining the invariant missing mass to be between −1.5 to 1.7 GeV. The non-physical region of negative missing mass arises from the finite resolution of the calorimeter. The single photon data, constrained by various kinematic and phase space considerations, amounted to 4015 events in the selected exclusive region. The values of the kinematic variables for the selected events ranged as follows although the events are not uniformly distributed over the ranges:

$$1 < Q^2 \lesssim 10 \ \ \mathrm{GeV}^2 \,,$$
$$-2 \lesssim t \lesssim 0.5 \ \ \mathrm{GeV}^2 \,,$$
$$0.02 < x_{Bj} \lesssim 0.4 \,,$$

with average values:

$$\begin{aligned} \langle Q^2 \rangle &= 2.6 \ \mathrm{GeV}^2 \,, \\ \langle t \rangle &= -0.25 \ \mathrm{GeV}^2 \,, \\ \langle x_{Bj} \rangle &= 0.11 \,. \end{aligned}$$

Here, the positive values of t which are unphysical arise from the detector resolution. The asymmetry value in the exclusive region was estimated using the method of moments to be -0.23 ± 0.04 (stat) ± 0.04 (syst).

The photon leptoproduction analysis described in this work resulted in the first observation of an asymmetry associated with the interference between the BH and DVCS processes. This asymmetry is with respect to the spin of the probing leptons, which were positrons in this experiment. The observation of this asymmetry illustrates that the DVCS process is accessible in kinematic regions where the BH process is dominant. Chapter 2 will extend the motivation and formalism of the generalized parton distributions, the DVCS process, and the associated asymmetries, in particular the spin asymmetry. The following chapter (3) will describe the experimental setup used to collect the photon data. The extraction of the photon data from the event sample will be covered in chapter

4, as well as the extraction of the DVCS single spin asymmetry and the associated uncertainties. A discussion of the results and the implications will be the focus of chapter 5 with a short outlook to the future of the DVCS process and the generalized parton distribution functions in chapter 6.

Chapter 2

Theoretical Formalism for Generalized Parton Distributions

The framework for generalized parton distributions (GPDs) is a relatively new subject, and therefore will be introduced in terms of elastic and inelastic scattering. Dominant aspects of the GPD framework will then be discussed and the relationship to the angular momentum of the nucleon established. Several models of the GPDs will be reviewed and a calculation for the DVCS process presented, to illustrate the expectations for the experimental data. Finally, the implications of the calculation, with respect to the different angular momentum contributions of the nucleon, will be considered.

2.1 Scattering

The scattering of one particle from another is the main process used to investigate the internal structure of a nucleon. Electromagnetic scattering using a lepton probe, such as an electron or muon, is the easiest to interpret in terms of the structure of the nucleon. This is due to the fact that leptons and hadrons interact via the well understood electromagnetic interaction which can be calculated using perturbative methods. As quarks are not observed in isolation, a nucleon (or meson) target must be used in the scattering interaction and information on the quarks inferred. Elastic scattering yields information via form factors on the nucleon (or meson) as a whole, such as the charge distribution or the magnetic moment. Deep inelastic scattering (DIS) yields information on the internal structure of the nucleon (or meson) since it can be interpreted as elastic scattering on the partons (quarks) inside the hadron. The information from DIS is characterized in terms of parton distribution functions. These two types of scattering can be linked with the use of the generalized parton distribution functions.

2.1.1 Elastic Scattering

In the elastic scattering process no new particles are created; only the kinematics of the final state differ from the initial state. Using the conservation of momentum and energy, the cross section for unpolarized elastic scattering can be (mostly) described in terms of a single variable. For classical mechanics the variable of choice is the impact parameter, for nuclear physics the momentum transfer from one particle to the other is usually used. In the classical scattering experiment of Rutherford, an α particle, which is essentially a helium nucleus, was used to probe a gold atom. A predicted relationship between the (differential) cross section into a solid angle (Ω) and the angle (θ) of the scattered particle was confirmed:

$$\frac{d\sigma}{d\Omega} = \frac{\alpha^2}{4E^2 \sin^4 \frac{\theta}{2}} , \tag{2.1}$$

where $\alpha = 1/137$ is the electromagnetic coupling (fine structure constant), and E is the energy of the initial probing particle. The angle $\frac{\theta}{2}$ is related to the magnitude of the momentum transfer q by the following:

$$|q| = 2k \sin\frac{\theta}{2} , \tag{2.2}$$

where $k = |\vec{k}|$ is the magnitude of the incident probe momentum. Hence, with a probe of fixed energy $(E, \vec{k})$, the cross section is entirely described by one variable (q). Eq. 2.1 is valid only in the case of an infinitely heavy target (gold atom) and spin-less particles (such as the α particle). As technical advances were made, smaller probes and targets were used allowing the investigation of the more fundamental protons and neutrons. In these cases the above formula must be modified to include the recoil of the target and the spin of both the probe and target:

$$\frac{d\sigma}{d\Omega} = \frac{\alpha^2}{4E^2 \sin^4 \frac{\theta}{2}} \frac{E'}{E} \cos^2\frac{\theta}{2}(1 + \frac{Q^2}{2M^2} \tan^2\frac{\theta}{2}). \tag{2.3}$$

Here $E(E')$ is the energy of the initial (scattered) spin-1/2 projectile and M is the mass of the target, where the mass of the projectile is assumed negligible. Q^2 represents the magnitude of the (negative) 4-momentum transfer:

$$Q^2 = -q^2 = -(k - k')^2 > 0 , \tag{2.4}$$

with $k(k')$ being the initial (scattered) probes four-momentum. Equation 2.3 is still an approximation as it assumes that the probe and target are point-like objects and deviations from this equation appear at high energies. The light electron particles (leptons) reveal no internal structure and are still considered point-like. However, the proton and neutrons (hadrons) are not point-like, but have an extended structure. This extended structure can be parameterized in elastic scattering with functions called form factors. These form factors can also be derived in theoretical models by taking the Fourier transform of a modeled (probability) density. Hence the structure (density) of the nucleon can be inferred from the elastic scattering form factors. Since electrons are point-like particles, and interact only electromagnetically, electron-target scattering is a dominant tool used to map out the internal electromagnetic structure of the nuclei of atoms and nucleons.

2.1.2 Inelastic Scattering

In order to investigate smaller length scales in the structure of the nucleon, probes with shorter wavelengths (higher energy) are used. Higher energy probes tend to break apart the initial particles and hence inelastic scattering becomes the dominant process. Elastic scattering has only a minor contribution to the total cross section at high energies. The inelastic scattering process is parameterized by two variables, the momentum transfer q and the energy transfer of the scattered particle, or $\nu = E - E'$ (lab frame), the difference in the initial and final energies of the probe. Once again the extended size of the nucleon can be described in terms of functions, called structure functions for inelastic scattering. There are two structure functions, F_1 and F_2, which are independent of the polarization of the projectile or target (obtainable in unpolarized scattering) and two of which are sensitive to the polarization, g_1 and g_2 (obtainable in polarized scattering experiments). With higher energy probes, the nuclear interior has been more finely investigated and it was discovered that at high energy and large momentum transfers (Q^2 above 1 GeV^2) the structure functions could be parameterized in terms of just one variable. The change in the dependence of the cross section on two variables to one variable (scaling) is reached in the deep inelastic scattering (DIS) process. A simple diagram of DIS is shown in Fig. 2.1. Here, the relevant variables are the four-momenta of the incoming lepton (k), of the scattered lepton (k'), of the target nucleon (p), of the final state (p'). The four-momentum of the virtual photon is given by $q = k - k$', with q, k, and k' representing four vectors. In DIS the scaling variable Bjorken x (x_{Bj}) becomes the single degree of freedom and is defined as:

$$x_{Bj} \equiv \frac{Q^2}{2M\nu}. \tag{2.5}$$

At high values of Q^2 the structure functions display scaling violations, and are actually functions of two variables (usually x_{Bj} and Q^2). This scaling violation can be parameterized, allowing access to more information on the gluonic structure of the nucleon contained in the structure functions.

In deep inelastic scattering, the leading order diagram in the Bjorken limit has been shown to be factorizable into two parts, a process known as factorization. The first part of the interaction is the hard scattering of the virtual photon (from the lepton) off of a parton in the nucleon and occurs on a relatively short time scale. The second part of the interaction involves the breaking apart and recombination of the partons into real particles in a process known as fragmentation. This second

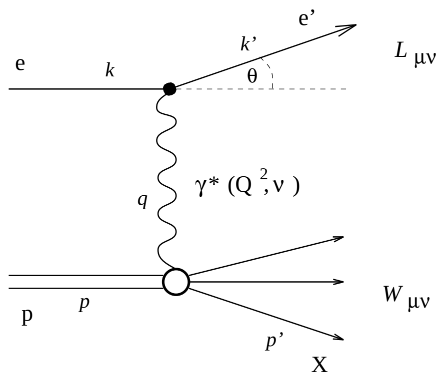

Figure 2.1: Deep inelastic electron proton scattering in the lowest order in QED.

part occurs on a much longer time scale than does the hard scattering, and therefore the parts can be viewed as distinct, allowing a factored form for the cross section. A simple diagram illustrating the two distinct parts of the leading order DIS process is shown in Fig. 2.1. Factorization is proven only in the extreme limit where the momentum transfer Q^2 and the virtual photon energy ν become infinite, but with the ratio of Q^2 to ν finite. However, the structure functions have little Q^2 dependence at moderate x_{Bj}, indicating the validity of factorization at experimental DIS regimes.

Four independent structure functions arise in the inelastic lepton-nucleon scattering formalism. For this illustration the scattering of an electron (or positron) off of a nucleon will be used. The mass of the lepton will be ignored, and the mass of the nucleon denoted as M. The spin 1/2 nature of both particles will be used; reactions involving particles with different spin will require a different formalism. The differential scattering cross section in terms of the leptonic $L^{\mu\nu}$ and hadronic $W^{\mu\nu}$ tensors can be expressed as:

$$\frac{d^2\sigma}{d\Omega dE'} = \frac{\alpha^2 E'}{Q^4 E} L^{\mu\nu} W_{\mu\nu} \,, \tag{2.6}$$

where $\alpha = 1/137$ is the fine structure constant. Here E (E') are the initial (scattered) lepton energies as before and the cross section is differential in the energy and in the solid angle (Ω) of the scattered lepton. The leptonic tensor $L^{\mu\nu}$ can be calculated due to the point-like nature of leptons (and QED) according to the Feynman rules as:

$$L^{\mu\nu} = \sum_{s_l'} \left[\bar{u}(k', s_l')\gamma^\mu u(k, s_l)\right] \cdot \left[u(k', s_l')\gamma^\nu \bar{u}(k, s_l)\right]^* \,, \tag{2.7}$$

here the spin (polarization) of the final states is summed over as it is not usually detected. The usual four-component spinor $u(k, s_l)$ notation is used to describe particle states with four momentum k and spin s_l. The sum over the final spins reduces the lepton tensor to a trace which can be reduced with trace theorems to:

$$L^{\mu\nu} = 2[k^{'\mu}k^{\nu} + k^{\mu}k^{'\nu} - k \cdot k^{'} g^{\mu\nu} - i\epsilon^{\mu\nu\alpha\beta} q_{\alpha} s_{l\beta}] \,, \tag{2.8}$$

where $s_{l\beta}$ is the spin four-vector of the initial lepton defined as:

$$s_l^{\mu} = \frac{1}{2}\bar{u}(k, s_l)\gamma^{\mu}\gamma_5 u(k, s_l) \,, \tag{2.9}$$

and $\epsilon^{\mu\nu\alpha\beta}$ is the totally anti-symmetric Levi-Civita tensor.

The hadronic tensor $W^{\mu\nu}$ cannot be calculated from first principles due to the extended hadronic structure, but must be parameterized in terms of functions. Symmetry arguments, gauge invariance, and conservation laws of QED allow the reduction of the tensor to four independent real functions W_1, W_2, G_1, and G_2, which are dependent on the two DIS variables x_{Bj} and Q^2. The functions W_1 and W_2 do not depend on the hadron's spin, while G_1 and G_2 are sensitive to the polarization of the hadron. The tensor can be expressed as:

$$\begin{aligned} W_{\mu\nu} &= W_1(Q^2, \nu)(-g_{\mu\nu} + \frac{q_{\mu}q_{\nu}}{q^2}) \\ &+ \frac{W_2(Q^2, \nu)}{M^2}(p_{\mu} - \frac{p \cdot q}{q^2}q_{\mu})(p_{\nu} - \frac{p \cdot q}{q^2}q_{\nu}) \\ &+ G_1(Q^2, \nu)Mi\epsilon_{\mu\nu\lambda\sigma}q^{\lambda}s_h^{\sigma} \\ &+ \frac{G_2(Q^2, \nu)}{M}i\epsilon_{\mu\nu\lambda\sigma}q^{\lambda}(p \cdot q s_h^{\sigma} - s_h \cdot q p^{\sigma}). \end{aligned} \tag{2.10}$$

Here, M is the hadronic mass, $g_{\mu\nu}$ is the metric tensor and q (p) represent the virtual photon (hadron) 4-momentum. The vector s_h represents the (axial) polarization vector of a spin-1/2 hadron. The four functions are made dimensionless using the following equations, resulting in the usual form of the structure functions:

$$F_1(x_{Bj}, Q^2) = MW_1(Q^2, \nu) \,, \tag{2.11}$$

$$F_2(x_{Bj}, Q^2) = \nu W_2(Q^2, \nu) \,, \tag{2.12}$$

$$g_1(x_{Bj}, Q^2) = M^2\nu G_1(Q^2, \nu) \,, \tag{2.13}$$

$$g_2(x_{Bj}, Q^2) = M\nu^2 G_2(Q^2, \nu) \,. \tag{2.14}$$

The interpretation of the onset of scaling, where the cross section can be written as a singled-variable function, is that the probe is no longer scattering from the whole target nucleon, but only elastically scattering off of a part of (or parton in) the nucleon. The discovery of a partonic sub-structure of the nucleon led to the formation of the Quark-Parton Model (QPM), which is described in many textbooks, see for example Ref. [6]. In the simple parton model, where the momentum transfer is large enough that scaling has set in, the structure functions are functions of one variable (x_{Bj}) and can be related to the distribution functions of the partons or quarks inside the nucleon:

$$\begin{aligned} F_1(x_{Bj}) &= \frac{1}{2}\sum_q e_q^2\, q(x_{Bj})\,, \\ F_2(x_{Bj}) &= \sum_q e_q^2\, x_{Bj}\, q(x_{Bj})\,, \end{aligned} \tag{2.15}$$

where $q(x_{Bj})$ represents the parton distribution function, and the sum is over the quark flavor q, weighted by the respective quark charge e_q. The parton distribution function is interpreted in this model as the probability to find a parton of momentum fraction x_{Bj} in the nucleon. The relations of Eq. 2.15 were derived from the observation that the structure functions for spin 1/2 particles appear related, a phenomena known as the Callan-Gross Relation:

$$F_2(x_{Bj}) = 2\; x_{Bj}\; F_1(x_{Bj}). \tag{2.16}$$

There are slight deviations from the Callan-Gross relation, which however are not important for this discussion. The spin dependent structure functions also can be written in terms of spin dependent quark distribution functions:

$$g_1(x_{Bj}) = \frac{1}{2}\sum_q e_q^2 \Delta q(x_{Bj})\,, \tag{2.17}$$

$$g_2(x_{Bj}) = 0\,, \tag{2.18}$$

where $\Delta q(x_{Bj})$ is the difference in the quark distribution functions with the quark spin parallel and anti-parallel to the nucleon spin.

To form a complete structure function for a nucleon, a sum over the various quark contributions is made. This includes the three valence quarks as well as the contributions from the gluons which appear as sea quarks (pairs of quarks and anti-quarks). The explicit structure function for the proton $F_2^p(x_{Bj})$ is for example:

$$\begin{aligned} &F_2^p(x_{Bj}) = \\ &x_{Bj}\left[\frac{4}{9}u(x_{Bj}) + \frac{1}{9}d(x_{Bj}) + \frac{1}{9}s(x_{Bj}) + \frac{4}{9}\bar{u}(x_{Bj}) + \frac{1}{9}\bar{d}(x_{Bj}) + \frac{1}{9}\bar{s}(x_{Bj})\right]\,, \end{aligned} \tag{2.19}$$

where the contribution to the sea quarks from heavier quark flavors c, b, and t have been neglected assuming moderate interaction energies.

Shown in Fig. 2.2 are the available world data on the structure functions F_1^p and g_1^p along with a next-to-leading order (NLO) QCD parameterization. The unpolarized structure function has been well mapped out in the two variables x_{Bj} and Q^2 and the polarized structure function g_1^p is beginning to be well mapped also.

The DIS cross section can be calculated from the parameterizations of the parton distributions, however, a theoretical calculation can be made without the parton distributions. The formalism of this calculation is instructive for exclusive processes in that it illustrates the connection of the DIS process to Compton scattering. In order to calculate the theoretical cross section for DIS, a sum of the calculated cross section for each possible final state must be made. Since it would be virtually impossible to calculate all of the possible final states in DIS, another method is incorporated to circumvent the infinite sum. The optical theorem states that the leading DIS process of a single virtual photon exchange can be viewed as being identical to the elastic scattering of a virtual photon from the proton at zero degrees. This scattering, commonly known as the forward Compton scattering process, is the same as a DIS process with its mirrored process (ie, multiple states combining into a single lepton and proton) as shown in Fig. 2.3. A calculation of DIS can then be accomplished using the forward Compton process with its single final state. Although a sum over many possible intermediate states still exists in forward Compton scattering, the intermediate states are all virtual. Therefore, an approximation can be used to calculate the sum (or the sum can be truncated), which is not possible if all the final states are real as in the DIS process. The forward Compton scattering amplitude is calculated relatively easily compared to the infinite sum required in the DIS calculation. At zero degree scattering (or the forward scattering limit) the Compton scattering cross section can be related to the DIS cross section via the optical theorem (see Fig. 2.4). The optical theorem relates a total cross section to the imaginary part of the forward amplitude of a scattering process:

$$\mathrm{Im}\ \ f(\theta = 0) = \frac{q\ \sigma_{\mathrm{total}}}{4\pi}\,, \tag{2.20}$$

with q representing the magnitude of the (three) momentum involved in the process. The optical theorem is used to relate the forward Compton amplitude (f_{Compton}) to the total DIS cross section (σ_{DIS});

$$\mathrm{Im}\ \ f_{\mathrm{Compton}}(\theta = 0) = \frac{q\ \sigma_{\mathrm{DIS}}}{4\pi}\,, \tag{2.21}$$

where now q represents the magnitude of the virtual photon (three) momentum. The relationship not only allows a way to calculate the total cross section for the DIS process, it also implies that the forward Compton process can be described in terms of parton distribution functions similar to the DIS process. This illustrates the connection of the DIS parton distributions to the generalized parton distributions, which describe the Compton process at non-zero scattering angles.

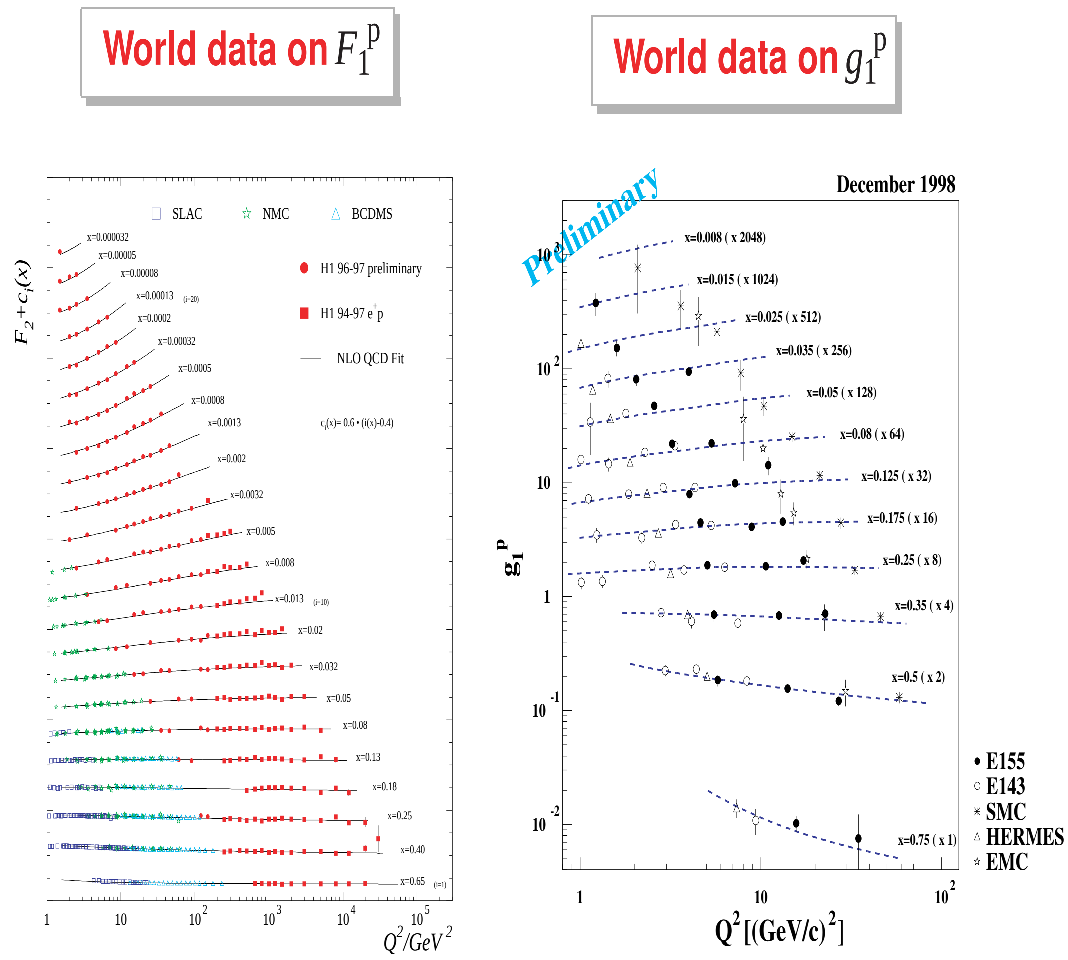

Figure 2.2: World data on spin-average and spin-dependent structure functions from Ref. [7].

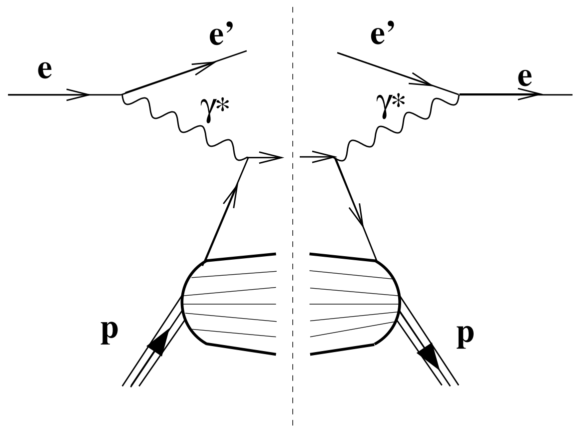

Figure 2.3: A diagram showing the DIS process, along with a mirror DIS process.

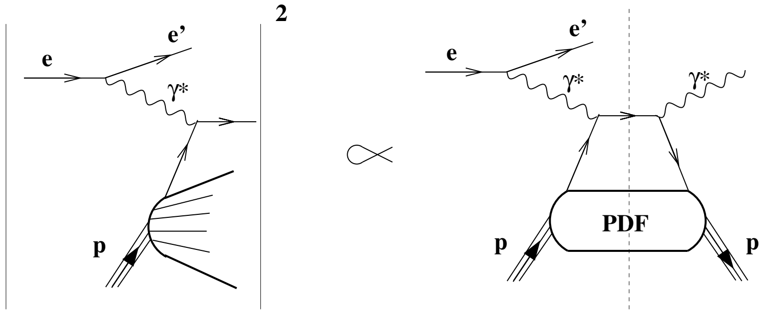

Figure 2.4: The DIS and forward Compton diagrams which are related through the optical theorem.

2.2 Generalized Parton Distributions

Since the DIS process is related to the imaginary part of the *forward* Compton amplitude and provides information on the structure of the nucleon, the question naturally arises: can new information be learned from the the non-forward part of the Compton amplitude? To answer this question, an investigation of the non-forward Compton processes is needed. These non-forward Compton processes must be in the same deep inelastic regime as DIS, in order to access the internal structure of the nucleon. The types of processes involving a non-forward Compton-like amplitude which can be identified experimentally are exclusive processes where a single observed particle is produced in conjunction with the target nucleon (total final state reconstructed). For a non-forward Compton-like scattering process the produced (and detected) particle is either a real photon or a meson. A real photon is the simplest final state to produce with the virtual photon becoming on-shell in the interaction (DVCS). A vector meson, having the same quantum numbers as the photon, can be created from a fluctuation of the virtual photon allowed by the Heisenberg uncertainty principle. The production of pseudo-scalar mesons can also be described in the same non-forward Compton-like scattering framework. The formalism for DVCS and exclusive meson production involves a Compton-like amplitude, therefore in analogy with DIS, parton distributions are used to parameterize the non-perturbative part of the interaction in the non-forward region. These parton distributions have an extra degree of freedom and therefore are generalizations of the standard parton distributions used in DIS and hence are known as Generalized Parton Distributions (GPD).

In addition to the generalized parton distributions of the non-forward Compton scattering processes, other sets of GPDs can be defined for the case where the final state differs from a nucleon. The GPDs which can describe these process are similar but distinct from the GPDs describing non-forward

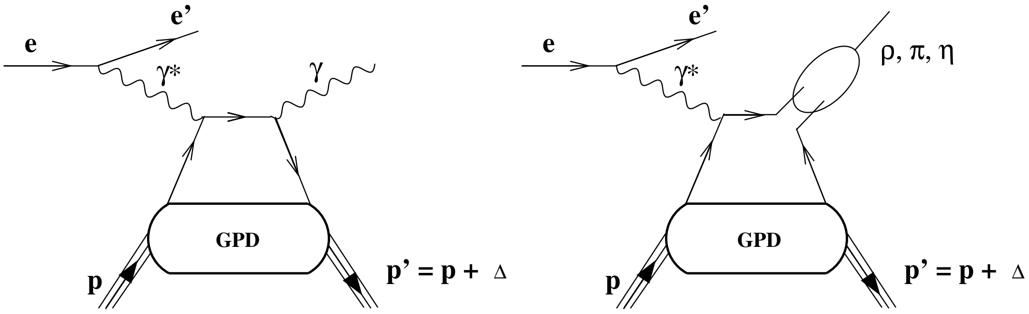

Figure 2.5: The handbag diagrams for DVCS (left figure) and exclusive meson production (right figure).

Compton processes. These interactions include

$$\begin{aligned} N &\rightarrow \Delta\,, \\ N &\rightarrow \Lambda, \Sigma\,, \\ N &\rightarrow \pi N. \end{aligned}$$

The last interaction is a semi-exclusive reaction, where the final state of the target is more than one particle, and could be used to investigate the mechanism responsible for chiral symmetry breaking [8].

For the forward Compton scattering process, there is no momentum transfer to the final state nucleon, that is, the virtual photon and proton have the same magnitude of momentum in the initial and final states. In the non-forward regime, however, some momentum transfer to the outgoing particles is required, typically characterized by the Mandelstam invariant $t = (p - p')^2$, the squared difference in the initial and final state nucleon four-momenta. Often the variable Δ is used, defined by $\Delta = (p' - p)$ or $\Delta^2 = -t$.

As in DIS, exclusive processes can be factored into two sub-processes, the hard scattering of the virtual photon from a parton, and the emission and reabsorption of the parton in the nucleon. This picture is only valid in the Bjorken limit as in DIS, where the kinematic variables Q^2 and ν become infinite, while the ratio $x_{Bj} = Q^2/2M\nu$ remains finite. Recently, factorization of the deeply virtual Compton scattering process in leading twist and exclusive meson production (from longitudinal virtual photons) has been proven in the Bjorken limit [9–12]. The factorization into two parts can be pictorially represented by handbag Feynman diagrams. Two types of exclusive handbag diagrams, for DVCS and exclusive meson production, are shown in Fig. 2.5. For the following discussion, the formalism if Ji will be used where a particular gauge choice is made which allows for a less complicated formalism [13]. Factorization leads to a product equation for the scattering tensor $T^{\mu\nu}$ of the hard scattering process with a process describing the non-perturbative parton emission from, and reabsorption to, the nucleon. For example, using the handbag diagram of DVCS for scattering off a quark, the virtual photon-nucleon scattering matrix can be written as:

$$T^{\mu\nu} = i \int \frac{d^4k}{(2\pi)^4} \,\mathrm{Tr}\left(\left[\gamma^\nu \frac{i}{\not k - \not\Delta + \not q + i\epsilon}\gamma^\mu + \gamma^\mu \frac{i}{\not k + \not\Delta - \not q + i\epsilon}\gamma^\nu\right] M(k)\right) . \tag{2.22}$$

The lepton part of the interaction will be omitted for the following description and the variable k will be used to represent the active quark momentum. The polarization indices of the virtual and real photons are μ and ν respectively and are connected by quark propagators in the description of the hard scattering part. $M(k)$ is the quark density matrix between two quark states with different momentum (p or p'),

$$M(k) = \int e^{ikz} \, d^4z \, \langle p'|\bar{\psi}_q(-z/2) \; \mathcal{O} \; \psi_q(z/2)|p\rangle \ , \tag{2.23}$$

here z is the relative coordinate between the space-time vertices of the propagator, k represents the momentum of the active quark and ψ_q represents the quark field of flavor q. The operator $\mathcal{O}$ represents a generic operator which is γ^μ for helicity independent scattering or $\gamma^\mu\gamma^5$ for the helicity dependent case.

The quark density matrix is often transformed to a simpler form by introducing the factor $\int dx(d\lambda/2\pi)e^{i\lambda(x-k\cdot n)} = 1$ and integrating over k^μ and z^μ. This results in a quark density matrix as a function of x, the momentum fraction of the active quark:

$$M(x) = \int e^{i\lambda x} \, \frac{d\lambda}{2\pi} \, \langle p'|\bar{\psi}_q(-\lambda/2) \; \mathcal{O} \; \psi_q(\lambda/2)|p\rangle \ . \tag{2.24}$$

The forward Compton amplitude, used to calculate the DIS process, is the limiting case of Eq. 2.23 when $p' = p$. For example, the forward matrix elements in the quark helicity averaged (unpolarized) case have the form:

$$\begin{aligned} &\langle p \mid \bar{\psi}_q(-\lambda/2)\gamma \cdot \lambda\psi_q(\lambda/2) \mid p\rangle \\ &\qquad = \bar{u}(p)\gamma \cdot \lambda u(p) \int_{-1}^{1} e^{-i\lambda x}\tilde{q}(x)\, dx \, + O(\lambda^2) \, , \end{aligned} \tag{2.25}$$

where $\tilde{q}(x)$ is a generic function representing both the quark and anti-quark momentum distribution and u and $\bar{u}$ represent nucleon spinors. When the momentum fraction x is greater than 0, the distribution function $\tilde{q}(x)$ coincides with the usual quark distribution $q(x)$ of quark flavor q. For negative momentum fractions ($x < 0$) the distribution function $\tilde{q}(x)$ customarily represents the (negative) antiquark distribution $-\bar{q}(-x)$. The non-leading $O(\lambda^2)$ terms in the Eq. 2.25 represent the additional terms which arise when the scattering is not in the Bjorken limit, often written equivalently in orders

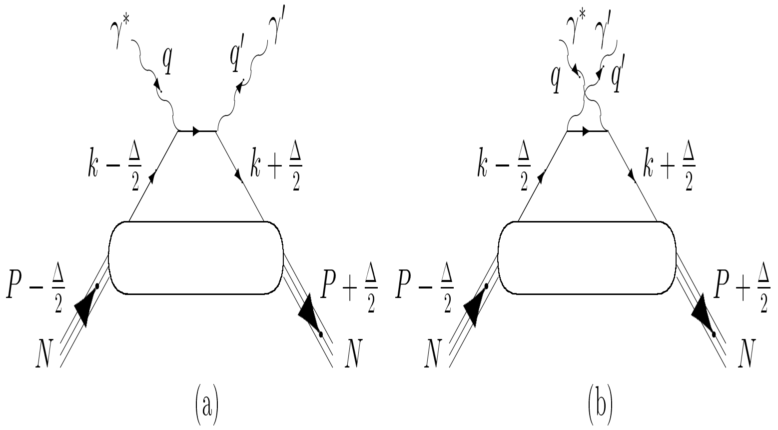

Figure 2.6: "Handbag" diagrams for DVCS.

of $1/Q^2$, as the length scale is related to the inverse of the energy scale. Normally in DIS, the q-flavored quark and antiquark distributions are defined by

$$\begin{aligned}&\langle p \mid \bar{\psi}_q(-\lambda/2)\gamma\cdot\lambda\psi_q(\lambda/2)\mid p\rangle\\ &\quad = \bar{u}(p)\gamma\cdot\lambda u(p)\int_0^1 \left(e^{-i\lambda x}q(x) - e^{i\lambda x}\bar{q}(x)\right)\, dx \,+ O(\lambda^2),\end{aligned} \tag{2.26}$$

with separate integrals over the positive interval $[0,1]$. For the non-forward case, the general definition (as in Eq. 2.25) is used to maintain a more compact formalism.

For the DVCS process there are two leading order handbag diagrams which describe the two ways the photons can couple to the struck quark (see Fig. 2.6). Here, the average nucleon momentum ($P = (p+p')/2 = p+\Delta/2$) notation is used to take advantage of a symmetric description. The virtual (real) photon is denoted with γ^* (γ') with 4-momentum q (q'), and the struck quark in this notation has an initial (final) momentum of $k-\Delta/2$ ($k+\Delta/2$). The average quark momentum is then denoted by the k variable.

It is convenient to define the non-forward matrix elements in the so-called light-cone coordinates in the infinite momentum frame. The expansion of the interaction in terms of light-cone operators is convenient as factorization is well defined and evolution equations (discussed later) are more easily derived [10, 14]. Following the formalism of Ji [13] and choosing the virtual photon and the average nucleon momenta to be collinear and along the z-direction, the kinematics can be transformed to two light-like four vectors $p^\mu = (p^+, 0, 0, p^+)$ and $n^\mu = \frac{1}{2p^+}(1, 0, 0, -1)$ with $p^2 = n^2 = 0$ and $p \cdot n = 1$. The transformation to the light cone variables p^μ, n^μ and transverse vectors, proceeds for the DVCS process as:

$$
\begin{aligned}
P^\mu &= p^\mu + \frac{M^2 - t/4}{2} n^\mu , &(2.27)\\
q^\mu &= -\xi p^\mu + \frac{Q^2}{2\xi} n^\mu , &(2.28)\\
\Delta^\mu &= -2\xi p^\mu + \xi(M^2 - t/4)n^\mu) + \Delta_\perp^\mu, &(2.29)
\end{aligned}
$$

where M is the mass of the target nucleon (assumed the same for the initial and final states). The variable ξ is defined as the momentum transfer of the virtual photon to the nucleon in the longitudinal direction ($\xi \equiv -n \cdot \Delta/2$) with the momentum transfer in the transverse direction represented by $\Delta_\perp^\mu$. Note that the variable ξ is not present in DIS, when $\Delta = 0$, but is an important part of the DVCS formalism.

In the light-cone nomenclature, the momentum fraction of the active quark is represented by the variable x, defined as $k^+ = xP^+$, which becomes equivalent to x_{Bj} in the Bjorken limit. For the non-forward processes, the light-cone momentum fraction x does not equal x_{Bj} (in the Bjorken limit) due to the non-zero momentum transfer to the final nucleon. The struck quark may initially have a momentum fraction x but returns to the nucleon with an extra momentum fraction in the longitudinal direction (unless $\xi = 0$). This results in two momentum fractions for non-forward processes, initial and final, different from the DIS process of only one momentum fraction. This fact complicates the naive picture since the generalized parton distributions can no longer be interpreted as the simple probabilities of quark momentum fractions in the nucleon (due to the two choices). Although the variable x in both the DIS and DVCS processes represents the light-cone momentum fraction, the Bjorken limit is not equivalent. As this theoretical discussion is, for the most part, assumed to be in the Bjorken limit, the variable x_{Bj} will be used to describe the momentum fraction x for forward DIS-type processes whenever there might be a possibility of confusion, leaving x to describe the momentum fraction for non-forward processes.

The light cone decomposition simplifies when considering the Bjorken limit ($Q^2 \to \infty$) where the + components of P^μ and Δ^μ are much larger than the minus or transverse components (which are neglected):

$$
\begin{aligned}
P^\mu &\sim p^\mu, &(2.30)\\
q^\mu &= -\xi p^\mu + \frac{Q^2}{2\xi} n^\mu , &(2.31)\\
\Delta^\mu &\sim -2\xi p^\mu. &(2.32)
\end{aligned}
$$

The parameter ξ in the Bjorken limit becomes the coefficient of proportionality ($\xi = -\Delta^+/2P^+$) between the plus components of the momentum transfer and the average hadron momentum. It

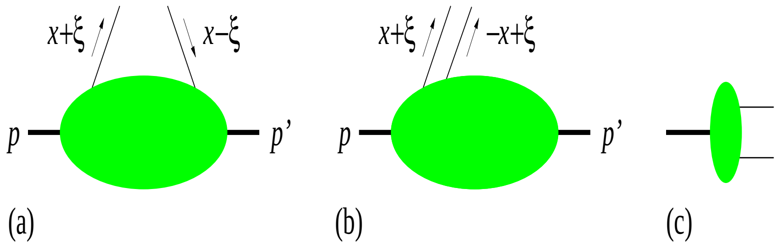

Figure 2.7: Feynman diagrams illustrating the different kinematic regimes. (a) The kinematic regime where a generalized parton distribution describes the emission and re-absorption of a parton. (b) The regime where it describes the emission of a quark-antiquark or gluon pair. This is reminiscent of a meson distribution amplitude, shown in (c).

therefore specifies a *skewedness* of the matrix elements and the GPDs are sometimes referred to as Skewed Parton Distributions (SPD). With this representation in the Bjorken limit, the initial and final nucleons have longitudinal momenta $(1+\xi)p^{\mu}$ and $(1-\xi)p^{\mu}$. The initial and final momentum of the struck quark is $(x+\xi)p^{\mu}$ and $(x-\xi)p^{\mu}$, respectively. The struck quark has different momentum in the initial and final states, but must be reabsorbed in an exclusive process to produce the nucleon final state. The generalized parton distributions therefore represent the correlation or wave function overlap between quarks of different momenta. Since there is a non-zero momentum transfer in the longitudinal direction, the GPDs can not be interpreted as momentum densities in the Bjorken limit in analogy to the parton distributions. Rather, the GPDs represent a probability amplitude for finding a quark with momentum fraction $x+\xi$ in the nucleon, and replacing it with a $x-\xi$ momentum fraction quark. The momentum density interpretation however, regains validity in the limit of $\xi = 0$, when the momentum transfer is solely in the transverse direction [15].

The constraint on the momentum fraction x is

$$-1 < x < 1\,, \tag{2.33}$$

as the quarks can not have longitudinal momentum greater than the parent nucleon. When $x > \xi$ both quark propagators in the Feynman diagram represent quarks. When $x < -\xi$ they represent antiquarks. In these two regions, the generalized parton distributions which describe the soft subprocess of the interaction behave in a similar fashion as the usual parton distributions. In the intermediate region, $-\xi < x < \xi$, the quark propagators represent one quark and one antiquark, and here the GPDs resemble a meson ($q\bar{q}$ pair) wave function amplitude. The different GPD regimes are illustrated in Fig. 2.7. The GPDs act like the usual parton distributions $q(x)$ as the momentum flow in the t channel approaches zero (forward limit where $\Delta = 0$). On the other hand when the interaction proceeds mainly via the t channel, the matrix elements act more like meson distribution amplitudes; the probability to find the meson in a quark-antiquark state.

The meson distribution amplitude is usually written in terms of the function $\phi(\alpha)$, where α represents the difference in the momentum fractions of the meson carried by the quark f_q and antiquark $f_{\bar{q}}$:

$$\begin{aligned} 1 &= f_q + f_{\bar{q}}\,, \\ f_q - f_{\bar{q}} &= \alpha\,. \end{aligned} \tag{2.34}$$

The GPDs are therefore most easily represented as a convolution of the parton distributions and meson distribution amplitudes.

The non-forward Compton scattering matrix elements can be expressed in terms of generalized parton distributions. In DVCS, for a spin-1/2 target, there are 12 independent kinematic functions [16]. This follows from a simple consideration of the allowed polarization of the states; 3 (virtual photon) x 2 (final photon) x 2 (initial nucleon) x 2 (final nucleon) x 1/2 (parity invariance). In the leading twist approximation, the virtual photons are purely transverse. Working in leading twist reduces the number from 12 to 8 independent structures. For transverse virtual photons, the dominant process is where the initial and final photon helicity are the same. The photon spin flip amplitudes contribute as higher order corrections and are suppressed by $1/Q^2$ compared to the leading amplitudes (to be discussed in Section 2.5.1). Neglecting the photon spin flip amplitude further reduces the number of independent functions to 4. Ji represents these four kinematic structures (for quarks of flavor q) in the GPD framework using quarks spinor representation [13]:

$$\begin{aligned} \int \frac{d\lambda}{2\pi} e^{i\lambda x} \langle P + \frac{\Delta}{2} | \overline{\psi}_q(-\lambda/2)\gamma^\mu \psi_q(\lambda/2) | P - \frac{\Delta}{2} \rangle \\ = H_q(x,\xi,t)\ \overline{u}(P+\frac{\Delta}{2})\gamma^\mu u(P-\frac{\Delta}{2}) \\ + E_q(x,\xi,t)\ \overline{u}(P+\frac{\Delta}{2})\frac{i\sigma^{\mu\nu}\Delta_\nu}{2M} u(P-\frac{\Delta}{2}) \\ + \cdots\ , \end{aligned} \tag{2.35}$$

$$\begin{aligned} \int \frac{d\lambda}{2\pi} e^{i\lambda x} \langle P + \frac{\Delta}{2} | \overline{\psi}_q(-\lambda/2)\gamma^\mu \gamma_5 \psi_q(\lambda/2) | P - \frac{\Delta}{2} \rangle \\ = \widetilde{H}_q(x,\xi,t)\ \overline{u}(P+\frac{\Delta}{2})\gamma^\mu \gamma_5 u(P-\frac{\Delta}{2}) \\ + \widetilde{E}_q(x,\xi,t)\ \overline{u}(P+\frac{\Delta}{2})\frac{\Delta^\mu \gamma_5}{2M} u(P-\frac{\Delta}{2}) \\ + \cdots\ , \end{aligned} \tag{2.36}$$

here the $\overline{u}()$ and $u()$ represent the nucleon spinors and the dots $(\cdots)$ denote higher-twist contributions which have been neglected. The chiral-even distributions H and $\widetilde{H}$ describe processes where the nucleon helicity is conserved, while the chiral-odd distributions E and $\widetilde{E}$ arise from the nucleon helicity flip process allowed by the finite momentum transfer. Similar equations exist for the gluon GPDs H_g, E_g, $\widetilde{H}_g$, and $\widetilde{E}_g$. For each type (flavor) of struck parton (quark or gluon), there are four independent GPDs, and as in DIS, the distribution for the nucleon can be obtained with a sum over the various parton distributions.

2.2.1 GPD Relationships and Constraints

There are several interesting characteristics of the GPDs which have been demonstrated by Ji which can help to limit the potential model functions. The GPDs have been shown to be even functions of ξ due to hermicity and time-reversal invariance considerations [13,17]. For example, the GPD $H(x,\xi,t)$ is equal using postive and negative values of ξ (of the same magnitude):

$$H(x,\xi,t) = H(x,-\xi,t). \tag{2.37}$$

Lorentz invariance of the nucleon matrix elements results in a relationship of the moments (with respect to x) of the GPDs and polynomials in ξ [13].

$$\begin{aligned} \int_{-1}^{1} dx\ x^N\ H_q(x,\xi,t) &= h_0^q + h_2^q\ \xi^2 + \ldots + h_{N+1}^q\ \xi^{N+1}\,, \\ \int_{-1}^{1} dx\ x^N\ E_q(x,\xi,t) &= e_0^q + \tilde{e}_2^q\ \xi^2 + \ldots + e_{N+1}^q\ \xi^{N+1}\,. \end{aligned} \tag{2.38}$$

here the functions h_i^q and e_i^q (not to be confused with the quark charge) are functions of the momentum transfer t. The polynomials on the left hand side of Eq. 2.38 only contain even powers of the skewedness ξ due to time-reversal invariance, therefore the last term in the polynomial ($\propto \xi^{N+1}$) only contributes in the odd-N moments of x. For the helicity dependent functions $\widetilde{H}(x,\xi,t)$ and $\widetilde{E}(x,\xi,t)$, the polynomial conditions are similar to the helicity independent case, with the exception that the highest power of the polynomial in ξ is of order N and not $N+1$.

The coefficients in front of the $N+1$ power of ξ for the odd moments of H^q and E^q have been shown to be related to each other due to the spin 1/2 nature of the nucleon [13,18]:

$$e_{N+1}^q = -h_{N+1}^q\,. \tag{2.39}$$

The polynomial conditions Eqs. 2.38 restrict the allowed class of functions for the GPDs.

The generalized parton distributions depend on the momentum transfer (t) to the nucleon final state. The elastic form factors are also dependent on t, and in fact, there is a relatively simple connection between the two. The GPDs are related to the Dirac, Pauli, axial and pseudo-scalar elastic form factors by the integrals [19];

$$\sum_q e_q \int_{-1}^{1} H_q(x,\xi,t)\, dx = F_1(t)\,, \tag{2.40}$$

$$\sum_q e_q \int_{-1}^{1} E_q(x,\xi,t)\, dx = F_2(t)\,, \tag{2.41}$$

$$\sum_q e_q \int_{-1}^{1} \widetilde{H}_q(x,\xi,t)\, dx = G_A(t)\,, \tag{2.42}$$

$$\sum_q e_q \int_{-1}^{1} \widetilde{E}_q(x,\xi,t)\, dx = G_P(t)\,, \tag{2.43}$$

where the sum is over the quark flavors and e_q is the charge of the relevant quark. Although the GPDs depend on the variable ξ, this dependence disappears in the integral over x as illustrated by the polynomial conditions of Eqs. 2.38. For example, the last sum

$$\sum_q e_q \int_{-1}^{1} \widetilde{E}_q(x,\xi,t)\, dx = G_P(t)\,, \tag{2.44}$$

can be written as the zeroth moment (N=0) over x which contributes only one polynomial term of $\xi^0 = 1$ power;

$$\sum_q e_q \int_{-1}^{1} \widetilde{E}_q(x,\xi,t)\, x^0\, dx = e_0^q(t)\,, \tag{2.45}$$

here, the charge of the quark e_q is not to be confused with the function $e_0^q(t)$.

The E and $\widetilde{E}$ functions have explicit Δ dependence in the parameterization of the non-forward matrix element:

$$\langle p'|\bar{\psi}\gamma_\mu\psi|p\rangle \sim \bar{u}(p')\gamma_\mu u(p) H + \frac{1}{2M}\bar{u}(p')\sigma_{\mu\nu}\Delta^\nu u(p) E\,, \tag{2.46}$$

$$\langle p'|\bar{\psi}\gamma_\mu\gamma_5\psi|p\rangle \sim \bar{u}(p')\gamma_\mu u(p) \widetilde{H} + \frac{\Delta_\mu}{2M}\bar{u}(p') u(p) \widetilde{E}\;. \tag{2.47}$$

The Δ dependence renders the E and $\widetilde{E}$ functions invisible in deep inelastic scattering processes ($\Delta = 0$). However, the $t = 0,\ \xi = 0$ limit of the E distributions does exist,

$$E_q(x,\xi = 0, t = 0) \;\equiv\; e_q(x)\,, \tag{2.48}$$

$$\widetilde{E}_q(x,\xi = 0, t = 0) \;\equiv\; \tilde{e}_q(x)\,, \tag{2.49}$$

where $e_q(x)$ and $\tilde{e}_q(x)$ are the forward limits of the functions E and $\widetilde{E}$. These function are not to be confused with the polynomial coefficients (functions of t) in Eq 2.38! In particular, for $t = 0$ the integral over E_q results in the anomalous magnetic moment $G_P(t = 0)$ (see Eq. 2.43). These limits for the E and $\widetilde{E}$ distributions can be useful in constraining potential GPD models in a similar fashion as the DIS limits of the H and $\widetilde{H}$ distributions. In the limit of zero momentum transfer (forward limit), the GPDs must collapse to the usual DIS parton distributions. In particular the relation is:

$$H_q(x,0,0) = \begin{cases} q(x), & x > 0\,, \\ -\bar{q}(-x), & x < 0\,, \end{cases} \tag{2.50}$$

$$\widetilde{H}_q(x,0,0) = \begin{cases} \Delta q(x), & x > 0\,, \\ \Delta\bar{q}(-x), & x < 0\,. \end{cases} \tag{2.51}$$

2.2.2 Relation to Total Angular Momentum

In recent years the spin structure of the nucleon has been the object of intense investigation. The initial theory of the nucleon spin structure as a simple sum over the quark spins was shown to be inadequate to describe the experimental measurement of the quark contribution. The simple addition of the spin of the quarks over the quark distribution was observed to differ from the nucleon spin value of 1/2 (in natural units of $\hbar = c = 1$) [3], a problem now referred to as the Spin Puzzle. In fact, only about 30% of the proton's spin originates from the spin of the quarks. The rest must arise from the gluon spin or from the orbital angular momentum of the quarks and gluons. The individual contributions of the nucleon spin projected along an axis can, in some sense, be expressed as (neglecting scheme and scale dependences) [20]:

$$\frac{1}{2} = \frac{1}{2}\Delta\Sigma + \Delta g + L_q + L_g\,, \tag{2.52}$$

with $\frac{\Delta\Sigma}{2}$ (Δg) representing the quark (gluon) spin and L_q (L_g) the orbital angular momentum of the quarks (gluons). Here, a sum over the various flavors is implied. The only contribution measured with some precision at present is the quark spin contribution $\Delta\Sigma$ measured in deep inelastic scattering of polarized leptons from polarized targets.

There have been some recent estimations of the gluon spin Δg contribution from an extraction using the DIS structure function $g_1(x_{Bj}, Q^2)$ and QCD evolution. However, the available experimental data has a limited range in Q^2 and x_{Bj}, which provide a small lever arm and contribute a large theoretical uncertainty to the final extraction. The situation looks more promising for the future as the measurement of Δg is a focus of several experiments, for example, COMPASS, RHIC and the HERA experiments with polarized proton and lepton beams [21–23].

A method to measure the last two contributions to the spin of the nucleon in Eq. 2.52, the orbital angular momentum contributions of the quarks and gluons is not obvious. Recently, Ji proposed a new idea to access these quantities using the generalized parton distributions [19]. The idea is that the total angular momentum of the quarks or gluons can be written in terms of the energy-momentum tensor. The tensor is also related to the generalized parton distributions, so if the GPDs were known, they could be used to evaluate the the total angular momentum.

Following the argument of Ji [19], the angular momentum operator in QCD is defined according to the generators of Lorentz transformation,

$$J^i = \frac{1}{2}\epsilon^{ijk}\int d^3x M^{0jk} \ , \tag{2.53}$$

where M^{0ij} is the angular momentum density, expressible in terms of the energy-momentum tensor $T^{\mu\nu}$ through

$$M^{\alpha\mu\nu} = T^{\alpha\nu}x^\mu - T^{\alpha\mu}x^\nu \ . \tag{2.54}$$

The energy-momentum tensor can be separated into quark and gluon contributions which are separately gauge invariant,

$$T^{\mu\nu} = T^{\mu\nu}_q + T^{\mu\nu}_g \ , \tag{2.55}$$

where the quark part can be written as,

$$T^{\mu\nu}_q = \frac{1}{2}[\bar{\psi}\gamma^\mu i\overrightarrow{D^\nu}\psi + \bar{\psi}\gamma^\nu i\overrightarrow{D^\mu}\psi + \bar{\psi}\gamma^\mu i\overleftarrow{D^\nu}\psi + \bar{\psi}\gamma^\nu i\overleftarrow{D^\mu}\psi] \ , \tag{2.56}$$

where $\overrightarrow{D^\nu}$ denotes an extended derivative ($D^\nu = \delta^\nu + ieA^\nu$ with A^ν the vector gauge field) acting on the wave function designated by the arrow direction. The gluon part can be written as,

$$T^{\mu\nu}_g = \frac{1}{4}g^{\mu\nu}F^2 - F^{\mu\alpha}F^\nu_{\ \ \alpha} \ , \tag{2.57}$$

where $F^2 \equiv F_{\alpha\beta}F^{\alpha\beta}$. Combining the above equations, the angular momentum operator $\vec{J}$ can be written as a gauge invariant sum, $\vec{J} = \vec{J}_q + \vec{J}_g$, where

$$J^i_{q,g} = \frac{1}{2}\epsilon^{ijk}\int d^3x(T^{0k}_{q,g}x^j - T^{0j}_{q,g}x^k) \ . \tag{2.58}$$

Here and in what follows, a subscript (q, g) will be used to represent two equations for the quarks (q) and gluons (g).

To experimentally access the energy-momentum tensor, a parameterization in terms of "energy tensor forms factors" can be made,

$$\begin{aligned}\langle p'|T^{\mu\nu}_{q,g}|p\rangle \ = \ & \bar{u}(p')\Big[A_{q,g}(\Delta^2)\gamma^{(\mu}P^{\nu)} + B_{q,g}(\Delta^2)P^{(\mu}i\sigma^{\nu)\alpha}\Delta_\alpha/2 \\ & +C_{q,g}(\Delta^2)(\Delta^\mu\Delta^\nu - g^{\mu\nu}\Delta^2)/M + \bar{C}_{q,g}(\Delta^2)g^{\mu\nu}M\Big]u(p) \ ,\end{aligned} \tag{2.59}$$

where $P^\mu = (p^\mu + p^{\mu\prime})/2$, $\Delta^\mu = p^{\mu\prime} - p^\mu$, and $u(p)$ is the nucleon spinor [19, 20]. The coefficients (A,B,C) could be extracted from a fit to experimental data. Integrating the $\mu = 0$ component over 3-momentum space in the forward limit ($\Delta = 0$), Ji finds that the terms $A_{q,g}(0)$ are just the momentum fractions of the nucleon carried by quarks and gluons ($A_q(0) + A_g(0) = 1$) [19]. The $A_{q,g}(0)$ terms are therefore equivalent to the parton distributions:

$$\begin{aligned} A_q(0) &= \int dx\ x\ H_q(x, \xi, t = 0) = \int dx\ x\ q(x)\,, \\ A_g(0) &= \int dx\ x\ H_g(x, \xi, t = 0) = \int dx\ x\ g(x), \end{aligned} \tag{2.60}$$

where $q(x)$ ($g(x)$) represent the usual quark (gluon) distributions, and in the forward limit the GPD and DIS parton distributions are the same. Substituting the above representation for the energy-momentum tensor back into the nucleon matrix element of Eq. (2.58) and performing the integration yields the result:

$$J_{q,g} = \frac{1}{2}\left[A_{q,g}(0) + B_{q,g}(0)\right]\ . \tag{2.61}$$

The energy-momentum tensor $T^{\mu\nu}_{q,g}$ appears in some DIS sum rules and thus the form factors of the energy-momentum tensor are in principle accessible in DIS processes. Unfortunately, only the energy-momentum form factors $A_{q,g}(0)$ are measurable in DIS as the $B_{q,g}(0)$ terms do not contribute to the forward matrix elements. However, measuring the *non-forward* matrix elements and extrapolating to the forward limit can give access to the $B_{q,g}(0)$ terms as the second moments of the GPDs are related to the form factors of the energy-momentum tensor,

$$\int dx\ x\ H_{q,g}(x, \xi, t) = A_{q,g}(t) + \xi^2 C_{q,g}(t)\,, \tag{2.62}$$

and

$$\int dx\ x\ E_{q,g}(x, \xi, t) = B_{q,g}(t) - \xi^2 C_{q,g}(t)\,, \tag{2.63}$$

where the separate quark and gluon equations have been combined. Combining the above two equations results in,

$$\int dx\ x\ \left[H_{q,g}(x, \xi, t) + E_{q,g}(x, \xi, t)\right] = A_{q,g}(t) + B_{q,g}(t)\,. \tag{2.64}$$

Extrapolating this sum rule to $t = 0$, the total angular (orbital plus spin) momentum contribution to the nucleon spin is obtained in Ji's sum rule,

$$J_{q,g} = \frac{1}{2}\int dx\ x\ [H_{q,g}(x,\xi,t=0) + E_{q,g}(x,\xi,t=0)]\,, \tag{2.65}$$

for each quark or gluon flavor.

According to Jaffe [24], there is a problem with the above formalism. In order to obtain a partonic interpretation of the angular momentum, the vector potential gauge choice $A^+ = 0$ is needed. Jaffe extracts a sum rule by first polarizing the nucleon along the 3-direction in the rest frame. Then the elements $\nu = 1,\ \lambda = 2$ of the (rotation and boost) density tensor $M^{\mu\nu\lambda}$ are used to select rotations about the 3-direction. A choice of either the M^{012} or M^{+12} element of the density tensor can be used to form the sum rule. The choice of M^{+12} results in an interaction independent sum rule due to the gauge choice of $A^+ = 0$ as all interaction terms drop out. The terms in the sum rule can then be written as integrals over the parton distributions

$$\frac{1}{2} = \int_0^1 dx \left\{ L_q(x,Q^2) + \frac{1}{2}\Delta q(x,Q^2) + L_g(x,Q^2) + \Delta g(x,Q^2) \right\}. \tag{2.66}$$

In this decomposition, each term is gauge invariant, interaction independent, and each contribution is an integral over the partonic density of the appropriate generator [25–27].

However, the sum rule of Ji is made using the M^{012} element in order to make a connection to the GPD framework. The interaction dependences do not drop out in the gauge of $A^+ = 0$. According to Jaffe, the sum rule

$$\frac{1}{2} = \frac{1}{2}\Delta\Sigma + \langle \Delta g \rangle + \langle L_q \rangle + \langle L_g \rangle\,, \tag{2.67}$$

still holds but the contributions from the gluon spin and the orbital angular momentum of the quarks and gluons are only expectation or mean values of the operators, since the quarks interact with the gluons and the contributions are now mixed. There are no parton representations for $\langle \Delta g \rangle$, $\langle L_q \rangle$, or $\langle L_g \rangle$, so Eq. 2.67 is not a 'classic' sum rule over parton distributions. Extracting out the total angular momentum from the GPDs for the quarks and gluons is still possible, however, the interpretation in terms of the partons is not straightforward.

A simple physical interpretation of the link between the GPDs and angular momentum has been investigated by Burkardt in the limit of $\xi = 0$, when the momentum transfer is only in the transverse direction [15]. In this limit, the representation of the GPDs using the light front wave functions (Fock space amplitudes) resemble the non-relativistic form factor expressions. By analogy with the form factors, the GPDs (at $\xi = 0$) can be written as the Fourier transform of parton distributions in the transverse plane. For example, the GPD function $H(x, \xi, t)$ and $E(x, \xi, t)$ can be written:

$$H(x, \xi = 0, t = \Delta_{\perp}^{2}) = \int d^{2}b_{\perp} \exp^{-i\Delta_{\perp}\cdot b_{\perp}} f(x, b_{\perp}), \tag{2.68}$$

$$E(x, \xi = 0, t = \Delta_{\perp}^{2}) = \int d^{2}b_{\perp} \exp^{-i\Delta_{\perp}\cdot b_{\perp}} f(x, b_{\perp}), \tag{2.69}$$

where $f(x, b_{\perp})$ is the probability to find a quark with momentum fraction x at a perpendicular distance $b_{\perp}$ from the (perpendicular) center of momentum. In other words, the GPDs (at $\xi = 0$) allow for a simultaneous determination of the momentum of the partons in the z direction (+ direction on the light cone) and the position in the perpendicular direction (denoted here as the y direction). For a nucleon polarized in the x direction, this simultaneous measurement has been shown by Burkardt to be related to the angular momentum operator in the x direction (for more details of this calculation see Ref. [15]):

$$\begin{aligned} \langle J_{q}^{x} \rangle &= \langle y T^{0z} \rangle - \langle z T^{0y} \rangle \\ &= 2\langle y T^{0z} \rangle \quad \text{(in the nucleon rest frame)} \\ &= 2\frac{M}{2} \int dx \int d^{2}b_{\perp}\ b_{y}\ x\ f(x, b_{\perp}) \\ &= \frac{1}{2} \int dx\ x\ [H(x, 0, 0) + E(x, 0, 0)]\,. \end{aligned} \tag{2.70}$$

Therefore, the GPDs are, in the $\xi = 0$ limit, related to the expectation value of $\langle y p_{z} \rangle$. The probability interpretation of the DIS formalism has now returned, since the initial and final momentum fractions in the longitudinal direction are now equal ($\xi = 0$).

The contributions of the total angular momentum of the quarks and gluons appear to be obtainable using a measurement of the GPDs and the sum rule of Ji. Of course, the GPDs will need many measurements of various exclusive processes in order to extract the different type of GPDs in addition to separating out the quark from the gluon GPDs which poses a non-trivial task. In addition, total angular momentum of the quarks can, in principle, be decomposed into gauge invariant spin and orbital contributions. However, a similar gauge invariant decomposition is not possible for the total angular momentum of the gluons ($J_{g} = \Delta g + L_{q}$ is gauge dependent) [19]. The contributions obtained from the GPDs also appear not to have a simple parton interpretation at this time, and so may not be useful in testing our understanding of the nucleon structure. The theoretical debate is still continuing regarding the usefulness of the GPDs to the Spin Puzzle, and hopefully a solution will be forthcoming. Perhaps with QCD lattice-type calculations of the generalized parton distributions a clearer picture of the contributions to the nucleon spin will emerge.

2.3 Modeling the GPDs

The generalized parton distributions (and the usual parton distributions) are non-perturbative objects, and therefore, can not be calculated in perturbative QCD. To predict observables, one has to first model the underlying parton distributions and then calculate the observables (or use lattice calculations). When enough experimental data becomes available, a parameterization of (fit to) the measured generalized parton distributions can be used to test the applicability of the models.

There is, at present, little experimental data available from exclusive processes. Until recently when factorization was proven and the GPD framework developed, there was little theoretical input. However, with factorization and the connection to the angular momentum, there has been increased theoretical development of the GPD framework. There are several calculations of the quark GPDs using models such as the MIT bag model [28] and the quark soliton model [29]. A light-cone wave function approach to the GPDs for a Fock state decomposition of the nucleon has been investigated which however, yields only a partial modeling of the GPDs for the DVCS process [30]. Parameterization of the quark GPDs, using the relationship to the form factors and parton distributions, is perhaps the easiest method to describe the (quark) GPDs and has resulted in the most complete predictions for the experimental observables [31].

2.3.1 Parameterization

A simple method to describe the quark GPDs is with a parameterization using the known relationships to the (forward) parton distributions and the elastic form factors. One of the first such parameterizations and calculations of exclusive observables was completed by Vanderhaeghen, Guichon, and Guidal [31]. With the relations to the parton distributions, distribution amplitudes, and first moments a parameterization of the quark GPDs can be made from interpolations of these functions. For a first guess, a ξ independent parameterization was made, assuming factorization for the x and t dependences. With this assumption, the use of the form factors and parton distributions is straightforward:

$$H(x,t) \propto q(x)F(t). \tag{2.71}$$

The resulting parameterization of the GPDs must be properly normalized to reproduce the relationship in the forward limit and in the first moment. For the unpolarized H functions in the proton the explicit form becomes:

$$\begin{aligned} H^{u/p}(x,t) &= u(x)\, F_1^{u/p}(t)/2\ , \\ H^{d/p}(x,t) &= d(x)\, F_1^{d/p}(t)\ , \\ H^{s/p}(x,t) &= 0\ , \end{aligned} \tag{2.72}$$

and for the polarized $\widetilde{H}$:

$$\begin{aligned} \widetilde{H}^{u/p}(x,t) &= \Delta u_V(x)\, g_A^{u/p}(t)/g_A^{u/p}(0)\ , \\ \widetilde{H}^{d/p}(x,t) &= \Delta d_V(x)\, g_A^{d/p}(t)/g_A^{d/p}(0)\ , \end{aligned} \tag{2.73}$$

assuming a symmetric sea contribution. This first estimate has no ξ dependence, and the E and $\widetilde{E}$ functions can not be so easily parameterized as there are no corresponding parton distributions from DIS for the forward limit.

To include the ξ dependence, a more sophisticated approach is needed. To simplify the parameterization, factorization of the momentum transfer (t) is again assumed, with the t dependence given by the elastic form factors. The x and ξ dependence, however, can not be separated by a simple factorization assumption. As mentioned previously, the GPDs are equivalent to the DIS parton distributions (characterized by the momentum fraction x) when the momentum transfer t goes to zero. In the opposite limit ($t >> x$), the GPDs resemble meson distribution amplitudes which are characterized by the variable α, defined earlier in Sec. 2.2 (see also Eq. 2.34). Therefore, a variable combination of the parton distributions (functions of $x = x_{Bj}$) and meson distribution amplitudes (functions of α) should result in a fair approximation. The GPDs must reduce to the parton distributions in the limit of $t = 0$ and $\xi = 0$, therefore, is has been argued by Radyushkin that the combination of the parton distributions and meson amplitudes should be of the form [32]:

$$h(x_{Bj}, \alpha)\ q(x_{Bj})\ , \tag{2.74}$$

where $q(x_{Bj})$ is the quark distribution obtained in DIS and $h(x_{Bj}, \alpha)$ is a generic function. The function $h(x_{Bj}, \alpha)$ must be an even function since the GPDs are even functions, and is normalized as:

$$\int_{-1+|x_{Bj}|}^{1-|x_{Bj}|} h(x_{Bj}, \alpha) d\alpha = 1\ , \tag{2.75}$$

to ensure the correct forward limit. The function $h(x_{Bj}, \alpha)$ should be similar to a distribution amplitude, and could have several different forms. A simple choice motivated by models of quark and gluon distribution amplitudes was suggested by Radyushkin:

$$h^b(x_{Bj}, \alpha) = \frac{\Gamma(2b+2)}{2^{2b+1}\Gamma^2(b+1)}\ \frac{\left[(1-|x_{Bj}|)^2 - \alpha^2\right]^b}{(1-|x_{Bj}|)^{2b+1}}\ , \tag{2.76}$$

which has a width governed by the parameter b which incidentally characterizes the strength of the ξ dependence when the function has been transformed to a function of x and ξ of the GPD formalism. The limiting case when $b \to \infty$ corresponds to an ξ independent ansatz for the GPD. The b parameter is a free parameter which can be used in a fit of experimental observables to optimize the parameterization. The use of the function $h(x_{Bj}, \alpha)\ q(x_{Bj})$ to describe non-forward exclusive processes treats the parton distribution and distribution amplitude contributions on equal footing and is known as the Double Distribution (DD) formalism [33]. The parameterization using the DD formalism satisfies by construction the relationships to the parton distributions and elastic form factors. In addition, the GPDs obtained by reduction from the double distributions will automatically satisfy the polynomial conditions of Eq. 2.38, except for a few special cases. These are the odd-N moments of the helicity independent functions $H(x, \xi, t)$ and $E(x, \xi, t)$ where the $N + 1$ powers of ξ are not produced. These terms are missing in the GPDs generated from the DD formalism and must be added using the so-called D-term [34]. The D-term only contributes to the odd-N moments, therefore it must be an odd function which produces only the highest power of ξ in these moments. The magnitude of the D-term is the same for both $H(x, \xi, t)$ and $E(x, \xi, t)$, entering only with the opposite sign as illustrated in Eq. 2.39. There is no obvious constraint or limits on the D-term and therefore has been modeled by a calculation in the quark soliton model (described in Sec. 2.3.3) and included in the parameterization.

The double distribution formalism has no explicit ξ dependence. The usual description of the GPDs are in terms of the variables x and ξ and so a change of variables must be made from the variables $x = x_{Bj}$ and α of the double distributions

$$H_q(x, \xi) = \int_{-1}^{1} dx_{Bj} \int_{-1+|x_{Bj}|}^{1-|x_{Bj}|} d\alpha\ \delta(x - x_{Bj} - \alpha\xi)\ h(x_{Bj}, \alpha)\ q(x_{Bj}) \ . \tag{2.77}$$

An example of the GPD function $H(x, \xi, t)$, using this parameterization, is shown in Fig. 2.8 for different values of ξ at $t = 0$ for the d quark, taken from Ref. [31]. The parameterizations of the quarks used for the calculations are from the MRST98 parton distributions at a normalization scale of $\mu = 2\ \mathrm{GeV}^2$ [35]. Notice the $\xi = 0$ line, where the $H(x, \xi = 0, t = 0)$ function is just the DIS parton distribution, which has a minimal value at $x = 1$, and grows rapidly due to the gluon contributions at $x = 0$. As the value of ξ becomes larger, the function tends to broaden and have more moderate x behavior.

The factored t dependence is added in the parameterization of the H function,

$$\begin{aligned} H_u(x, \xi, t) &= H_u(x, \xi)\ F_1^u(t) \,/\, 2 \ , \\ H_d(x, \xi, t) &= H_d(x, \xi)\ F_1^d(t) \ , \\ H_s(x, \xi, t) &= 0 \ . \end{aligned} \tag{2.78}$$

To complete the GPD function $H(x, \xi, t)$, the D-term mentioned above is calculated from the quark soliton model and added to maintain the polynomial conditions.

The factored ansatz for the t dependence is a simple ansatz and only assumed to be valid for small values of t where the parton distribution contribution is larger and a possible error (ie, non-factorable t dependence) should be small. An improved t dependence may be obtained by using a Regge type ansatz where the t dependence is contained in a power of x, for example, $x^{-\alpha' t}$, where α' is the slope of the Regge trajectory [1]. This term can be included in the double distribution parameterization of Eq. (2.74) and may result in an improved t dependence.

The parameterization of $\widetilde{H}$ proceeds in the same way as for the H function, except with the use of the polarized parton distributions and the form factor $G_A(t)$ to account for the helicity dependent relations.

To parameterize the functions E and $\widetilde{E}$, more assumptions are needed since the forward limits of these GPDs are invisible in DIS. However, the factorization of t is used as before, as the first moment relations are also valid for the E and $\widetilde{E}$ functions. The forward limit of the GPD function $E(x, \xi, t)$ is constrained in Ref. [31] by using the anomalous magnetic moments for the proton and neutron:

$$
\begin{aligned}
F_2^p(0) &= \kappa^p = 1.793 \ , \\
F_2^n(0) &= \kappa^n = -1.913 \ .
\end{aligned}
\tag{2.79}
$$

Assuming a simple three (constituent) quark model of the nucleon, the magnetic moments are then used to obtain the quark (u, d) form factors at $t = 0$:

$$
\begin{aligned}
F_2^u(0) &= 2\kappa^p + \kappa^n = 1.673 \ , \\
F_2^d(0) &= \kappa^p + 2\kappa^n = -2.033 \ .
\end{aligned}
\tag{2.80}
$$

The first moment relationship of the GPD $E(x, \xi, t)$ is valid at $t = 0$ (see Eq 2.43) which provides the normalization for $e_q(x) \equiv E(x, \xi = 0, t = 0)$:

$$
\int_{-1}^{+1} dx \ e_q(x) = F_2^q(0). \tag{2.81}
$$

For a first guess, the same x dependence of a valence quark distribution can be used for the function $e_q(x)$ [8], which result in the correct forward limit

$$
\begin{aligned}
e_u(x) &= \frac{1}{2} u_{val}(x) F_2^u \ , \\
e_d(x) &= d_{val}(x) F_2^d \ , \\
e_s(x) &= 0.
\end{aligned}
\tag{2.82}
$$

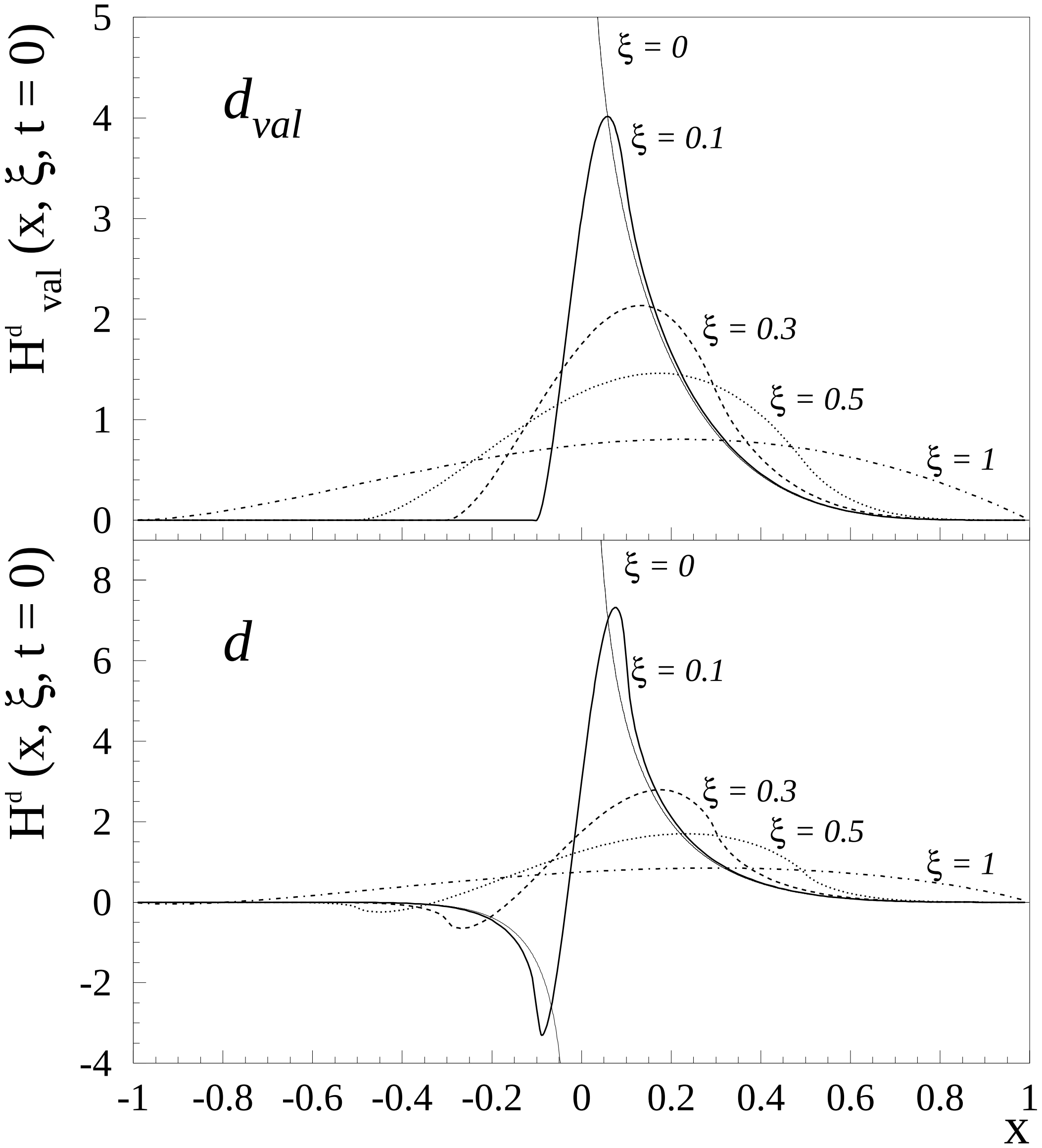

Figure 2.8: Double distribution part to the d-quark GPD H^d at $t = 0$ for different ξ, using the profile model of Eq. 2.76 with $b = 1$ from Ref. [31]. Upper panel : valence d-quark GPD, lower panel : total (valence and sea) d-quark GPD. The thin lines ($\xi = 0$) show the ordinary forward d-quark distributions (MRST98 parameterization [35] at $\mu^2 = 2$ GeV^2).

A delta function is used to parameterize the sea contribution to $e^q(x)$ in Ref. [8] since the sea contribution is symmetric in x and has a narrowly peaked form in the quark soliton model. This leads to an estimate of the forward functions $e^q(x)$

$$\begin{aligned} e_u(x) &= \frac{1}{2}u_{val}(x)F_2^u + \delta(x)F_2^u, \\ e_d(x) &= d_{val}(x)F_2^d + \delta(x)F_2^d, \\ e_s(x) &= 0. \end{aligned} \tag{2.83}$$

With a description of the the forward limit $e_q(x)$ the parameterization of $E(x,\xi)$ continues in the same manner as for H and $\widetilde{H}$. The same profile function (Eq. 2.76) is used and along with the forward limit function $e^q(x)$, transformed to a function of x and ξ. The t dependence is added, with a simple parameterization of the measured $F_2(t)$ as

$$F_2(t) \approx \frac{1}{(1-t/0.71)^2}, \tag{2.84}$$

resulting in:

$$E_q(x,\xi,t) = E_q(x,\xi)\,\frac{1}{(1-t/0.71)^2}. \tag{2.85}$$

And finally, the extra needed D-term, which has the same magnitude as for the H function but opposite sign, is added to complete $E_q(x,\xi,t)$.

Using the forward limit of the Ji sum rule (Eq. 2.65) allows a representation of the forward function $e_q(x)$ in terms of the known parton distributions and the total angular momentum J_q:

$$J_q = \frac{1}{2}\int_{-1}^{+1} dx\; x\;[q(x) + e_q(x)]. \tag{2.86}$$

This relation can be used to produce an E function which is parameterized in terms of the total (quark) angular momentum instead of $e_q(x)$. Then J_q can be used as a free parameter for fitting experimental data, allowing for a direct extraction.

The final parameterization is of the helicity dependent spin-flip $\widetilde{E}$ function. The main contribution to this GPD, as observed from the quark soliton model, is from the pion pole [36]. Therefore, a parameterization is made using the pion distribution amplitude in the asymptotic limit (Φ_{as}) as [8]:

$$\Phi_{as}\left(\frac{x}{\xi}\right) = \frac{3}{4}\left[1-\left(\frac{x}{\xi}\right)^2\right]. \tag{2.87}$$

The region of validity for the pion pole dominance is only in the x range where the quark and antiquark can couple to the nucleon ($-\xi \le x \le \xi$), enforced with a step function in the parameterization. The

t dependence is parameterized with the form factor $G_P(t)$. Combining the parts together results in a final form for $\widetilde{E}$

$$\widetilde{E}_u = -\widetilde{E}_d = \frac{1}{2}\,\widetilde{E}_{\pi-pole} \;=\; \theta\,(-\xi \leq x \leq \xi)\;G_P(t)\,\frac{1}{\xi}\,\Phi_{as}\left(\frac{x}{\xi}\right)\,. \tag{2.88}$$

The parameterization as outlined above results in the correct forward limits and also obeys the sum rules of the first moments. Although the constraints limit the form the parameterization may take, the assumptions used in this parameterization may result in a GPD which is inconsistent with reality. In addition, only the quark GPDs have been used, no contributions from the gluons have been included. Therefore, some experimental input is needed to check the validity of the assumptions.

2.3.2 MIT Bag Model

One of the first model calculations used a simple version of the MIT bag model to estimate the GPDs [28]. The MIT bag model [37] uses massless quarks, antiquarks, and gluons to comprise the nucleon. These partons are confined to a region of space (the bag) by use of a positive constant potential energy. This potential energy, along with the kinetic energy given to the partons, results in an effective mass, which for the u and d quarks is ≈ 340 MeV. The bag idea incorporates the concept of confinement, and also allows the partons to behave like non-interacting free particles, as observed in DIS. A small coupling term can be added in a more complex version of the model to account for the observed quantum numbers. The MIT bag model yields predictions which compare well to the form factors as well as to the parton distribution functions [38].

The simple MIT bag model has no gluon contribution and uses only three independent valence quarks inside the bag (no sea quark contribution). The wave functions of the quarks and the radius of the bag were determined to roughly reproduce the parton distributions at a low energy scale. The spherical Bessel functions were used for the quark wave functions, which have zero values at the radius of the bag, given by the relation $R = 4\omega_0/M$, with M being the mass of the nucleon, and ω_0 the lowest-frequency solution of the bag eigen-equation.

The modeling of the momentum transfer is an additional consideration for non-forward processes. The momentum transfer to the struck quark is partially transferred to the other quarks in order to keep the nucleon from breaking apart. In the asymptotic limit, the momentum transfer would be shared equally among the three quarks. With the quarks of the bag model being modeled as independent, the transfer of the momentum between quarks needs to be taken into account. A linear parameterization of the form $\eta\Delta$ is used to model the effective momentum transfer to the three quarks where η is a free parameter. This parameter is fixed by fitting the first moments of the model GPDs to match the

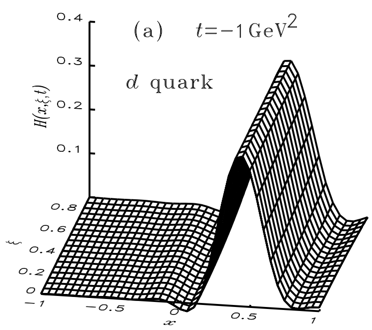

Figure 2.9: The generalized parton distribution $H(x, \xi, t)$ for the d quark at a momentum transfer of $t = \ -1\ GeV^2$ in the MIT bag model [28].

elastic form factors. The resulting functions H and $\widetilde{H}$ in this model have little dependence on the value of η, however, the functions E and $\widetilde{E}$ show strong dependence on this parameter.

As an example of the MIT bag model, the calculation for the GPD function $H(x, \xi, t)$ for the d-quark is shown in Fig. 2.9. The ξ dependence of the GPDs in the MIT bag model is very weak. The t dependence (not shown) is very similar to the t dependence of the elastic form factors. This simple MIT bag model does has some shortcomings, the main one being the bag surface is not described in terms of fields. This results in non-conservation of chiral symmetry and leads to negative antiquark distributions, which are unphysical. A more sophisticated bag model might be used to account for these shortcomings.

2.3.3 Quark Soliton Model

Another approach to the modeling of the GPDs uses a calculation in the quark soliton model [29]. The soliton model assumes nucleons consist of three valence quarks which are bound together using a radial (hedgehog) pion field. This pion field is the *soliton* which has an energy equal to the sum of the energy of the quarks in the negative-energy Dirac continuum. The number of QCD colors (known to be three) is allowed to become large in order to make use of mean field theory. In the large number-of-color limit ($N_c \to \infty$), the nucleon becomes heavy, and the mass can be obtained via a minimization procedure. This large N_c quark soliton model has been used to calculate the parton distribution functions and has shown to reproduce the nucleon static properties as well as several sum rules quite well [40]. The model yields quark and antiquark distributions which are positive. Explicit confinement of the quarks is missing in this model which however, does not seem to affect calculations involving the ground state of the nucleon. Also missing in the quark soliton model is the contribution from gluons; only the quark GPDs are calculable.

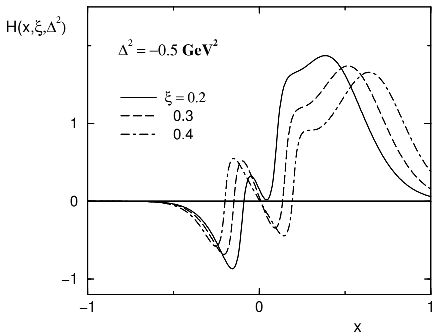

Figure 2.10: The generalized parton distribution $H(x, \xi, t)$ for the d quark at momentum transfer $t = -\Delta^2 = -0.5\ GeV^2$ as a function of x for several values of ξ in the quark soliton model [29].

The GPDs calculated in this model have rather different behaviors than in the MIT bag model calculations. The GPD function $H(x, \xi, t)$ for the d-quark is shown as a function of x in Fig. 2.10. A crossover behavior (inflection point) is present at the values of $x = \xi/2$, which is more distinctive in the positive momentum ($x > 0$) range. Also, the quark soliton predicts a stronger dependence on the value of ξ than in the MIT bag model.

2.3.4 Evolution Equations

The GPDs are modeled in both the MIT bag and quark soliton model at a low energy scale $O(Q^2) \sim 0.2$ GeV^2, which substantially differs from hard scattering energy scales needed for factorization to be valid. The model of the GPDs at low energy therefore needs to be transformed to the higher energy scales. The theoretical description of hard reactions incorporates only a minimal number of constituents in the hadron wave function in the lowest approximation, assuming negligible higher order (in α_s) terms. This approximation neglects QCD dynamics, which are manifest at low energy scales as scaling violations (Q^2 dependence). The approximation arises from an expansion of the process in the strong coupling constant α_s. The next-to leading order (NLO) term in the power expansion scales as $\ln(Q^2)$. These NLO terms involve an internal loop type Feynman diagram containing divergent integrals. The normal method to remove these divergences is by a renormalization operation characterized by some subtraction scale μ. The renormalization basically subtracts the divergent part from the integral and adds this divergent part into the GPD functions, since the GPD is a non-perturbative (non-calculable) object and must be measured in any case. The GPDs then acquire a renormalization scale (μ) dependence which is governed by an evolution equation. The evolution equations provide a way to evolve the generalized parton distributions to different scales of Q^2.

Since the GPDs have limits described by parton distributions ($t = 0$) and meson distribution amplitudes ($t >> x$), the evolution equations governing the renormalization scale dependence of the GPDs are convolutions of the parton and meson distribution amplitude evolution equations. The investigation of the evolution of the GPDs has been therefore in terms of functions which describes the behavior (x) of parton distributions and the behavior (α) of distribution amplitudes, the double distributions (DD) [33] introduced earlier (Sec. 2.3.1). The double distributions have no ξ dependence, and treat the x and α dependences on an equal footing. Integration over the α dependence results in the usual DIS parton distribution functions whose evolution is described by the Dokshitzer-Gribov-Lipatov-Altarelli-Parisi (DGLAP) [41]) equations. Alternatively, integration over x results in a function resembling a meson distribution amplitude (DA), which has an evolution similar to distribution amplitudes (Efremov-Radyushkin-Brodsky-Lepage (ERBL) [42] evolution). Therefore, a combination of these two types of evolution equations should describe the evolution of the GPDs.

Solutions to the evolution equation have been approached in the two regimes using the techniques used to solve the DGLAP and ERBL type equations, however, no analytical solution has been found which is valid in both regions. Some approximate numerical solutions have been worked out, and the asymptotic solution of the evolution equations has been studied [43]. Unfortunately, there has been limited evolution of the MIT bag and quark soliton model to an appropriate hard scale, and therefore the predictions may have reduced predictive ability.

The models (and parameterization) described in this section have certain common features due to the constraints. However, there are distinct characteristics of each model (parameterization), which will need experimental input to discern between them. The MIT bag model has little ξ dependence, in contrast to the other two. The quark soliton model has a cross over behavior at $x = \xi$, which is absent in the others. Unfortunately, the low normalization scale of both the MIT bag model and the quark soliton model requires the GPDs to be evolved up to scales where hard scattering is dominant, (this can be done with the evolution equations), but the evolution process is not exact and may result in a model which does not reflect the actual GPDs at the hard scales. The ultimate test of the usefulness of each model (parameterization) will be a comparison with experimental data.

2.4 Deeply Virtual Compton Scattering

The deeply virtual Compton scattering (DVCS) process

$$\gamma^*(q) + N(p) \to \gamma(q') + N(p') \,, \tag{2.89}$$

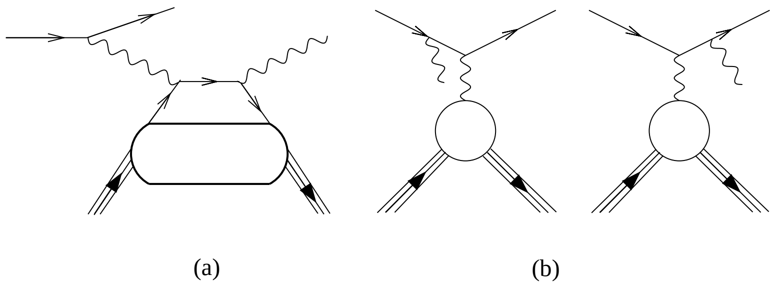

Figure 2.11: (a) Feynman diagram for deeply virtual Compton scattering, and (b) photon radiation from the incoming and scattered lepton in the Bethe-Heitler process.

is the exclusive process which is theoretically easiest to interpret in terms of the generalized parton distributions. A real photon is produced in the final state and the known point-like component of the virtual photon dominates in the interaction, hence there is no overlap of a hadronic wave function with the nucleon, as in exclusive meson production. However, the DVCS process has the identical final state as the Bethe-Heitler (BH) process, which makes the experimental extraction challenging. The handbag diagram for DVCS and the handbag diagrams for the BH process are shown in Fig. 2.11.

The BH process is well known and calculable, and in principle could be subtracted from the photon leptoproduction cross section. However, at most presently accessible kinematic regimes, the BH process dominates over the exclusive photon cross section. The propagator for the BH process has a $1/t$ dependence, and hence BH dominates at low values of t. The DVCS cross section decreases more rapidly with Q^2 than does the BH cross section. The BH cross section is dominant therefore at high Q^2 and low t, exactly where a measurement of DVCS has the cleanest interpretation in terms of the GPDs. Although challenging, a measurement of the DVCS cross-section is presently attainable at low x_{Bj} regions.

2.4.1 DVCS Cross Section Measurements

The HERA collider experiments ZEUS and H1 have attributed an excess of photon production (relative to the BH yield) to the DVCS process [4, 5]. Both experiments collected data in 1996 and 1997 using the 820 GeV proton beam and 27.6 GeV positron beam of the HERA accelerator facility. Both ZEUS and H1 have similar experimental setups and extract the photon production in a like manner. The recoil proton in the collider experiments continues down the beam pipe undetected by the spectrometers. The scattered positron and produced photon are detected by selecting events with exactly two clusters in the electromagnetic calorimeters, which must be in opposite hemispheres. The two cluster events in the same hemisphere are dominated by BH and are collected as control samples.

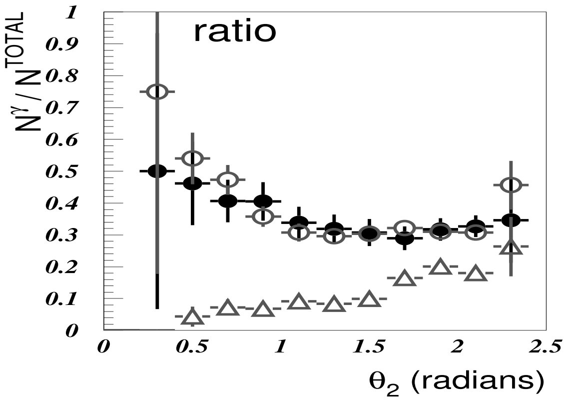

Figure 2.12: The ratio of events with two opposite photon clusters to all two-cluster events as a function of the forward cluster polar angle (θ_2) from the ZEUS experiment [4] for $Q^2 > 6$ GeV^2 and $0.0005 < x < 0.01$. Data (solid circles) are shown along with a BH (open triangles) and BH plus DVCS (open circles) simulation.

The selected events are further constrained by requiring a maximum of one track, which must be associated with one of the clusters. If no track is found, the cluster in the backward hemisphere (direction of the lepton beam) is assumed to be produced from a positron.

For the ZEUS experiment, a ratio of events with two opposite photon clusters to all two-cluster events is taken to reduce effects of the inelastic contribution and detector inefficiency. The ratio is shown in Fig. 2.12 as a function of the opening angle (θ_2) for the photon dominated clusters in the forward hemisphere. The BH simulation is consistent with the control sample (not shown), yet considerably underestimates the ratio of Fig. 2.12. A BH + DVCS Monte Carlo (MC) simulation was constructed by Frankfurt, Freund, and Strickman (FFS) [44] using an aligned jet model argument in the small x_{Bj} limit where the GPDs are proportional to the parton distributions. The BH + DVCS simulation reproduces the angular distribution of the ratio suggesting that the excess is arising from the DVCS process. A Monte Carlo simulation and shower shape studies were used to ensure that the excess was not arising from π^0/η decays.

Recently ZEUS has extracted the DVCS cross section [45]. The BH contribution was subtracted from the photon sample using a theoretical calculation. The data were also corrected for detector smearing and acceptance. The cross section was measured in the kinematic region defined by $Q^2 > 5\ GeV^2$, $40 < W < 140\ GeV$, $E_T^{\gamma} > 3\ GeV$ and $-0.6 < \eta_{\gamma} < 1.0$, where W is the invariant mass of the virtual photon and target system and E_T^{γ} and η_{γ} are the transverse energy and pseudo-rapidity of the final state photon, respectively. In Fig. 2.13, the DVCS cross section is shown as a function of

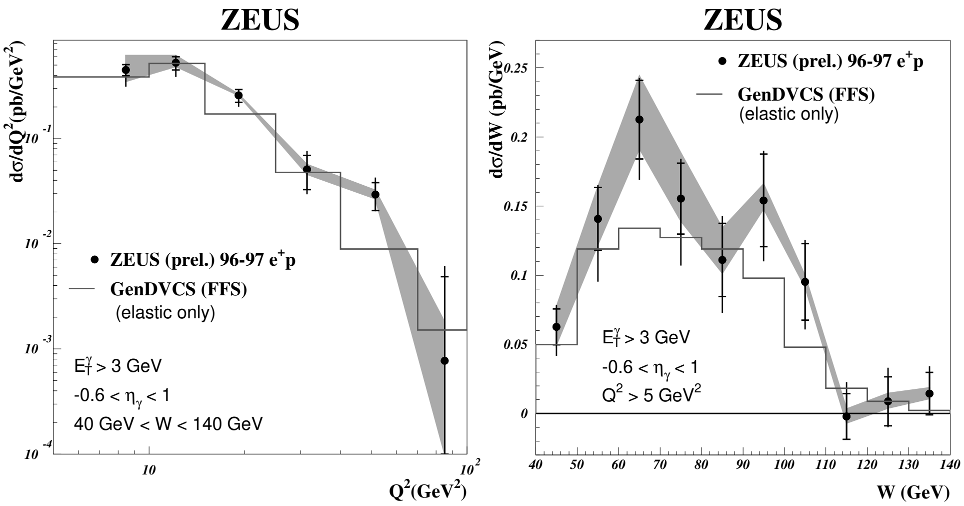

Figure 2.13: Differential DVCS cross section as a function of Q^2 (left) and W (right) for the ZEUS experiment. The data (solid points) are plotted with statistical (inner error bar) and systematic errors added in quadrature. The calorimeter energy scale uncertainty, which is correlated between bins, is shown separately as the shaded band. The histogram represents the DVCS (FFS) simulation.

Q^2 and W and compared with the DVCS (FFS) simulation. The predictions are in general agreement with the data, both in shape and normalization. However, the data include also a small (about 20%) contribution of inelastic events which are not accounted for in the MC simulation. A correction for these inelastic events should improve the overall agreement between the data and MC simulation. The major contributions to the systematic uncertainty comes from the BH calculation, the hadronic background determination, and the uncertainty in the energy scale of the calorimeter.

The H1 data were extracted with slightly stronger constraints to ensure data samples had minimal contaminations. The BH dominated control sample is well modeled by a BH calculation. This same calculation was then used to subtract the BH contribution from the data sample with two opposite photon clusters to obtain the elastic DVCS cross section as shown in Fig. 2.14. The DVCS cross section data were compared to the DVCS aligned jet model MC (FFS) and a DVCS calculation in the dipole picture by Donnachie and Dosch (DD) [46]. The data are in agreement with both models.

2.4.2 Extraction of DVCS with Asymmetry Measurements

At the kinematics of the HERMES experiment, the BH cross section is typically an order of magnitude larger than the DVCS cross section. Shown in Fig. 2.15 is a calculation of the BH cross section along with a DVCS calculation in the parameterization calculation, as a function of the opening angle between the virtual and produced (real) photon ($\theta_{\gamma*\gamma}$). The dominant BH contribution makes extracting the DVCS cross section (with some precision) very difficult by a simple subtraction.

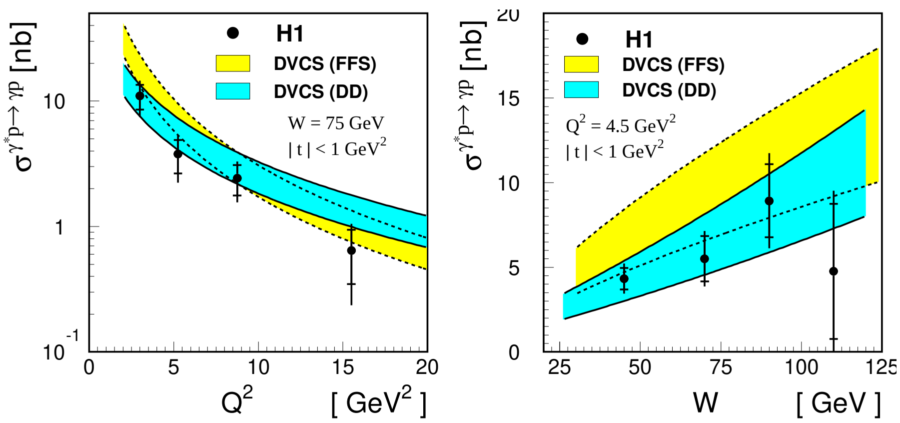

Figure 2.14: $\gamma^* p \to \gamma p$ DVCS cross section as a function of Q^2 (a) and W (b) obtained from the H1 experiment [5]. The data (solid points) are plotted with statistical (inner error bar) and systematic errors added in quadrature. Theoretical predictions of the FFS [44] and DD [46] Monte Carlo simulations are shown with gray band. The band width comes from the theoretical uncertainty connected with the t-slope which is assumed to be between 5 (upper edge of the band) and 9 GeV^{-2} (lower edge).

However, it was realized that the large BH contribution could be utilized to access the DVCS process in the interference term [16]. Quantum mechanics stipulates that particles states which are identical will interfere with each other. This interference results in an additional contribution to the scattering amplitude.

The interference arises in the formulation of the scattering cross section for the single photon production process:

$$e(E, \vec{\kappa}) + N(E_p, \vec{p}) \to e'(E', \vec{\kappa'}) + \gamma(\nu', \vec{q'}) + N(E'_p, \vec{p'}). \tag{2.90}$$

Note the use of κ, κ' for the lepton momentum, as the variable k will be used as previously to designate the struck quark momentum. Starting from Fermi's Golden rule, the cross section can be written:

$$d\sigma = \frac{1}{4\kappa p}|T|^2(2\pi)^4\delta^4(\kappa + p - \kappa' - p' - q')\frac{d^3\vec{\kappa'}}{2E'(2\pi)^3}\frac{d^3\vec{p'}}{2E'_p(2\pi)^3}\frac{d^3\vec{q'}}{2\nu'(2\pi)^3}, \tag{2.91}$$

where the squared scattering amplitude $|T|^2$ contains the interference term in addition to the squared DVCS and BH contributions:

$$|T|^2 = \sum_{\lambda', S_2, \Lambda} \left\{ |T_{DVCS}|^2 + |T_{BH}|^2 + T_{DVCS}T^*_{BH} + T^*_{DVCS}T_{BH} \right\}. \tag{2.92}$$

The BH amplitude dominates at HERMES kinematics, therefore the magnitude of the interference term should be less than the squared BH amplitude, but much larger than the squared DVCS amplitude (assuming the same order of magnitude for the real and imaginary parts of the DVCS amplitude).

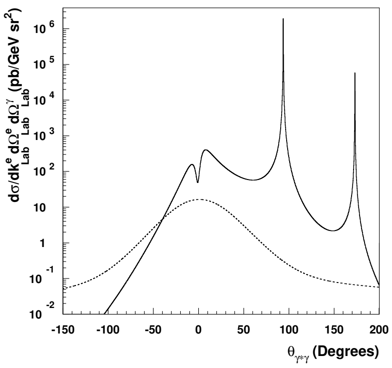

Figure 2.15: The differential cross section (in the lab) of the Bethe-Heitler (solid) and DVCS (dashed) processes as a function of the opening angle $\theta_{\gamma*\gamma}$ obtained from the parameterization calculation [31]. The calculation was produced for HERMES kinematics: $E_{Beam} = 27.6$ GeV, $Q^2 = 2.5$ GeV^2, and $x_{Bj} = 0.1$.

Extracting out the interference term should be easier than obtaining the squared DVCS amplitude, if an appropriate observable can be found.

The Bethe-Heitler process is the emission of a real photon before or after the elastic scattering from the nucleon. Since the interaction with the nucleon is elastic, the BH amplitude is purely real and can be written (following the formalism of Ref. [13] and neglecting the lepton mass)

$$T_{BH} = \frac{-e^3}{\Delta^2}\bar{u}(\kappa')\left[\not{\epsilon}^* \frac{1}{\not{\kappa} - \not{\Delta} + i\epsilon}\gamma^\mu + \gamma^\mu \frac{1}{\not{\kappa}' + \not{\Delta} + i\epsilon}\not{\epsilon}^*\right] u(\kappa)\langle P'|J_\mu(0)|P\rangle \ , \tag{2.93}$$

where $\bar{u}$ and u are the lepton spinors and ϵ is the polarization of the emitted photon. The elastic nucleon matrix can be parameterized as,

$$\langle P'|J_\mu(0)|P\rangle = \bar{U}(p')\left[\gamma_\mu F_1(\Delta^2) + F_2(\Delta^2)\frac{i\sigma_{\mu\nu}\Delta^\nu}{2M}\right] U(p) \ , \tag{2.94}$$

where $\bar{U}$ and U are used to represent the nucleon spinors and F_1 and F_2 are the usual Dirac and Pauli form factors of the nucleon. Likewise the DVCS amplitude can be expressed:

$$T_{DVCS} = \mp \frac{e^3}{q^2}\bar{u}(\kappa')\gamma^\mu u(\kappa) T_{\mu\nu}\epsilon^{\nu *} \ \text{ with } \begin{cases} - & \text{for } e^-, \\ + & \text{for } e^+. \end{cases} \tag{2.95}$$

where $T_{\mu\nu}$ is the standard Compton amplitude (shown previously in Eq. 2.22)

$$T^{\mu\nu} = i\int \frac{d^4k}{(2\pi)^4}\ \mathrm{Tr}\left(\left[\gamma^\nu \frac{i}{\not{k} - \not{\Delta} + \not{q} + i\epsilon}\gamma^\mu + \gamma^\mu \frac{i}{\not{k} + \not{\Delta} - \not{q} + i\epsilon}\gamma^\nu\right] M(k)\right) . \tag{2.96}$$

Here, k represents the momentum of the struck quark. The quark density matrix $M(k)$ can be transformed to $M(x)$ (see Eq 2.24) which can be expressed in terms of generalized parton distributions according to Eqs. 2.35 and 2.36.

In the DVCS process, an on-shell photon is produced at the vertex, resulting in an absorptive part to the cross section. This absorptive part leads to a phase difference between the DVCS and BH amplitudes in the interference term which can be measured by taking an asymmetry with respect to the spin of the particle.

Parity and time reversal invariance can be used to illustrate how the asymmetry depends on the absorptive part (phase difference) of the two process in the interference term. A one-particle helicity state transforms under the combined parity and time reversal operation as

$$|\mathbf{k},\lambda\rangle \longrightarrow \eta(\lambda)|\mathbf{k},-\lambda\rangle \ , \tag{2.97}$$

where $\eta(\lambda)$ is ± 1 depending on λ, the spin of the particle and on its internal parity. The combined parity and time reversal operations changes a given helicity state into a state with the same momentum but with opposite helicity. The DVCS and the BH processes are invariant under parity and time reversal therefore, the scattering T-matrix elements satisfy the relation

$$\begin{aligned} &\langle \vec{k}', \lambda'_e; \vec{p}', \lambda'_p; \vec{q}', \lambda'_q | T | \vec{k}, \lambda_e; \vec{p}, \lambda_p \rangle \\ &\qquad = \prod_i \eta_i \langle \vec{k}', -\lambda'_e; \vec{p}', -\lambda'_p; \vec{q}', -\lambda'_q | T^\dagger | \vec{k}, -\lambda_e; \vec{p}, -\lambda_p; \rangle^*, \end{aligned} \tag{2.98}$$

where λ_i (λ'_i) denotes the helicity of the initial (final) particle states. For an initial positron of definite helicity of $\pm 1/2$ the cross section (neglecting all kinematic factors) can be written:

$$\sigma(\pm) \propto \sum_{\{\lambda_i,\lambda'_i\}} |T_{\lambda'_e,\lambda'_p,\lambda'_q;\pm 1/2,\lambda_p}|^2 \ , \tag{2.99}$$

with $\pm$ representing the helicity of the initial positron. The single spin asymmetry (or helicity difference) of the cross sections can be written therefore as:

$$\sigma(+) - \sigma(-) \propto \sum_{\{\lambda_i,\lambda'_i\}} |T_{\lambda'_e,\lambda'_p,\lambda'_q;+1/2,\lambda_p}|^2 - \sum_{\{\lambda_i,\lambda'_i\}} |T_{\lambda'_e,\lambda'_p,\lambda'_q;-1/2,\lambda_p}|^2. \tag{2.100}$$

This equation is equivalent to the real part of the factored equation:

$$\begin{aligned} \sigma(+) - \sigma(-) \propto \Re e &\sum_{\{\lambda_i,\lambda'_i\}} \left[T_{\lambda'_e,\lambda'_p,\lambda'_q;+1/2,\lambda_p} + T^*_{\lambda'_e,\lambda'_p,\lambda'_q;-1/2,\lambda_p} \right] \\ &\times \left[T^*_{\lambda'_e,\lambda'_p,\lambda'_q;+1/2,\lambda_p} - T_{\lambda'_e,\lambda'_p,\lambda'_q;-1/2,\lambda_p} \right]. \end{aligned} \tag{2.101}$$

Substituting in Eq. 2.98 the equation can be transformed to the real part of:

$$\begin{aligned} \sigma(+) - \sigma(-) \propto \Re e &\sum_{\{\lambda_i,\lambda'_i\}} \left[T_{\lambda'_e,\lambda'_p,\lambda'_q;+1/2,\lambda_p} + \prod_i \eta_i T^*_{-\lambda'_e,-\lambda'_p,-\lambda'_q;-1/2,-\lambda_p} \right] \\ &\times \left[T^*_{\lambda'_e,\lambda'_p,\lambda'_q;+1/2,\lambda_p} - \prod_i \eta_i T_{-\lambda'_e,-\lambda'_p,-\lambda'_q;-1/2,-\lambda_p} \right]. \end{aligned} \tag{2.102}$$

If there would be no absorptive part of T, i. e., $T = T^\dagger$, then, according to (2.98), the difference of the helicity cross sections is zero. Therefore, the asymmetry is a measure of the absorptive part, or the difference in the phase of the BH and DVCS processes. This type of single spin asymmetry is accessible at experiments which use a polarized beam, such as the HERMES experiment.

Another way to isolate the interference term is that the DVCS amplitude, unlike the BH amplitude, depends on the sign of the lepton charge (see Eq. 2.95). The squared DVCS amplitude will have no dependence on the lepton charge, however, the interference term will change sign with the lepton charge. An asymmetry with respect to the charge of the lepton ($\sigma(e^+) - \sigma(e^-)$) can also be used to isolate the interference term.

Explicit contraction of the currents for the BH and DVCS process involves long complicated equations for the squared BH, DVCS, and interference terms, which are useful for cross section measurements. However, for asymmetry measurements, only the interference term is important and will be investigated further. More explicit equations of the complete cross section can be found for example in [13, 16, 47].

Following the formalism of Belitsky [47], the difference in the helicity cross sections at leading twist ($O(1/Q)$) for a polarized positron beam and unpolarized target can be written as

$$\begin{aligned} d\sigma^{\uparrow} - d\sigma^{\downarrow} = &-\frac{16(2-y)\sqrt{1-x_{Bj}}}{\sqrt{1-y}x_{Bj}\sqrt{-tQ^2}}\sqrt{1-\frac{t_{min}}{t}}\sin\phi \\ &\times \Im m\left\{ F_1\mathcal{H}_1 + \frac{x_{Bj}}{2-x_{Bj}}(F_1+F_2)\widetilde{\mathcal{H}}_1 + \frac{t}{4M^2}F_2\mathcal{E}_1 \right\} d\mathcal{M}\ , \end{aligned} \tag{2.103}$$

here y, the invariant fractional energy carried by the virtual photon ($y = \nu/E_{Beam}$ in the lab frame), is introduced for a concise formalism, and ϕ is the azimuthal angle between the lepton scattering plane and the photon production plane. Note that the angle ϕ is the azimuthal angle of the real produced photon around the direction of the virtual photon (and not the lepton beam direction) as shown in Fig. 2.16. The differential $d\mathcal{M}$ is a combination of the the phase-space kinematic factors and the four-fold differential:

$$d\mathcal{M} = \frac{\alpha^3 x_{Bj} y}{8\pi Q^2}(1 + \frac{4M^2 x_{Bj}^2}{Q^2})^{-1/2} dx_{Bj}\, dQ^2\, dt\, d\phi\,. \tag{2.104}$$

The single spin asymmetry yields information on the imaginary part of the interference term, written here in terms of the Dirac, F_1, and the Pauli, F_2, form factors and the amplitudes $\mathcal{H}_1, \widetilde{\mathcal{H}}_1, \mathcal{E}_1$, which are convolutions of the leading order (LO) hard scattering vertex with the GPDs. An example of this type of convolution for $\mathcal{H}_1$ and the LO hard scattering propagator is:

$$\mathcal{H}_1(\xi, t) = \int_{-1}^{1} H_q(x, \xi, t)\frac{dx}{x - \xi + i\epsilon}\,, \tag{2.105}$$

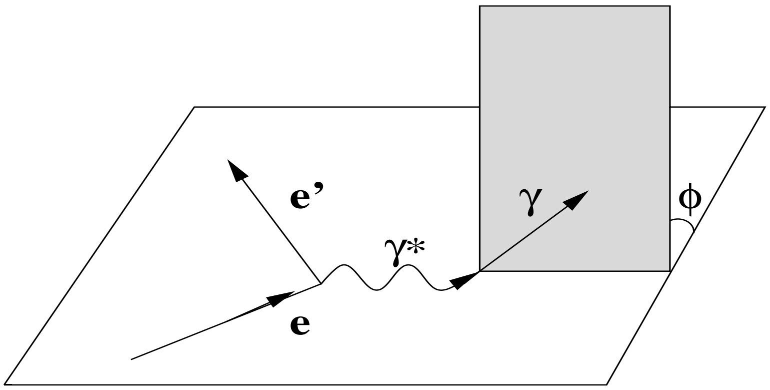

Figure 2.16: A diagram of the DVCS process illustrating the azimuthal angle ϕ.

for quark flavor q and which has both real and imaginary parts. The real parts are given by the principle value integral:

$$\Re e\, \mathcal{H}_1(\xi, t) = \mathrm{P} \int_{-1}^{1} H_q(x, \xi, t)\, \frac{dx}{x - \xi}\ . \tag{2.106}$$

The imaginary parts are given by the values of the relevant GPDs at the border point $x = \xi$:

$$\Im m\, \mathcal{H}_1(\xi, t) = -\pi H_q(x = \xi, \xi, t)\ . \tag{2.107}$$

The imaginary part of these convolution integrals (the GPD border point value) is accessible through the single spin asymmetry, the measurement of this analysis. The real part can be accessed through the measurement of the lepton charge asymmetry, which will not be performed in this analysis. Asymmetries therefore can be used to access the DVCS process in experiments where the BH process dominates. As shown in Eq. 2.103, the single spin asymmetry in leading twist has a $\sin\phi$ dependence. To extract out the amplitude of this dependence, a fit of the asymmetry as a function of ϕ can be made. Or alternatively, extracting a $\sin\phi$ moment also provides a good estimator of the amplitude of the asymmetry.

2.5 Predictions for the Single Spin Asymmetry

For the HERMES kinematic range, the DVCS process is most easily accessed via the interference term of the BH and DVCS amplitudes. The charge and single spin asymmetries constitute the observables associated with the real and imaginary parts of the interference term. Calculations using the parameterization for the GPDs show sizable asymmetries for the kinematics at HERMES [1]. The calculations for a proton target are shown for the charge asymmetry in Fig. 2.17 and for the single spin asymmetry (SSA) in Fig. 2.18 (for an electron probe) as a function of the azimuthal angle ϕ. The predictions include the BH process as well as three curves corresponding to the BH + DVCS processes. For the combined BH + DVCS processes, a leading twist (2) DVCS term, a curve corresponding to the leading twist DVCS with the additional D-term (to restore the polynomial conditions), and a curve of the DVCS including kinematic twist-3 terms (see Sec. 2.5.1) are shown as well the BH process by itself.

The prediction of Fig. 2.17 shows a cross section dominated by the DVCS process, however, the kinematics used in this calculation are not the average values at the HERMES kinematics. The value of x_{Bj} is set at 0.3 which is desirable to extract the valence quark GPDs, but does not reflect the average value of x_{Bj} at HERMES. The cross section shown in Fig. 2.18 is a prediction at the value of $x_{Bj} = 0.15$, which is closer to the average $x_{Bj} = 0.11$ value for the HERMES experimental data in the exclusive region. This cross section estimate shows the dominance of the BH process (except at out-of-plane values of the azimuthal angle ϕ).

The value of the charge asymmetry, although not at the average kinematic region for the HERMES data, predicts an asymmetry which is on the order of 10%. The charge asymmetry appears to be sensitive to the D-term and kinematic twist-3 effects (described in the following section), and may prove useful in evaluating the contributions from these effects. Although this analysis will not obtain a measurement of the charge asymmetry, the charge asymmetry analysis is in progress for the HERMES data, and preliminary results appear to be in agreement with the parameterization calculation.

The single spin asymmetry (shown in the lower panel of Fig. 2.18) predicts a large asymmetry on the order of 30% and therefore should be easily measured. The single spin asymmetry does not appear to be particularly sensitive to the D-term or twist-3 effects of the parameterization calculation at these kinematics.

2.5.1 Higher Order Corrections

The discussion of the GPDs has been made assuming an infinite momentum frame, where only the handbag diagram contributes to the non-forward Compton amplitude. In experimentally accessible regimes, there are always contributions from other non-leading diagrams. These contributions can be grouped into three major categories, the power expansion in the strong coupling constant α_s, which involve extra gluon exchanges within the active quark propagator, the inverse momentum transfer $1/Q$ expansion, which involves gluon exchanges between the active and spectator quarks, and the α_{em} expansion, which involves extra virtual photon(s) exchange(s). Other effects which involve corrections

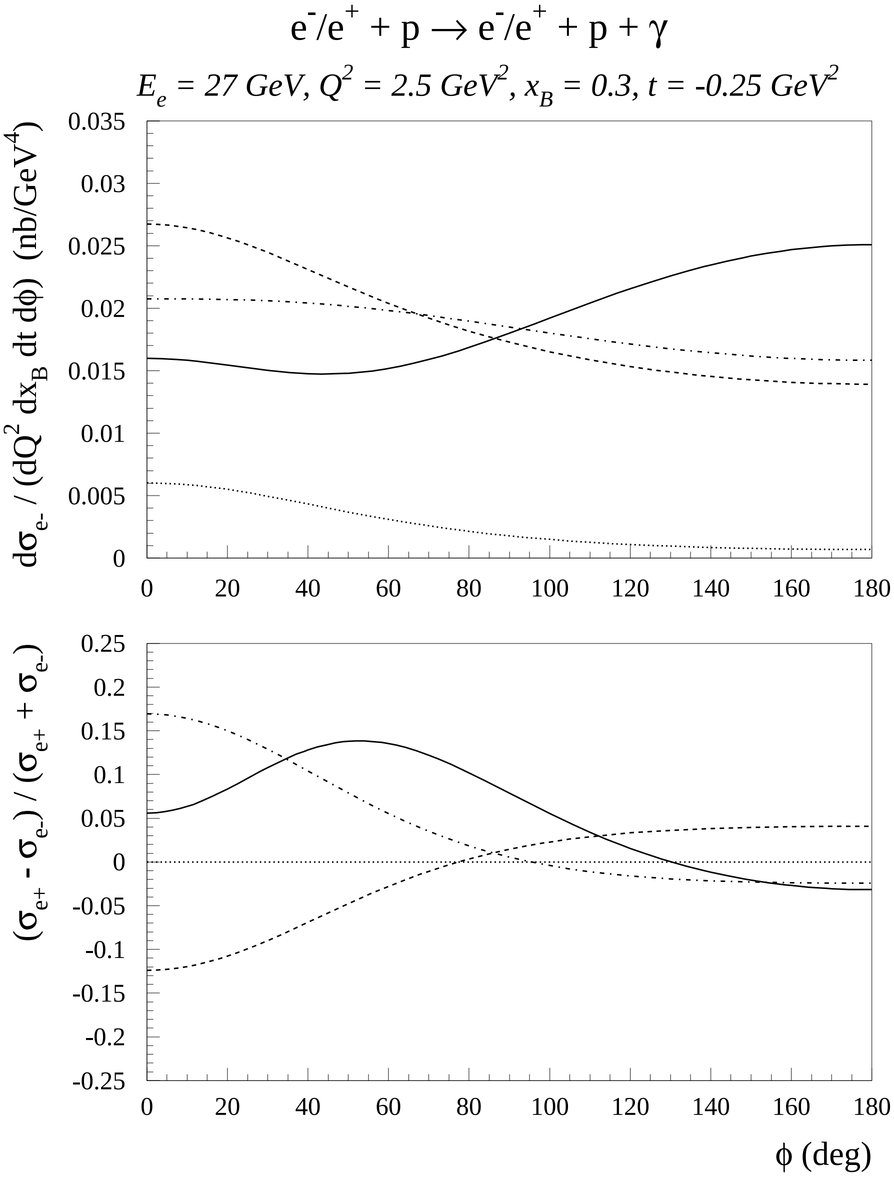

Figure 2.17: Differential cross section for the $e^- p \to e^- p\gamma$ reaction (upper panel) and DVCS charge asymmetry (lower panel) in the parameterization calculation [1]. The BH contribution (dotted) is shown along with BH+twist-2 DVCS (dashed), BH+twist-2 DVCS including the D-term (dashed-dotted), and BH+twist-2 DVCS including twist-3 and the D-term (solid). The calculation were made for a beam energy of 27 GeV, with $Q^2 = 2.5$ GeV^2, $x_{Bj} = 0.3$ and $t = -0.25$ GeV^2.

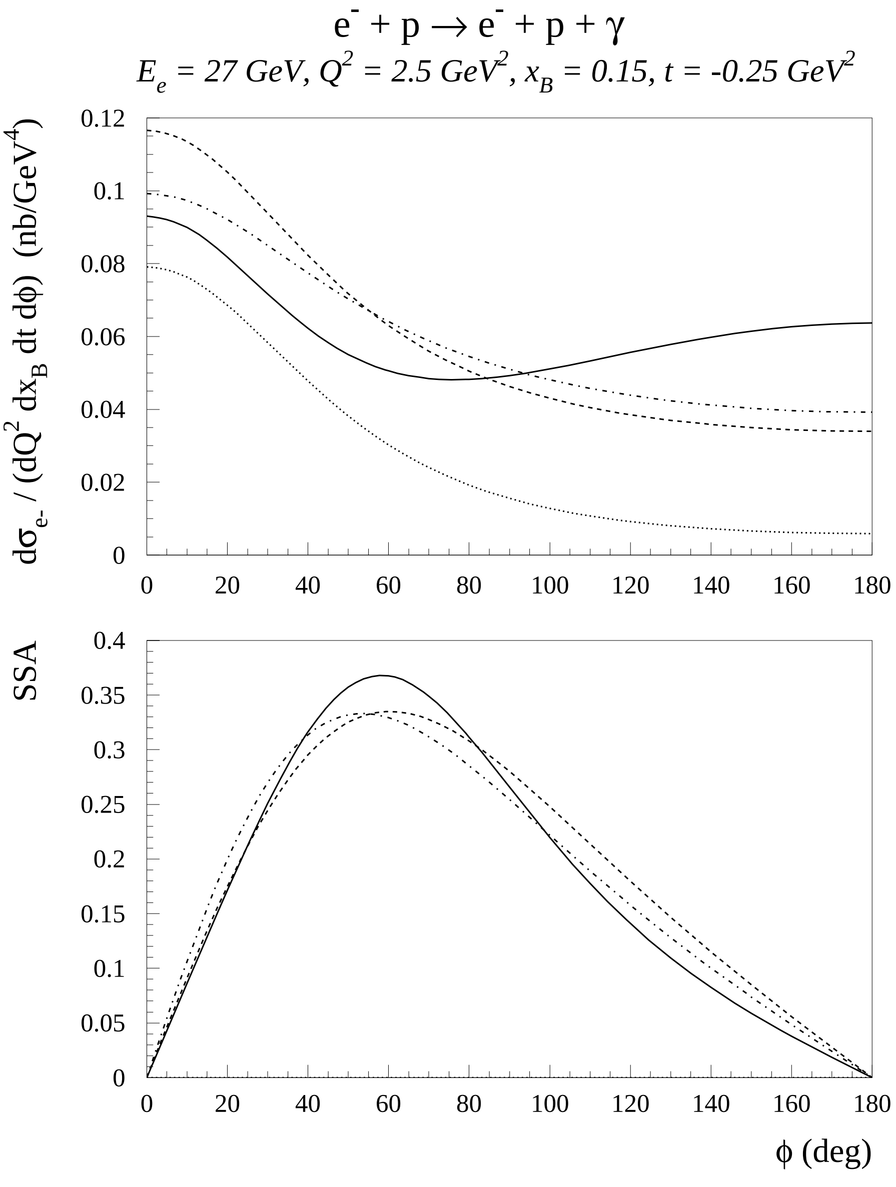

Figure 2.18: Differential cross section for the $e^-p \to e^-p\gamma$ reaction (upper panel) and DVCS SSA (lower panel) in the parameterization calculation [1]. The BH contribution (dotted) is shown along with BH+twist-2 DVCS (dashed), BH+twist-2 DVCS including the D-term (dashed-dotted), and BH+twist-2 DVCS including twist-3 and the D-term (solid). The calculation were made for a beam energy of 27 GeV, with $Q^2 = 2.5$ GeV^2, $x_{Bj} = 0.15$ and $t = -0.25$ GeV^2.

to the diagrams themselves include inherent transverse momentum of the quarks, and target mass effects. The expansion in powers of α_s is called the power expansion and is usually labeled by orders: leading order (LO), next to leading order (NLO), next-to-next to leading order (NNLO), etc. The expansion in terms of $1/Q$ is usually denoted the twist expansion. The twist expansion is one in orders of $1/Q^{\tau-2}$ where τ is the twist of the operators, yielding a twist-2 operator value for the leading Compton amplitude ($\propto 1/Q^0$). The α_{em} expansions are usually referred to QED radiative corrections, and are relatively small since $\alpha_{em} = 1/137$. The electromagnetic interaction can be calculated exactly, therefore the QED radiative corrections are usually calculated and applied to experimental data. The expansions in α_s and $1/Q$ are not so easily calculated and are therefore included in theoretical predictions for the leading terms. The handbag diagram for the Compton calculation is classified as a leading twist (twist 2) and LO (in α_s) calculation. The power and twist expansions are not independent in the non-forward kinematic regime, and care must be taken when calculating corrections. However, for the simplification of the theoretical work, the two expansions are usually assumed independent. The next-to-leading (NLO) corrections to the (virtual) photon-quark interaction of the DVCS process in the power expansion of the strong coupling constant α_s contain an extra gluon leg as shown in Fig. 2.19. These corrections have been investigated by several groups. using a minimal subtraction scheme [48] and a conformal operator product expansion [49], but will not be discussed further as they strongly depend on the model used for the GPDs. The NLO corrections are power suppressed by a factor of $1/Q^2$, and so are difficult to distinguish from the higher twist corrections which have the same suppression factor. The calculation of the higher order corrections in this case should proceed simultaneously in both expansions for a more accurate accounting.

Due to non-zero momentum transfer in the transverse direction, unlike the case of DIS, gauge invariance is destroyed even in the leading twist calculation. Gauge invariance can be simply restored in an heuristic way with the addition of an extra term. For instance, following Ref. [31], the gauge invariant tensor for DVCS can be expressed as a sum of two terms:

$$H^{\mu\nu}_{DVCS} = H^{\mu\nu}_{L.O.\,DVCS} - \frac{p^\mu}{(p \cdot q')} \left(q'_\lambda \, H^{\lambda\nu}_{L.O.\,DVCS} \right) , \tag{2.108}$$

where p^μ is the light-like, and q'_μ the real photon four-vector. The tensor $H^{\mu\nu}_{DVCS}$ respects gauge invariance for both the virtual and the real photon :

$$q_\nu \, H^{\mu\nu}_{DVCS} = 0 \, , \qquad q'_\mu \, H^{\mu\nu}_{DVCS} = 0 \, . \tag{2.109}$$

The choice of the gauge restoring term also correctly yields zero in the forward direction ($\Delta_\perp = 0$)

$$q'_\lambda \, H^{\lambda\nu}_{L.O.\,DVCS} = -\left(\Delta_\perp\right)_\lambda H^{\lambda\nu}_{L.O.\,DVCS} \, . \tag{2.110}$$

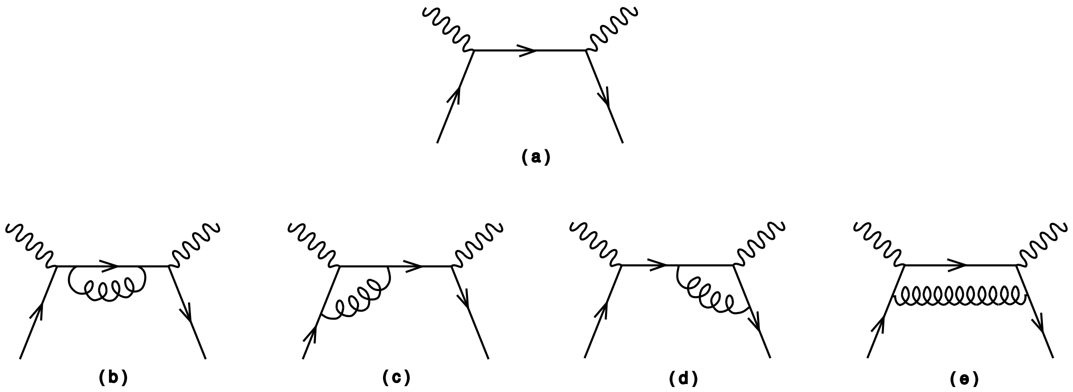

Figure 2.19: Leading order (a) and next-to-leading order corrections (b-e) for the $ep \to ep\gamma$ reaction.

Gauge invariance can also be partially restored in a more fundamental way by incorporating higher twist contributions. The next higher-order twist contributions (twist-3) can be divided into two categories, the first arising from $1/Q$ suppressed contributions from the nucleon matrix elements of quark-quarks operators (where a quark is emitted and reabsorbed into the nucleon), and the other from matrix elements of mixed quark-gluon operators (where quarks and gluon(s) are emitted or absorbed by the nucleon) [50] as shown in Fig. 2.20. The latter are characterized by diagrams which contain a gluon propagator from the hard scattering part to the non-perturbative piece of the reaction and are referred to as genuine twist-3 contributions, whereas the former are classified as kinematic twist-3 contributions. The genuine twist-3 contributions are sensitive to the quark-gluon correlations in the nucleon and are dependent on the type of reaction (ie, photon or meson production).

Kinematic twist-3 contributions have shown to be related to the four twist-2 GPDs through Wandzura-Wilcsek (WW) relations [51–53]. Assuming the genuine twist-3 corrections are small (negligible), the (kinematic) twist-3 contributions can be written in terms of the four independent GPDs of the twist-2 formalism. In this way, (kinematic) twist-3 corrections can be added to the models without introducing new GPD functions. Full gauge invariance in this case can also be restored heuristically as before with an additional gauge restoring term.

Calculations have recently been completed including all twist-3 contributions for the case of DVCS from a pion target [39]. This calculation used the MIT bag model to calculate the GPDs and predicts a large contributions from the genuine twist-3 diagram. Although modeled for a pion target and at low normalization scale, this calculation suggests the genuine twist-3 corrections are not small compared to the leading twist contributions.

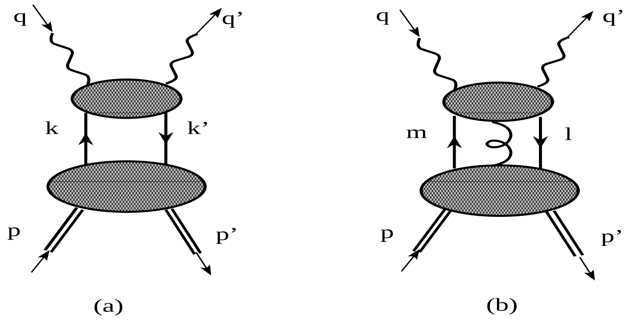

Figure 2.20: The two leading diagrams for non-forward Compton scattering. (a) contains leading twist and kinematic twist-3 contributions and (b) contains contributions of twist-3 or greater.

The QED radiative corrections to the BH and DVCS handbag diagrams have been studied in Ref. [54]. The first order QED radiative corrections to the BH and DVCS processes are one-loop corrections, which include vertex, lepton self-energy, and vacuum polarization corrections (see Fig. 2.21). The vertex corrections to the BH from the initial (V1i-V3i) and final legs (V1f-V3f) are shown, as well as the self-energy (Si, Sf) and vacuum polarization (P1i,P1f) diagrams. Fig. 2.21 also includes the vertex (V4) and vacuum polarization (P2) diagrams for the DVCS process. The vertex corrections tend to dominate the QED radiative corrections. The QED radiative corrections are usually applied to the experimental data, and will be discussed further in the analysis section of chapter 4 although, for this analysis, the QED radiative corrections were not calculated but argued to be small.

Other corrections to the DVCS and BH leading order diagrams have been investigated, including correcting for the inherent transverse momentum of quarks [31] and correcting for the target mass in the two photon exchange process [55]. The results however, are model dependent and not very illustrative without some experimental constraint on the models.

2.6 Implications for Angular Momentum

Assuming the parameterization calculation could adequately describe experimental exclusive data of the HERMES experiment, the authors of Ref. [8] investigated the angular momentum contribution of the quarks and gluons to the nucleon. Using the parameterization of the forward GPD function $e_q(x) \equiv E(x, \xi = 0, t = 0)$ (see Sec. 2.3.1), and the parton distributions as input into the Ji sum rule (Eq. 2.65) allows access to the total angular momentum of the quarks J_q:

$$J_q = \frac{1}{2} \int_{-1}^{+1} dx \; x \; [q(x) + e_q(x)]. \tag{2.111}$$

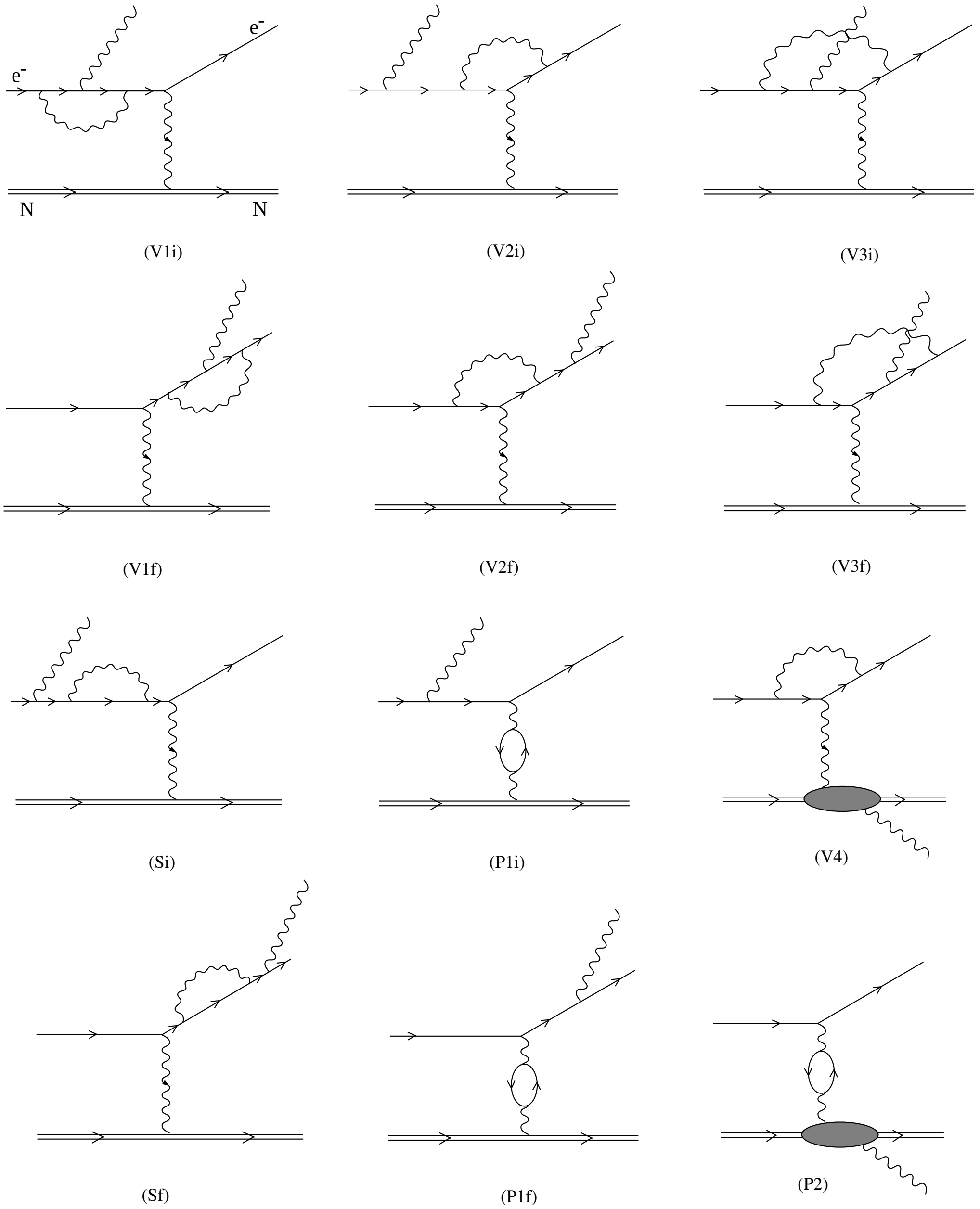

Figure 2.21: First order virtual photon radiative corrections to the $ep \rightarrow ep\gamma$ reaction.

	u	d	s	$u+d+s$
$2J_q$	0.69	-0.07	0.03	0.65

Table 2.1: Estimate of the quark total angular momentum contribution $2J_q$ to the nucleon.

A valence quark model for the function $e_q(x)$, and the MRST98 parameterization [35] at a normalization scale of $\mu^2 = 1$ GeV^2 for the parton distributions was used in this estimate. The MRST98 parton distribution parameterization uses the Modified Minimal Subtraction ($\overline{\text{MS}}$) renormalization scheme [91]. The total angular momentum ($\times 2$) contribution to the proton spin ($2J_q$) from the three lightest quark flavors were estimated in Table 2.1, as well as the sum of the three flavors. The estimate in this calculation indicates that the u-quark contribution dominates the total angular momentum of the quarks to the proton (69%), while the d and s contributions are relatively minor. The sum of the u, d, and s contributions is estimated to be 65% which is in agreement with a recent lattice QCD estimate of $2J_q = 0.60 \pm 0.14$ for the total at a scale of $\mu \approx 1$ GeV^2 [92]. It is also not inconsistent with the QCD sum rule estimate at the same scale of $2J_q = 0.30 \pm 0.26$ [93]. Using the above values for the total angular momentum of the quarks, an estimate of the orbital angular momentum contribution can be made

$$2J_q - \Delta q = 2L_q\,, \tag{2.112}$$

where the spin contribution of the quarks can be obtained from polarized DIS experiments. In Ref. [8], the total spin contribution of both quark and anti-quark contributions from the HERMES experiment [94] were used, which were evaluated at an average Q^2 scale of ≈ 2.5 GeV^2. The estimate of $2J_q$ was therefore calculated from the MRST98 parton distribution parameterizations which were evolved up to a consistent scale of $\mu^2 = 2.5$ GeV^2. The extraction of $2L_q$ is not complete as the estimated total angular momentum $2J_q$ from the parameterization calculation contains only valence quark contributions, while the measurement of the HERMES experiment for the spin contributions Δq are a sum of the valence and sea contributions (for example $\Delta q_u = \Delta u + \Delta\bar{u}$). Nevertheless, these incomplete extracted results indicate several interesting trends (see Table 2.2). First, the orbital angular momentum extracted in this manner appears to contribute only in a positive manner. Secondly, although there are 2 u-quarks in the proton, the orbital angular momentum contribution from the u-quarks to the nucleon is very small, perhaps indicating a (partial) cancellation of the orbital contribution between the two. The strange quark contribution appears to be quite small, however, the function $E(x, \xi, t)$ for the strange quark is set to zero in the parameterization calculation. Also, the experimental value

	$2J_q$	Δq (HERMES)	$2L_q$
u	0.61	0.57 $\pm$ 0.04	0.04 $\mp$ 0.04
d	-0.05	-0.25 $\pm$ 0.08	0.20 $\mp$ 0.08
s	0.04	-0.01 $\pm$ 0.05	0.05 $\mp$ 0.05
$u+d+s$	0.60	0.30 $\pm$ 0.10	0.30 $\mp$ 0.10

Table 2.2: Estimate of the quark orbital angular momentum contribution $2L_q$ to the nucleon.

used for the spin contribution is a sum of $\Delta s + \Delta\bar{s}$ and hence might be expected to small for the proton. Finally, the estimate of the orbital angular momentum contribution of the total quarks to the nucleon amounts to $\approx 30\%$ in this extraction at a scale of $Q^2 = 2.5$ GeV^2. The estimation of the total angular contribution from the quarks ($\approx 65\%$) in this parameterization calculation also indicates that the gluon contribution is about one-half of the quark contribution as:

$$\begin{aligned} & J_q + J_g = 1/2 \qquad \text{or} \\ & 2J_q + 2J_g = 1\,, \end{aligned} \tag{2.113}$$

which yields a $\sim$ 35% gluon contribution. This is relatively small compared to the Δg estimates extracted from NLO fits to DIS data. As an example, a recent NLO fit in the $\overline{\text{MS}}$ renormalization scheme at $Q^2 = 1$ GeV^2 indicates that Δg is on the order of 53% [95]. However, the fits are not well constrained as the existing data has a limited range in Q^2, and the extraction involves a scale evolution to separate the quark and gluon contributions from the DIS structure function $g_1(x, Q^2)$. Also, the extracted polarized gluon distribution from the fit strongly depends on the x-dependence of the initial parameterization. And finally, the gluon orbital angular momentum also comes into a comparison of J_g to Δg and may have a negative contribution.

The estimates of the total angular momentum of the quarks and gluons using the parameterization calculation provide some interesting observations. However, they contain several assumptions and simplifications which may be inaccurate. Perhaps the largest uncertainty is how to interpret the total angular momentum extracted from the GPDs in terms of the spin and orbital angular momenta of the quark-parton model (as was discussed in Sec. 2.2.2).

The relatively complicated GPD formalism has been reviewed in this section, illustrating the information which might be gained from the study of these functions. First, the GPDs represent correlation functions between quark of different momenta, and therefore can provide information which can not be accessed in DIS. Secondly, the GPDs provide a link between the elastic scattering form factors and the parton distributions, which may help in forming a more coherent picture of scattering over different kinematic regimes. Finally, the GPDs are sensitive to the total angular momentum of the quarks (and gluons) and so may help ascertaining the different contributions (spin and orbital angular momentum) of the quarks and gluons to the nucleon spin.

Exclusive processes provide a way to experimentally access the GPD functions. DVCS is the easiest process to describe in terms of the GPDs, and is the focus of this analysis. At HERMES kinematics however, it is difficult to extract the DVCS process from the dominant BH process which has the identical final state. For this analysis, an asymmetry with respect to the azimuthal distribution of the produced photons, with respect to the scattering plane, and the helicity of the lepton was measured. This single spin azimuthal asymmetry provides access to the imaginary part of the BH-DVCS interference term. Although the extraction of the GPDs is not possible with this one measurement, it does provide the first evidence for the validity of this method to access the DVCS process. With this evidence it is hoped that more experiments will attempt to measure the DVCS process, and along with other exclusive processes, provide for a description of the GPDs. The mapping of the GPDs in the relevant x, ξ, and t variables will provide valuable information on the correlations between quarks of different momentum and provide a more complete picture of nucleon structure.

Chapter 3

Experiment

The single photon leptoproduction data was collected at the DESY (Deutsches Elektronen SYnchrotron) accelerator facility located in Hamburg, Germany. The data for this analysis was from the 1996 and 1997 data collecting periods. The HERA (Hadron Elektron Ring Anlage) storage ring is in a circular tunnel 6.3 km in diameter which contains two beam lines, one for protons, the other for leptons. The HERMES (HEra MEasurement of Spin) experiment, located on the east side of the storage ring, is one of four experiments at DESY (see Fig. 3.1). The HERMES experiment collects data using a forward open-geometry spectrometer, separated into a top and bottom detector above and below the beam pipes. The leptons scatter from a gas target situated in the lepton beam pipe. The polarized target is created by injecting nuclear polarized gas into a storage tube coaxial with the beam. Polarization values up to 90% have been achieved for hydrogen. The lepton beam at the HERMES interaction point is longitudinally polarized, reaching typical polarization values of 55%. By utilizing the target and beam polarization, HERMES is able to gain information about the quark spin structure in nucleons.

3.1 HERA Accelerator at DESY

The two beam lines of the HERA storage ring provide leptons and hadrons for the ZEUS and H1 collider experiments. During the 1996 and 1997 running periods, the two beam lines contained protons at 820 GeV and positrons at 27.6 GeV, circulating in opposite directions. Before 1998, positron beams were primarily used, since they are less disturbed by minute amounts of positively ionized dust in the beam pipe. The beam lines are separated by a distance of 72 cm at the HERMES experiment with the lepton beam located on the inner side of the ring. The HERMES spectrometer is centered along the lepton beam line, with the proton beam line offset.

The positron beam was injected into HERA from a pre-accelerator (PETRA), up to a typical current of 35 mA and was then maintained until the current was reduced by the experimental target

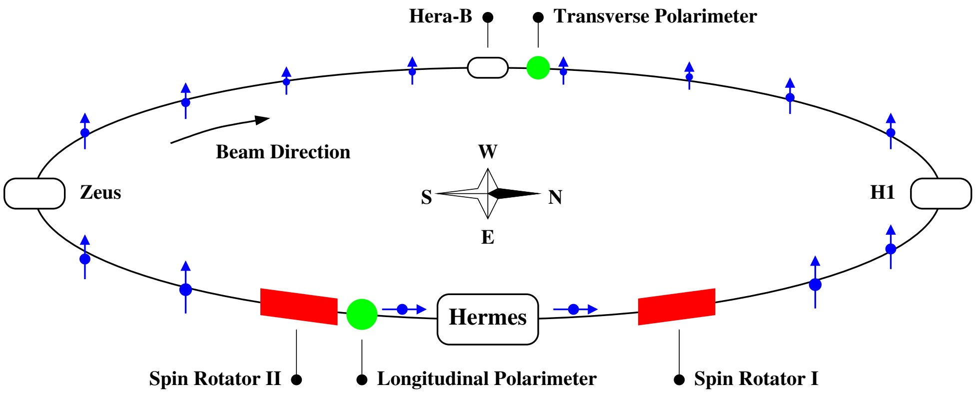

Figure 3.1: The HERA storage ring. The four experiments are shown as well as the position of the spin rotators and polarimeters.

interactions to a value of about 10 mA, when it was ejected from the beam line. The average rate of beam loss results in a data collection period of approximately 12 hours. The positron beam is formed of 'bunches' of positrons with a pulse width of 29 ps (5.4 mm) separated by 96 ns. Each bunch contains approximately 3.8×10^{10} positrons. There are 210 bunches for a fully loaded ring, subdivided into three groups which are separated by time gaps longer than 96 ns to allow for background studies. The transverse profile of the positron beam is elliptical, with an average height of 0.07 mm and width of 0.26 mm.

The positron beam is self-polarizing due to the Solokov-Ternov effect [56]. This self-polarization is due to a small asymmetry in the spin flip amplitude of synchrotron radiation. The synchrotron radiation is produced by the acceleration of the beam as it bends in the field of the ring magnets. For the majority of the time, the synchrotron radiation does not flip the spin of the positron, however, there is a small amplitude to flip the positron spin and this spin flip amplitude has a small associated asymmetry. In a uniform magnetic field the asymmetry results in a polarization parallel to the magnetic field (for positrons) which is transverse to the momentum of the positrons. The spin flip amplitude is suppressed by about 10 orders of magnitude compared to the non-spin flip amplitude, therefore the polarization takes time to develop. The development of the polarization follows an exponential rise, with a rise time of about one-half hour at the HERA accelerator ring (see Fig. 3.2). The theoretical polarization limit for the HERA positron beam is 92%, however, depolarization effects result in a smaller experimental value, typically on the order of 55% (see Fig. 3.2). The depolarization effects include non-uniformity of the magnetic fields due to slight mis-alignment of the bending magnets, spin diffusion from the synchrotron radiation process, and depolarization resonances. Spin diffusion is a result of oscillations (synchrotron and betatron) which are shifts in the energy and position of the

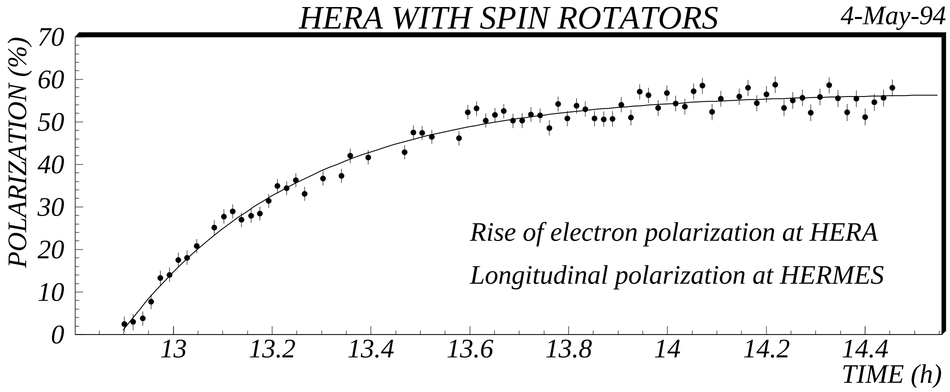

Figure 3.2: Longitudinal polarization values measured in the HERA positron ring. The curve which is a fit to the data, shows the rise time and the peak polarization achieved with spin rotators.

positron when it radiates a photon. These shifts result in spin tilts from the horizontal magnet field of the quadrapoles. The spin tilts add incoherently leading to a diffusion of the spin orientations and a decrease of the polarization value. Depolarization resonances refer to the large depolarization effects arising when the oscillations from the radiation process are in resonance with the spin precession frequency. The depolarization effects are minimized at HERA using a process of harmonic correction bumps [57].

Spin structure functions are accessed using a longitudinal beam, therefore, the spin of the transversely polarized beam needs to be rotated before entering the HERMES experiment. It is rotated back after the HERMES experiment, in order to maintain the polarization via the Solokov-Ternov effect. This is accomplished with spin rotators, devices which use horizontal and vertical bending magnets in sequence to rotate the lepton spin by 90 degrees. The spin rotators at HERA were the first spin rotators to function in a storage ring [58]. The spin rotators are precisely calibrated to ensure an exact 90 degree rotation transferring all the polarization from transverse to longitudinal. To eliminate depolarization of the longitudinal polarization from a bending magnetic field, the section between the spin rotators is composed of a nearly straight beam line.

The polarization of the beam is continually monitored by two polarimeters using the Compton backscattering of polarized light (provided by lasers). One polarimeter is located just downstream of the HERMES experiment in the section between the spin rotators (see Fig. 3.1), and measures the longitudinal polarization. The other polarimeter is located on the opposite side of the ring (the west side) and measures the transverse polarization.

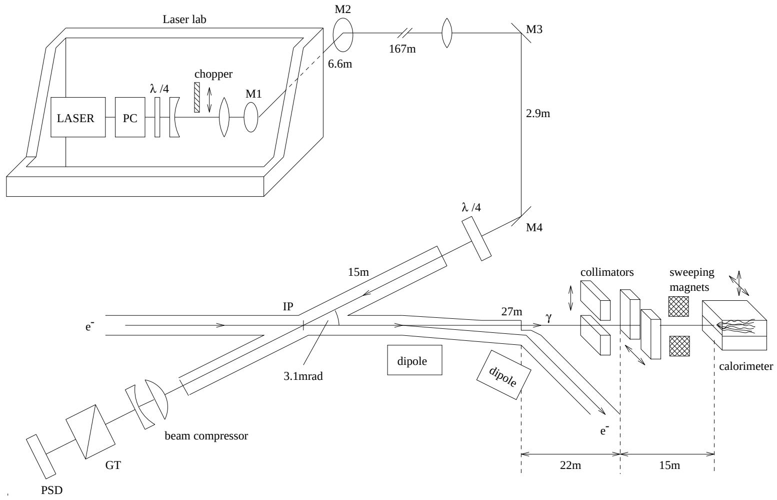

Figure 3.3: Schematic of the transverse polarimeter showing the laser source, Pockels cell (PC), beam interaction and the polarimeter calorimeter.

3.1.1 Transverse Polarimeter

The source of polarized light for the transverse polarimeter is a 10 W argon-ion laser, which provides a continuous beam of circularly polarized light. The polarization of the photons is flipped using a Pockels cell (PC) at a frequency of 90 Hz to reduce any systematic effects. The setup of the polarimeter is shown schematically in Fig. 3.3. The energies and positions of the backscattered photons are measured by a tungsten-scintillator calorimeter situated 65 m downstream from the interaction point. The calorimeter is divided horizontally into two segments. An asymmetry in the energies from the top and bottom segments

$$\eta(\langle y \rangle) = (E_{upper} - E_{lower})/(E_{upper} + E_{lower}) \, , \tag{3.1}$$

allows an estimate of the mean vertical position $\langle y \rangle$ of the backscattered photon in the calorimeter. The polarization can then be determined by the difference in the mean vertical position of left and right circularly polarized light:

$$\delta\langle y \rangle (E_\gamma) = \frac{1}{2}(\langle y \rangle_L - \langle y \rangle_R) \propto P_y \, . \tag{3.2}$$

3.1.2 Longitudinal Polarimeter

At the location of the HERMES experiment in the east hall, where the beam is longitudinally polarized, there are bremsstrahlung photons arising from the interactions of the positron beam and

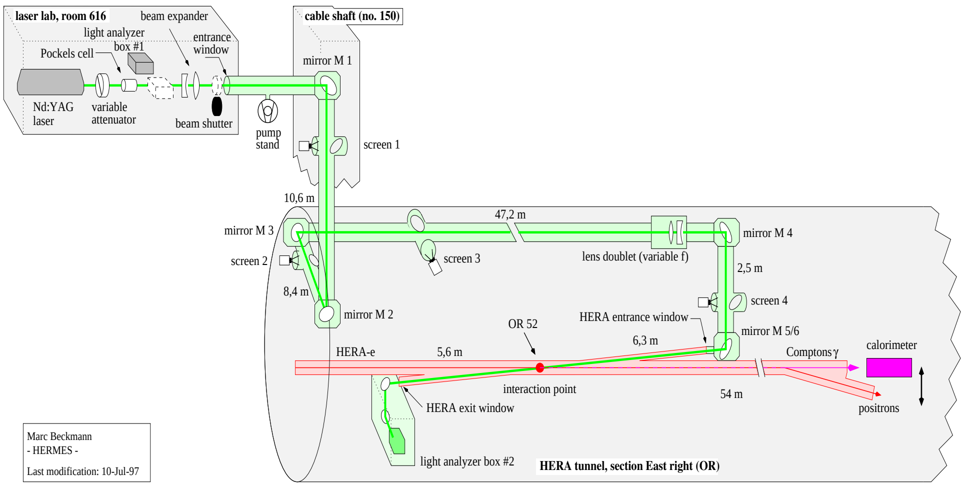

Figure 3.4: Schematic of the longitudinal polarimeter showing the laser source, Pockels cell (PC), beam interaction and the polarimeter calorimeter.

target. To reduce the effect of this background to the backscattered photons, a more powerful source of circularly polarized light, in the form of a pulsed Nd:YAG laser, is used. As with the transverse polarimeter, a Pockels cells is used to switch the polarization of the photons (at 89 Hz). The backscattered photons are measured 54 m downstream of the interaction point using four $NaBi(W0_4)$ Čerenkov crystals, arranged in a 2×2 array. A schematic view of the longitudinal polarimeter setup is shown in Fig. 3.4. Photons from the laser are backscattered from the lepton beam and an asymmetry of the energy distribution of the backscattered photons in the calorimeter is measured. This asymmetry is proportional to the longitudinal polarization ($A(E_\gamma) \propto P_z$) and is therefore used to measure the value of the longitudinal polarization of the beam.

3.2 Internal Gas Target

The HERMES target is an integral part of the positron beam pipe and utilizes elemental gas particles for the target interactions. The target cell is 40 cm long and has an elliptical profile of 9.8 mm high and 29 mm wide which mirrors the beam profile. A schematic view of the target cell is shown in Fig. 3.5. The cell wall material is very thin aluminum (75 μm). The target cell is mounted inside a vacuum chamber which has a 0.3 mm stainless steel foil exit window. The wall material and exit window were as thin as possible to allow scattered particles to escape the target region with minimum disturbance. The ends of the target cell are open to allow the positron beam to pass through the target cell, interacting solely with the target gas. The target gas is injected via a tube at the center of the cell. The gas target thickness is approximately 100 times greater than compared to a free gas jet

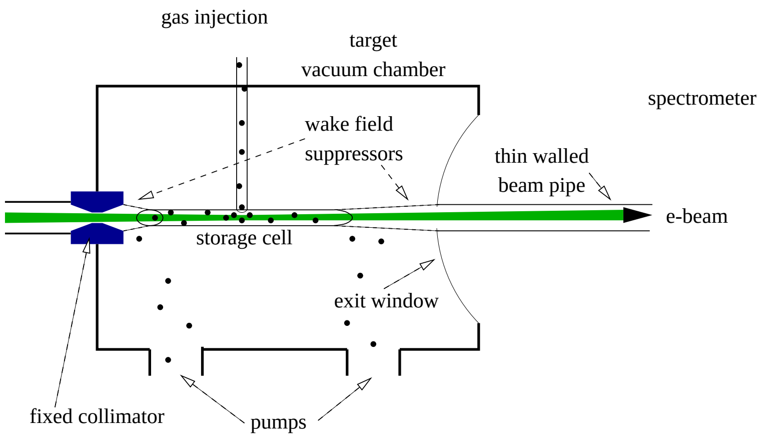

Figure 3.5: Schematic of the target cell. The C2 collimator is shown on the upstream side of the target. Wake field suppressors consisting of small metal tubes are used to join the target cell to the beam pipe and reduce heating from the wake fields.

crossing the beam [59], since the interaction probability with the beam is large as the particles bounce off the walls numerous times before exiting the cell at either end. The density of the gas is increased by cooling the target cell to 100 K, which reduces the velocity of the target gas particles and increases the occupancy time in the cell.

On both ends of the target cell vacuum pumps remove the residual target gas out of the beam pipe and maintain the vacuum needed for the positron beam. The cell is protected from synchrotron radiation by two sets of collimators. The first set of collimators (C1) are located 2 m upstream of the target and are movable to allow injection and tuning of the beam. The C1 set consists of two collimators, one split horizontally, the other vertically, which are closed during data taking and reduce the synchrotron radiation accompanying the positron beam. The second collimator (C2) is situated just upstream of the target (see Fig. 3.5). It is designed to stop any radiation reflected from the C1 collimators.

The HERMES target uses polarized as well as unpolarized gases. Helium-3, hydrogen and deuterium have been used as polarized targets. Unpolarized targets of these same gases as well as nitrogen and krypton have been used. For this analysis, only data collected using the hydrogen target were used which included both the polarized and unpolarized hydrogen target gases. The target polarization from the polarized hydrogen target has been averaged (summed) over the polarization values. Since the polarized target switched polarizations states randomly every 1-2 minutes and has a rather stable polarization, summing over the polarization states effectively results in an unpolarized target.

The polarized hydrogen target was used in 1996 and 1997. The source of polarized hydrogen consisted of a dissociator used to create atomic hydrogen plus permanent magnets and radio-frequency transmissions used to select the hyperfine states of hydrogen with the desired helicity. The initial injected polarization was typically on the order of 95%. A magnetic field was maintained in the target to provide a quantization axis for the polarized gas. The initial polarization of the atomic hydrogen could be diluted from recombination of atomic into molecular hydrogen, cell wall collisions and spin exchange collisions. The polarized hydrogen gas in the target was analyzed with a target gas analyzer (TGA) to measure the fraction of the hydrogen in atomic form. A Breit-Rabi Polarimeter measured the polarization of the atomic hydrogen. Combining the measurement of the TGA and BRP allows a calculation of the hydrogen target polarization:

$$P_T = \alpha_0 \left[\alpha_r + (1-\alpha_r)\beta\right] P_T^{atom}\,, \tag{3.3}$$

where α_0 is the initial atomic fraction, α_r is the atomic fraction measured by the TGA, β is the (estimated) polarization of the recombined molecules and P_T is the polarization of the atomic hydrogen from the BRP. The target polarizations were typically between 85 and 90% with a density of 7×10^{13}nucleons/cm^2. More information on the polarized target can be found in Refs. [59–61].

The unpolarized hydrogen gas was fed from bottles of pure H2 gas through a thermo-valve and diaphragm system, which provides a constant density on the order of 10^{15}nucleons/cm^2 into the target cell. The higher density of the unpolarized target allows calibration measurements of the target and spectrometer to be made in a relatively short time, as well as providing data for unpolarized analyses.

3.3 HERMES Spectrometer

The HERMES spectrometer is an open-geometry spectrometer, split into two identical halves, one situated above the accelerator beam pipes and the other below. The acceptance covers scattering angles of ± 170 mrad in the horizontal direction and $\pm(40-140)$ mrad in the vertical direction. The momenta of the charged scattered particles is measured using a series of tracking chambers and a dipole magnet. Charged particle identification (PID) is accomplished with four detectors, a gas threshold Čerenkov detector (upgraded to a ring-imaging Čerenkov in 1998), a transition radiation detector, a preshower detector and an electromagnetic calorimeter. Photon energies and positions are measured in the electromagnetic calorimeter as well. A detailed description can be found in [62] and a side view schematic of the spectrometer is shown in Fig. 3.6.

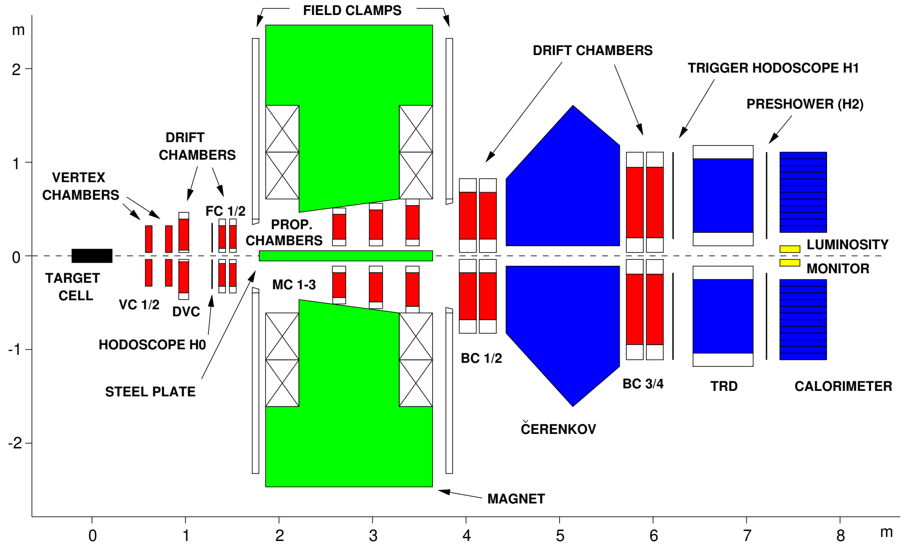

Figure 3.6: Schematic side view of the HERMES spectrometer.

3.3.1 Tracking Detectors and Magnet

In order to achieve sufficient resolution of the charged particle kinematics, multiple tracking devices are needed in conjunction with a large magnetic field. The tracking chambers consist of micro-strip vertex detectors (the vertex chambers), drift chambers including the drift vertex chambers (DVC), the front chambers (FC), and the back chambers (BC), and finally multi-wire proportional chambers located in the magnet (the magnet chambers or MC). The vertex chambers are micro-strip gas chambers which are composed of anode strips sputtered and etched on a glass substrate at 193 μm intervals. A foil cathode plane is situated near the substrate, and the gap in-between filled with an ionizing gas mixture of DME/Ne(50:50). A voltage difference of $\sim$ 600 V is maintained between the cathode plane and substrate. A particle traversing through the micro-strip gas chamber ionizes the gas leaving a track of ionized particles. The ionized particles drift to the anode strips inducing a charge which forms the signal for the amplifier electronics. The small cell size results in a position resolution on the order of 80 μm. The drift chambers use the same principle of ionized particles drifting to an anode forming the signal, but with a larger cell size. The drift chambers are formed with two cathode foil planes with alternating cathode and anode wires in the middle of the foils. The wires are separated by a distance of 0.6 cm (0.7 cm) for the DVC (FC) front drift chambers and 1.5 cm for the back drift chambers. The ionizing gas is a mixture of Ar/C0_2/CF$_4$(90:5:5) and the voltage difference between the cathode and anode maintained at $\sim$ 1500 V. A traversing charged particle will ionized the gas, the ionized particles will drift to the anode and induce a charge, resulting in a signal to the amplifier

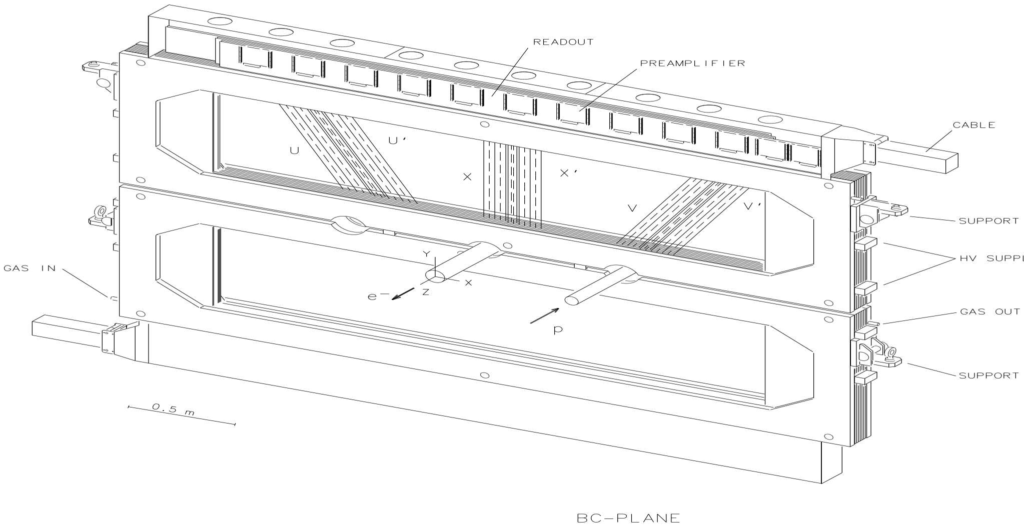

Figure 3.7: A schematic of the top and bottom sections of one BC module.

electronics. Drift chambers can give accurate positions transverse to the wires by measuring the time difference between the trigger of the event and the signal in the wire (drift time). An average position resolution of ~ 250 μm is obtained with the HERMES drift chambers. The tracking chambers are only able to measure the transverse position from a sense wire, and therefore three different sets of detector planes are used to measure the track position along three different axes, along the horizontal axis (the X-axis), along an axis 30 degrees above the horizontal axis (the U-axis), and along an axis 30 degrees below the horizontal axis (the V-axis). A cut-away drawing of the back chambers is shown in Fig. 3.7, illustrating the wire orientation. The transverse measurement in the tracking chambers has an inherent ambiguity as the particle could have crossed by either side of the sense wire. For the VC's, since the micro-strips are all anodes, the track position is determined from a weighted average of several micro-strip signals, eliminating the left-right ambiguity. To eliminate the left-right ambiguity for the drift chambers, another set of planes with offset wires is used. The offset planes have the wires offset by one-half the cell width. The tracking chambers are divided into top and bottom sections, for convenience only the top tracking chambers will be described, with the bottom chambers implied. The information for each projection is combined to form a two dimensional track, the two-dimensional tracks are then combined to make the final three dimensional reconstructed track.

The vertex chambers consist of two modules (VC1 and VC2). Each module consists of three planes of glass substrate inter-spaced with the cathode foils. The micro-strip gas chamber method of construction allows for a smaller cell size which increases the position resolution, and eliminates the need for a frame so that the active area can be positioned closer to the beam pipe. For these reasons the vertex chambers are placed next to the target and provide the best vertex resolution.

Other tracking detectors in the front region are the DVC and FC chambers. The DVC consists of one module with six drift planes in three projections (X,X', U,U', and V,V'). There are two modules in the FC, each containing the six planes as in the DVC's, for a total of twelve planes. This results in four FC planes for each projection. In 1996, the tracking in the front region was accomplished by the FC's as the DVC's and VC's were still being commissioned. In 1997, the VC's and FC's were used for the tracking (the DVC's still being tested), which improved the vertex resolution.

A dipole magnet is situated between the front and back tracking chambers which allows a precise determination of the charged particle momentum. The field has a deflecting power of $1.3\mathrm{T}\cdot\mathrm{m}$. To minimize the magnet field outside the physical magnet, large iron plates are used as field clamps on the upstream and downstream magnet faces. In the middle of the magnet a large iron septum plate is used to ensure a negligible magnetic field in the beam pipe area. The septum plate defines the minimum angular acceptance (40 mrad) in the vertical direction, and the pole faces determine the maximum acceptance (140 mrad).

The magnet proportional chambers (MC) are located inside the magnet. They are used to resolve any ambiguity for events with high track multiplicity, and to measure the position of low energy tracks which are bent out of the acceptance by the magnet and not detected in the back detector. Since the single photon analysis uses events with only one scattered positron track having a front and back partial track, the magnet chamber information was only used to reject events containing an additional short track (not detected in the back region).

Downstream of the magnet are the BC drift chambers. They consist of four modules, separated into two sets by the Čerenkov detector. The separation provides a large lever arm to decrease the uncertainty in the track parameters, and the four modules contribute a total of twenty-four planes, or eight planes in each X, U, and V projection.

The combination of the tracking chambers and the magnet allow a momentum resolution ($\Delta P/P$) of less than 1.5% and an angular resolution of less than 0.6 mrad over the entire kinematic range of the HERMES spectrometer. The different characteristics of the tracking chambers are shown in Table 3.1.

3.3.2 Particle Identification

The HERMES spectrometer uses a combination of four particle identification detectors to separate leptons from hadrons and to separate out pions from the hadron sample. The probability to produce a pion at the event vertex is much higher than the probability to produce any other hadron

CHAMBER	Vertex		Drift Vertex	Front		Magnet			Back	
Detector name	VC1	VC2	DVC	FC1	FC2	MC1	MC2	MC3	BC1/2	BC3/4
mm from target	731	965	1100	1530	1650	2725	3047	3369	4055	5800
Active Area:										
Horizontal (mm)	323	393	474	660	660	996	1210	1424	1880	289 0
Vertical (mm)	137	137	290	180	180	263	306	347	520	710
Cell design	microstrip gas		horizontal-drift	horizontal-drift		MWPC			horizontal-drift	
Cell width (mm)	0.193		6	7		2			15	
A-C plane gap (mm)	3		3	4		4			8	
Anode (A) material	200 μm glass(Al)		W(Au)	W(Au)		W(Au)			W(Au)	
Anode wire diameter	7 μm		30 μm	20 μm		25 μm			25 μm	
Potential wire mat$'$l	Al strip		Be-Cu(Au)	Al(Au)					Be-Cu(Au)	
Potential wire dia.	85 μm		50 μm	50 μm					127 μm	
Cathode (C) material	Al on glass		Al on Mylar	Al on Mylar		Be-Cu wires			C on Kapton	
Cathode thickness	200 μm		34 μm	6.4 μm		90 μm @ 0.5 mm pitch			25.4 μm	
Gas composition:	DME/Ne		$Ar/CO_2/CF_4$	$Ar/CO_2/CF_4$		$Ar/CO_2/CF_4$			$Ar/CO_2/CF_4$	
(%)	50/50		90/5/5	90/5/5		65/30/5			90/5/5	
U,V stereo angle	$+5°, -90°$		$\pm 30°$	$\pm 30°$		$\pm 30°$			$\pm 30°$	
Resolution/plane (σ)	65 μm		220 μm	225 μm		700 μm			275 μm	300 μm
Wires in X plane	1674	2046	80	96	96	496	608	720	128	192
Wires in U,V plane	2170	2170	96	96	96	512	608	720	128	192
Module config.	VUX	XVU	XX$'$UU$'$VV$'$	UU$'$XX$'$VV$'$		UXV			UU$'$XX$'$VV$'$	
Rad. length/module	0.8%		0.25%	0.075%		0.29%			0.26%	
Number of modules	1	1	1	1	1	1	1	1	2	2
(upper or lower)										
Channels/module	6014	6386	544	576	576	1520	1824	2160	768	1152
Total channels	24800		1088	2304		11008			7680	

Table 3.1: Tracking Chamber properties.

for the kinematics at HERMES, therefore the separation of pions from positrons is given the most consideration. The transition radiation detector provides the best separation for most detected particles of the four detectors, followed by the calorimeter and preshower. Due to the ~ 4 GeV threshold of the gas mixture, the positron-pion separation is limited in the Čerenkov detector.

The transition radiation detector (TRD) detects the radiation produced from a highly energetic charged particle as it moves from one medium to another. The TRD consists of six modules, each constructed of a radiator followed by a proportional wire chamber to detect the transition radiation. The radiator is a volume of 325×75 cm^2 $\times$ 6.5 cm thick filled with propylene fibers having a diameter of ~ 20 μm. The propylene fibers cause energetic positrons to emit radiation in the X-ray range. Energetic hadrons, with a heavier mass, do not produce significant radiation from the fibers. The proportional wire chamber is a volume 2.54 cm thick containing 256 wires spaced by 1.27 cm and filled with a gas mixture of Xe/CH_4(90:10) which is an efficient absorber of X-rays. Although the hadrons will deposit some minimizing ionization energy in the proportional chamber, the signal from the X-rays produced by leptons is much larger allowing a separation of leptons and hadrons.

The electromagnetic calorimeter consists of two sections, one for the top and bottom detector. Each section is constructed of a 42×10 array of F101 lead glass blocks [63] with a size of 9×9 cm$^2 \times 50$ cm long. The blocks are optically isolated using a wrapping of aluminized mylar foil and opaque black tedlar foil. Each block is optically connected to a photomultiplier tube (PMT) which measures the light generated when a particle traverses the lead glass. A particle traversing a medium with a refractive index n will emit electromagnetic (Čerenkov) radiation if its velocity (v) is greater than the phase velocity of light (v_{ph}) in that medium: $v > v_{ph} = c/n$ (where c is the speed of light in a vacuum). When an energetic electron is incident on the lead glass, an electromagnetic cascade is started from the production of a (Čerenkov) radiated photon. The photon then creates leptons through pair production which in turn produce lower energy (Čerenkov) photons. This cascade or shower production of photons and leptons continues until the particles have insufficient energy to produce more particles. The 50 cm length of the glass blocks corresponds to ~ 18 radiation lengths, which is the best balance between shower containment of a typical HERMES lepton and the loss of light due to attenuation. To reduce the effects of radiation damage, each section of the calorimeter is moved away from the beam line during beam injection. As the calorimeter is the detector most sensitive to photons, a more detailed description of the calorimeter will follow in Section 3.6.

To maximize the lepton-hadron seperation ability of the calorimeter, a preshower detector was constructed just upstream of the calorimeter. The preshower consists of an 11 mm lead sheet (2 radiation lengths), followed by an array of hodoscope paddles. The hodoscope paddles are 42 $\times$

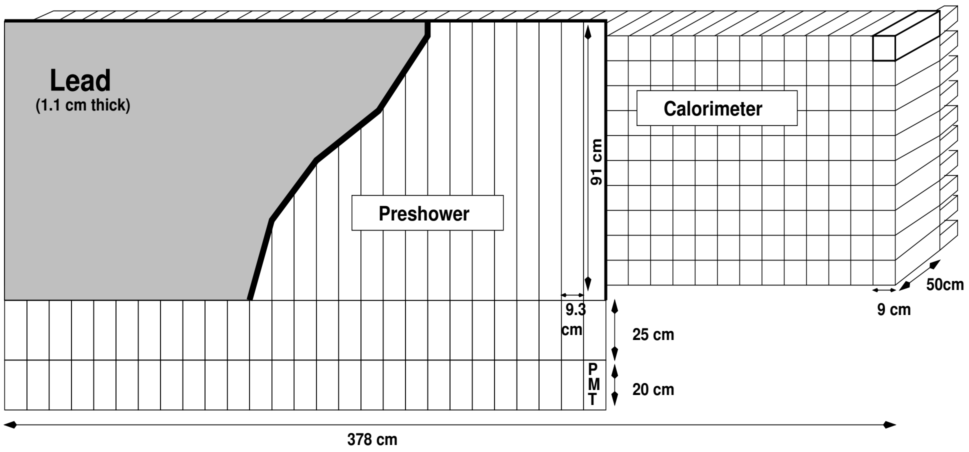

Figure 3.8: Schematic view of the preshower counter and calorimeter showing the alignment of the preshower hodoscope paddles in relationship to the calorimeter blocks.

9 cm^2 $\times$ 1 cm thick plastic scintillators optically isolated and connected to photomultiplier tubes. The majority of positrons will begin to create electromagnetic showers while passing through the lead sheet, and will typically deposit $\sim$ 30 MeV in the hodoscope paddles. The energy deposition is greater than the minimum ionization energy of $\sim$ 5 MeV, which would be deposited by hadrons. The energy deposited in the hodoscope is a small fraction of the typical particle energies and is therefore only a small correction to the energy measurement in the calorimeter. Used in conjunction with the calorimeter, the ratio of the total number of hadrons to misidentified hadrons is $\sim 5 \times 10^3$ (hadron rejection factor) [64]. A schematic view of the calorimeter and preshower counter is shown in Fig. 3.8

A threshold Čerenkov detector consists of a radiator which has a radiation threshold dependent on the velocity of the traversing particle. The HERMES Čerenkov detector uses a gas mixture of C_4F_{10}/N_2 in a (30:70) ratio, which sets a threshold of 4 GeV for pions to emit Čerenkov photons. Since the HERMES trigger requires a minimum value of 3.5 GeV for positrons, the Čerenkov detector can only discriminate between positrons and pions in a very limited range. The main purpose of the Čerenkov detector is to discriminate between pions and heavier hadrons, which however, is not important for the single photon analysis.

The typical distributions for the different PID detectors are shown in Fig. 3.9, which illustrates the discrimination ability between pions (hadrons) and positrons for each detector. As mentioned previosly, the TRD provides good discrimination, along with the calorimeter. The preshower and Čerenkov detector do not individually provide a clean separation between the hadrons and positrons, however, when used in conjuction with the other PID detectors, do contribute to the overall particle identification.

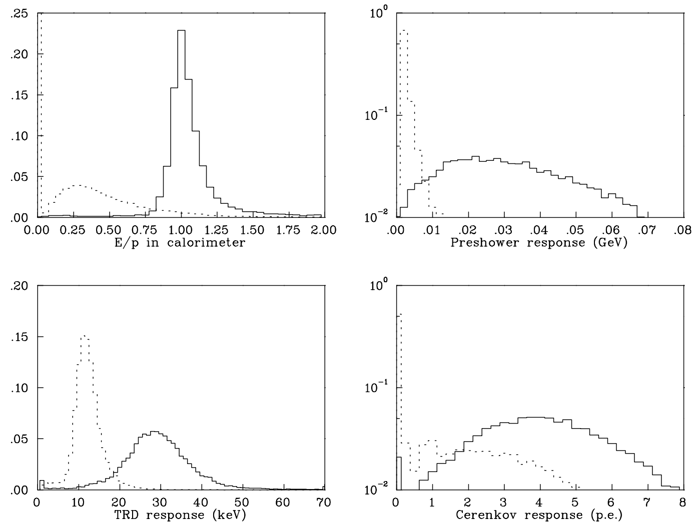

Figure 3.9: Typical positron (solid) and hadron (dotted) distributions of the PID detectors.

The four PID detector responses can be combined using separate constraints on each detector. A more efficient method is to use a likelihood method to combine the detector responses before imposing any constraints. For one detector, the PID likehood function is a logarithmic fraction of the conditional probability that the particle is a hadron (h) or a positron (p) with a correction factor determined by the type of interaction process:

$$PID = log_{10}(\frac{L^p}{L^h}) - log_{10}\Phi \,. \tag{3.4}$$

Here, the variable Φ is the ratio of the fluxes for the two different particle types which is governed by the interaction process. The likelihood functions for each detector are determined from the data, using very strict constraints to insure a pure sample. These 'parent' distributions are parameterized as functions of momentum for the HERMES experiment. The likelihoods for the Čerenkov detector, the preshower and the calorimeter were combined into one likelihood as:

$$PID3 = PID_{cer} + PID_{pre} + PID_{cal} = log_{10}(\frac{L^p_{cer}L^p_{pre}L^p_{cal}}{L^h_{cer}L^h_{pre}L^h_{cal}}). \tag{3.5}$$

The dependence of the likelihood on the flux ratio Φ has been dropped in Eq. 3.5 so the same PID3 value will be obtained for different physical processes, such as DIS and photoproduction. The combined PID3 value is consistent with what one would expect from a single PID detector with very good particle identification. The TRD detector likelihood values were historically separated from the other three detectors as the TRD parent distributions were not very well understood at the beginning of the data

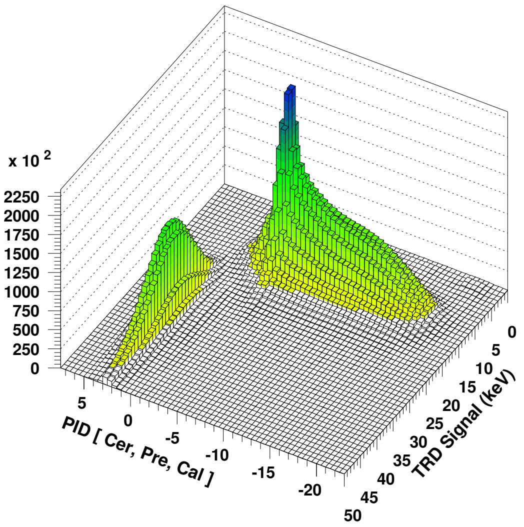

Figure 3.10: The PID3 likelihood value versus the energy deposition in the TRD. The positron and hadron peaks show a clear separation from each other.

production. The TRD likelihood is formed as:

$$PID5 = PID_{TRD} = log_{10}\frac{L^{e}_{TRD}}{L^{h}_{TRD}}. \tag{3.6}$$

The PID3 likelihood values are plotted against the TRD response (see Fig. 3.10), illustrating the clean separation between the hadrons and the positrons using the four particle identification detectors.

The four PID detectors are combined using a simple addition of the logarithms (PID3 + PID5). A positive value of the PID sum indicates a likely positron, a negative value a hadron. To minimize any hadron contamination a value of PID3 + PID5 $>$ 2 was used for the single photon analysis which is equivalent to the particle being at least 100 times more likely to be a positron than hadron. The estimated amount of possible hadron contamination will be discussed in Sec. 4.4.1.

3.4 Luminosity Monitor

The luminosity monitor at HERMES uses the Bhabha scattering process of the positrons from the electrons of the target gas. The cross section is well known and precisely calculable for this process from quantum electrodynamics (QED), so an absolute measurement of the luminosity is possible, however, for most measurements of asymmetries, including this analysis, only a relative luminosity between different spin states is needed. The luminosity monitor is constructed of two calorimeters mounted to the left and right of the positron beam line, 7.2 m downstream of the target. Each calorimeter section is constructed of twelve $NaBi(WO_4)_2$ crystals having dimensions of 22×22 mm^2 $\times$

200 mm in length. Each crystal is optically isolated using aluminized mylar foil, and connected to a photomultiplier tube. The array setup allows an acceptance in the horizontal direction of 4.6 to 8.9 mrad, adequately covering the detection of the symmetric Bhabha events in which the e^+ and e^- each have a scattering angle of 6.1 mrad. A Bhabha event is selected if there is a simultaneous response in both the left and right calorimeters, each having an energy sum greater than 5 GeV. The energy constraint reduces the dominant background of DIS scattered positrons, for which the calorimeter sections receive an asymmetric energy deposition. As with the main calorimeter, the luminosity monitor is moved away from the beam pipe during injection to reduce the radiation damage. A statistical precision of $\sim 1\%$ is reached in roughly 100 seconds, and the systematic uncertainty on the absolute luminosity is about 6% [65].

3.5 Triggers

The main trigger used in the HERMES experiment is designed to initiate the spectrometer readout when a scattered positron traverses the detector. This trigger allows a readout of all DIS events in the acceptance and is called the DIS trigger (trigger 21). The DIS trigger consists of a five-fold coincidence between three hodoscope detectors, the calorimeter (see Fig. 3.6), and a timing signal for the incident positron bunch. For the hodoscopes and calorimeter, the coincidence must also occur in either the top or bottom spectrometer half. A minimum ionizing particle (hadron) would deposit ~ 0.8 GeV of energy in the calorimeter; to ensure that a positron shower has occurred and to reduce the amount of unusable data written to data storage media, a threshold of 3.5 (1.4) GeV was set on the calorimeter column sums for unpolarized (polarized) targets. Since the majority of a scattered positron's energy will be deposited within a 2×2 array of calorimeter blocks, the energy sum of two complete columns of the calorimeter provides a fast energy signal for threshold discrimination. The threshold insures that a triggered positron has enough energy to require only minimal radiative corrections and at the same time, reduces the low energy background events. Two hodoscope arrays (H1 and H2) are used in the back region to form part of the trigger. Both H1 and H2 contain 42 scintillating paddles (for the top detector half) connected to photomultiplier tubes (PMT). The PMT's use a threshold set below minimum ionizing energy to insure maximum trigger efficiency. To discriminate between scattered positrons coming from the target and particles traveling in the opposite direction coming from the proton beam, a third hodoscope (H0) is situated in front of the magnet. The distance between H0 and the other hodoscopes allows for an average flight time ($\sim$ light speed) of 18 ns, which is long enough to suppress triggers from proton beam induced background traveling from the rear of the experiment to the front. H0 is constructed of a single scintillator paddle for each detector half. The response in each paddle is read out by two PMT's, again with a threshold set below minimum ionizing energy. The redundancy in the hodoscope scintillators reduces the amount of random triggers from background noise in the PMTs. To further reduce random triggers and background triggers from the proton beam and adjacent positron bunches, the signals from the three hodoscopes and calorimeter must arrive in a small time window defined by the progression of the positron bunch through the detector. The bunch timing is derived from a HERA clock, which is synchronized with the positron bunches in the accelerator ring.

3.6 Calorimeter

The calorimeter and the preshower counter are the only HERMES detectors which are able to efficiently detect photons. Photons, being neutral particles, traverse undisturbed through the spectrometer, except for the loss due to the radiation length of the spectrometer. Upstream of the preshower detector (a lead sheet of two radiation lengths) the HERMES spectrometer amounts to ~ 0.2 radiation lengths, with the largest contribution from the Čerenkov and TRD detectors. Any photon absorbed before the preshower counter will not detected. In addition, any photon with energy less than 0.8 GeV (minimum ionizing energy in the calorimeter) is not used in any analysis. The undetected photons would be important in a cross section measurement, but should not affect an single beam-spin asymmetry measurement. The absorption or attenuation of photons can take place by three mechanisms; photo-electric absorption, Compton scattering, and pair production (e^+e^- pair). For highly energetic photons (energy greater than ~ 0.1 GeV) the attenuation is almost always by pair production. The attenuation of photons of intensity I_0 through the conversion to an electron-positron pair is governed by the equation:

$$I = I_0 \exp(-\frac{7x}{9X_0}) , \tag{3.7}$$

where x is the distance traveled in the material and X_0 is the radiation length of the material. For the preshower lead sheet of 2 radiation lengths there is $\sim 78\%$ probability for a photon to convert into a lepton pair. The conversion into a electron-positron pair starts a cascade shower of particles as the pair will emit photons through the bremsstrahlung process, which will in turn create more pairs. The charged particles in this shower will be detected in the hodoscope paddles with an energy deposition larger than the minimum ionizing energy. Although not very efficient at photon detection, the preshower is useful for systematic checks of the photon production and increases the ability of the HERMES spectrometer to separate positrons from hadrons.

The main photon detector is the calorimeter, which has been briefly described in the particle identification section 3.3.2. Photons predominantly convert into a lepton pair in the preshower counter and start the electromagnetic shower which continues in the calorimeter. The photons which do not convert in the preshower counter will convert in the calorimeter glass blocks (18 radiation lengths) therefore virtually all photons are detected. The original design and implementation of the calorimeter was focused on the requirements of the DIS trigger and the positron-hadron separation in addition to the need for high radiation hardness to survive in a storage ring environment. These considerations resulted in less than optimal characteristics for photon detection. The radiation hardness requirement of the lead glass reduces the optical transmission causing an attenuation of the light yield at the PMT's, making position and energy reconstruction of photons more challenging. The calorimeter is calibrated by ensuring that the energy of a positron measured in the calorimeter is consistent with the momentum measured by the tracking detector and magnet ($E/p = 1$). This method of calibration may not be optimal for the photons which have a longer shower development (1 radiation length on average).

The calorimeter, luminosity monitor, and hodoscope arrays all use photomultiplier tubes having an amplification gain which may drift with time. To monitor the relative gains between tubes a gain monitoring system (GMS) was installed. The GMS consists of a dye laser light source of varying intensity channeled through glass fibers to each PTM of the H2 hodoscope array, calorimeter and luminosity monitor and to a reference diode. The intensity of the laser light is continuously varied with the use of a rotating filter wheel at the laser source. The output of each PMT is compared to the signal from the reference diode which has been shown to have a stable gain over long periods of time. The gain changes for each PMT relative to the reference diode are monitored to identify time dependent gain shifts and non-functioning PMTs. In this way the optimum performance of the detectors using PMT tubes can be maintained.

Chapter 4

Analysis

The experimental data from the spectrometer proceed through several processing and reduction steps before the desired events are obtained. When an event is detected by the spectrometer, all the detector responses are collected and the information stored on a computer hard disk in files. These raw data files are decoded and the main tracking program reconstructs the individual events and stores the relevant information in files ready for individual analyses. An analysis code is used to extract out the relevant information for each event of interest. A measurement is formed from the data sample. The quality of the measurement is ascertained by the statistical accuracy (number of events collected) and systematic uncertainty due to the measurement technique.

4.1 Data Acquisition and Production

The data are collected using a data acquisition system (DAQ). The responses from individual detectors are translated into digital form in the DAQ; analog signals from the numerous photomultiplier tubes (PMT) to digital form using analog-to-digital converters (ADC) and timing information from the tracking detectors using time-to-digital converters (TDC). When an event causes a desired response in the detector (triggered event), all the digital information relevant for the event is collected by an electronic event builder and sent via an optical link to a DEC/ALPHA computer cluster located in the HERMES control room. The event information is then stored on computer disk until it is transfered to a more permanent location. The building of the event and transfer of the information to the computers takes about 600 μs, during which no other trigger can be accepted (dead time).

The event data are stored along with general spectrometer information which changes on a longer time scale, such as the target and detector status information. This general 'slow' information is read out every 10 seconds (a burst). In addition, the target information is read out every time the polarization is flipped (every 1-2 minutes randomly) when the polarized target is used. The number of triggers, events, and luminosity counts (scalars) integrated over the time span of the burst are also stored with the event data.

The event information along with the slow information and scalars are collected into run files written in EPIO (Experimental Physics Input Output) [66] format and consist of $\sim$ 50k events or about 10 min. of normal data acquisition. These raw data files are written to tape locally and also sent to the main HERMES computer and the DESY tape robot. In addition, the slow control information is written to local files using a Distributed ADAMO Database (DAD) [67] format. DAD is a database version of the ADAMO (Aleph Data Model) [68] entity-relationship type database. These local slow control files allow calibration of the individual detectors.

4.1.1 HDC

The raw data are taken from the DESY tape robot and processed through several programs for conversion into useful physics quantities. An overview of this process is shown in Fig. 4.1. The first process is to decode the raw EPIO event data and convert the pulse height information of the PMT's and the timing information of the tracking chambers into energies and positions, using the HERMES geometry and specific mapping and calibration information. This task is completed with the HERMES DeCoder (HDC). The scalar information is also decoded in this process and stored in separate files to be used in the slow control information processing. The decoded event information from the HDC program is sent directly into the next program, the HERMES ReConstruction program (HRC).

4.1.2 HRC

The HERMES ReConstruction (HRC) program is the main program used to reconstruct the charged particle tracks in the spectrometer and to calculate physics quantities. HRC uses the output of HDC in conjunction with alignment and calibration information to identify and reconstruct tracks.

The reconstruction of tracks in HRC consists of several steps. First, the information from the tracking detectors in each projection (X, U, or V directions) is combined together into two bit patterns, one for partial tracks in front of the magnet and one for partial tracks in the back section of the spectrometer. Tracks in each projection are reconstructed by combining detector bit patterns and then comparing the combination to a pattern data bank. This pattern data bank consists of a set of track patterns, generated at the initial program setup and representing all possible allowed track (bit) patterns in the HERMES spectrometer. There are 126 million possible track patterns reduced by symmetry arguments to 31,000 unique entries. The pattern comparison is an iterative

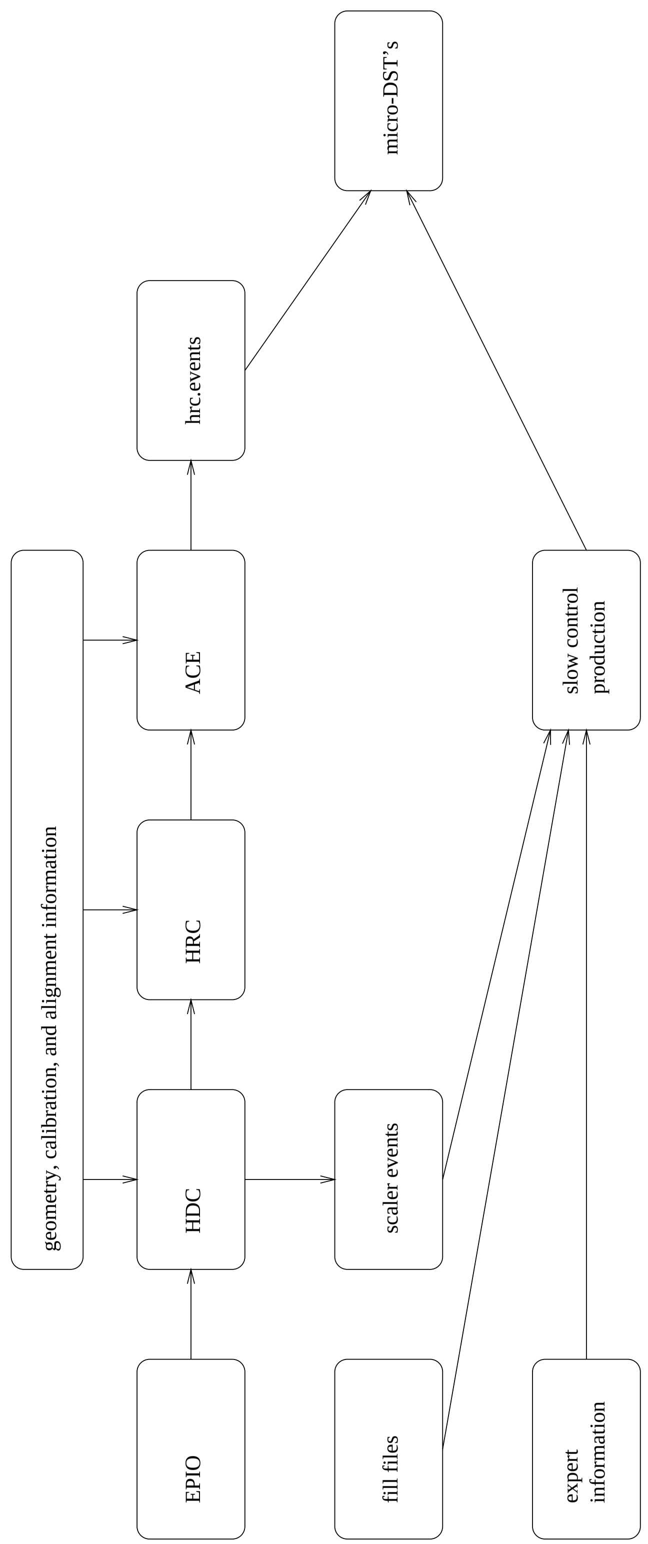

Figure 4.1: The HERMES production layout showing the various steps in the reconstruction of the raw data.

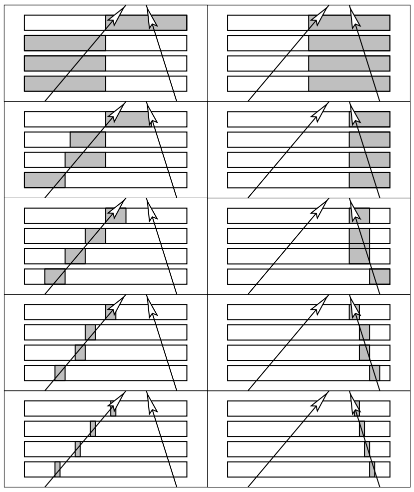

Figure 4.2: Track pattern search for two tracks. The detector pattern is compared to the pattern data bank at each iteration starting from the top of the plot.

procedure, the first iteration compares the combined detector responses to several simple patterns. Each simple pattern (parent) has several more complicated child patterns. If the detector bit pattern matches the simple parent, it is then compared to the related child patterns. The child pattern is either matched, in which case the bit pattern enters another iteration with the (grand)child patterns of the matched child, or the bit pattern fails to find a match, in which case no partial track can be formed. The iteration pattern matching procedure is repeated until the maximum variance in the proposed partial track is $\sim$ 4 times the detector resolution. The detector resolution for the drift chambers is on the order of $\sim 250\mu$m corresponding to $\sim$ 1 mm width of the final matched pattern. This technique of pattern matching reduces the number of matching tests as compared to a linear approach of matching all possibilities, resulting in a faster event reconstruction. There are at most eleven iterations and each proposed track is compared to an average of 70 bit patterns. A diagram of the matching pattern process is shown in Fig. 4.2 and more detail can be found in Ref. [69]. The efficiency of the detectors is not perfect, therefore allowances are made to also accept tracks with one (or more) missing detector response(s). The pattern matching algorithm is used only to identify a track; the actual track parameters are calculated using a fit to the detector responses.

The 2-dimensional partial tracks in each of the X, U, or V projections for the front and back region are combined to form a 3-dimensional front or back partial track. A linear fit to the detector responses yields the final partial track parameters. The front and back tracks are then combined into a full track, by matching the straight line projections of each track in the center of the magnet. In 1995 and 1996, before the commissioning of the vertex and drift vertex chambers was completed and the chambers used in the track reconstruction, the direction of the partial front track was relatively poorly defined due to the close proximity of the front chambers to each other. Therefore, the projected back partial track at the center of the magnet was used as another point to define the front partial track. This process, known as forced bridging, increased the resolution of the front partial track parameters.

The full track parameters are used along with a measured map of the magnetic field to determine the momentum of the particle. Instead of tracking the particle through the magnetic field for every track, a momentum look-up table is used. This look-up table, produced initially along with the track pattern data bank, contains the momentum of a half of million particles, tracked through the magnetic field and parameterized by the interaction vertex at the target (z-vertex), two angles in the x and y direction (θ_x, θ_y), and the angle difference between the front and back partial tracks, resulting in a five-dimensional matrix. The track parameters (for the full track) define a 4-dimensional point, which will be enclosed by $2^5 = 32$ points in the matrix. The 32 points are interpolated to yield the best momentum calculation of the particle.

Very low momentum front partial tracks will have no matching back partial track since they are bent out of the acceptance of the back portion of the spectrometer. These front 'short' tracks use the magnet chamber information for a momentum determination. Unfortunately, these short tracks do not traverse the particle identification detectors and therefore have limited use in analyses.

Another function of HRC is to combine the responses of the calorimeter blocks into clusters. The blocks in the calorimeter are scanned in the x and y direction to locate local energy maxima. Two peak blocks adjacent to each other can be separated into two clusters, as local maxima in both the x and y directions are used for potential clusters. However, since the block face size is 9×9 cm^2, two clusters can only be distinguished if the energy peaks are detected in separate blocks. Two photons will therefore be reconstructed as a single cluster if the two photons are incident on a single block. Two photons will be reconstructed predominantly as two clusters if the distance between the photons is greater than ~ 10 cm.

As a shower width can exceed the size of one block, the energy of this peak block is combined with the energy from the surrounding eight blocks (or five, if the peak block is on the calorimeter edge) to form the cluster energy (see Fig. 4.3). In the case where there are two peak blocks close to each other (overlapping clusters) a weighting scheme is used to determine the energy associated with each cluster. Once an individual cluster is selected, the total energy of the cluster is re-calibrated, using an energy calibration curve obtained from the calorimeter test beam data [70]. The central position of

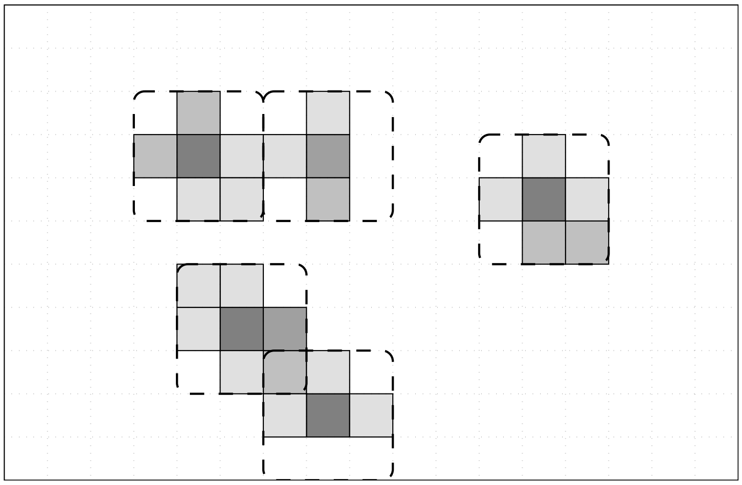

Figure 4.3: Schematic of the calorimeter cluster search in the HRC program.

the cluster is then calculated using a simple square root weighting:

$$x_{cl} = \frac{\sum_i \sqrt{E_i} x_i}{\sum_i \sqrt{E_i}}, \tag{4.1}$$

where x_i and E_i represent the central position and energy of the i^{th} block. The x and y positions for the cluster are calculated independently.

Clusters in the calorimeter are associated with a track if the cluster center is located within ≈ 4.5 cm to the track position. The track association search also uses the projected position of the front track, to include possible bremsstrahlung from the front region. Including bremsstrahlung clusters means that there could be more than one cluster associated with a track. The energies of the clusters associated with a track are combined to yield a charged particle energy measurement from the calorimeter. Calorimeter energies from positron tracks are used to calibrate the calorimeter on a run to run basis by ensuring the distribution of the energy to momentum ratio (E_{calo}/p) is peaked at a value of one.

4.1.3 ACE

The HRC reconstructed data are then piped into the detector efficiency calculation program ACE (Alignment, Calibration, and Efficiency). Originally designed to handle the alignment and calibration, ACE is only used to calculate detector efficiencies at present, while the alignment and calibration is handled in separate routines maintained by the person(s) responsible for the individual detector(s). ACE uses the tracks found by HRC to measure the efficiency of each tracking detector without introducing any bias. Typical efficiencies for the tracking chambers range from 95% to 98%.

To calculate the efficiency of all detectors combined, an algorithm is used which takes into account the individual detector efficiencies, the resolution of the detectors, and the momentum of the track.

4.1.4 Slow control and μDST production

A production of the slow information is carried out in parallel to the event reconstruction of HRC. The slow information production consists of the calculation and calibration of parameters which change on a burst level ($\sim$ 10 sec). These parameter are constant for all events within the burst, for example, the beam polarization, and therefore do not need to be updated for each event. The slow information production requires input from person(s) responsible for individual detector(s) and combines the slow and scalar information into a single file for each run. The slow information is then synchronized with the output from the HRC reconstruction chain and stored in a single micro-dataset tape (μDST) as was shown before in Fig. 4.1. The particle identification is also calculated at this step in the production chain, using the most recent parent distributions. A data quality parameter for each event is constructed using all available information from the detectors and experts. Only analysis relevant information is stored the μDST file, in order to minimize the file size for each run.

The reconstruction chain is iterated at least one time, as many of the alignment and calibration parameters are calculated from actual data. This leads to several productions of a given data set using the main(HDC/HRC/ACE), slow, and μDST programs.

4.2 Single Photon Event Selection

The deeply virtual Compton scattering process is the scattering of a lepton from a target which does not fragment, producing a real photon in the final state. The HERMES detector is not presently able to detect recoil particles which have relatively low energy and large polar angles, therefore only the scattered lepton and real photon are detected. The data collected in 1996 and 1997 from a hydrogen target are used in this present analysis. Events were selected as single photon candidates if there was exactly one reconstructed positively charged track along with exactly one untracked cluster. The charged track had to be detected in the full detector for particle identification purposes, so no short tracks were used as these particles are swept out of the (back) detector acceptance by the magnet. The charged track also had to be identified as a positron using the four particle identification detectors. The untracked cluster was identified by a deposition of energy in the calorimeter greater than 0.8 GeV without an associated track in the detector. Due to the granularity of the calorimeter and the cluster algorithm in HRC, two untracked clusters which have centroids separated by less than $\approx$ 10 cm are identified as a single untracked cluster and are included in the single photon candidate selection.

However, if two untracked cluster centroids are separated by more than $\approx$ 10 cm, the distinction of the two is possible and the event rejected from the single photon candidates. The estimate of the events with two overlapping clusters will be discussed in Sec. 4.7.2.2.

Neutral particles, such as the π^0 meson, can decay into two photons. Events containing two photons from a neutral particle decay will most likely be reconstructed with two untracked clusters. The requirement of exactly one untracked cluster for the single photon analysis removes a large fraction of the events containing a neutral particle decay. However, due to the finite acceptance of the HERMES spectrometer, there is a possibility that only one of the photons from neutral particle decay will be detected, causing a background contamination to the analysis. In addition, due to the granularity of the calorimeter, two decay photons could be reconstructed as a single photon. This possible background from neutral particle decay will be discussed in more detail in Sec. 4.7.2.2.

The detection of the scattered positron allows for a calculation of the exchanged virtual photon's four momentum vector $(\nu, \vec{q})$. The event kinematic variables are also calculated in the lab frame as in DIS:

$$
\begin{aligned}
Q^2 &= -q^2 = 4EE' \sin^2(\theta/2)\,, \\
x_{Bj} &= \frac{Q^2}{2M\nu}\,, \\
W^2 &= (p+q)^2 = M^2 + 2M\nu - Q^2\,, \\
y &= \frac{q \cdot p}{k \cdot p} = \frac{\nu}{E}\,, \\
t &= (q - cl)^2 = -Q^2 - 2(\nu E_{cl} - \vec{q} \cdot \vec{cl})\,,
\end{aligned} \tag{4.2}
$$

where E (E') is the initial (scattered) positron energy, θ is the scattered polar angle of the positron, M is the proton mass (positron mass neglected), and cl $(E_{cl}, \vec{cl})$ is the four-momentum vector of the cluster (produced photon). The variables p and q represent the four-momentum vectors of the initial proton and virtual photon respectively. The kinematics of the photon are calculated using the reconstructed untracked cluster position and energy and assuming the photon originated from the same vertex as the positron. With the virtual and real photon four-momenta, the opening angle $\theta_{\gamma*\gamma}$ and the azimuthal angle ϕ can be calculated in the lab frame as:

$$
\theta_{\gamma*\gamma} = cos^{-1}\left(\frac{\vec{q} \cdot \vec{cl}}{|\vec{q} \cdot \vec{cl}|}\right)\,, \tag{4.3}
$$

$$
\phi = \frac{\vec{cl} \cdot \vec{q} \times \vec{k}}{|\vec{cl} \cdot \vec{q} \times \vec{k}|} \cos^{-1}\left(\frac{(\vec{q} \times \vec{k}) \cdot (\vec{q} \times \vec{cl})}{|\vec{q} \times \vec{k}||\vec{q} \times \vec{cl}|}\right)\,. \tag{4.4}
$$

The azimuthal angle is constrained between $-\pi$ and π with the sign given by the first part of the right hand side Eq. 4.4. A illustration of the azimuthal angle of the produced photon around the virtual photon axis was shown earlier in Fig. 2.16. The recoil proton is not detected in this analysis, however, the missing mass of the process can be calculated from the event kinematics. In principle, the exclusive events should have a missing mass of the proton (0.938 GeV) but due to the finite resolution of the detector the experimental missing mass is broadened about the proton mass. The missing mass is calculated as:

$$\begin{aligned} M_x^2 &= (q + p - cl)^2 = M^2 + 2M(\nu - E_{cl}) - Q^2 - 2(\nu E_{cl} - \vec{q} \cdot \vec{cl}) \, , \\ M_x &= \sqrt{M_x^2} \, . \end{aligned} \tag{4.5}$$

A negative M_x^2 may arise due to the finite momentum resolution of the spectrometer in which case $M_x = -\sqrt{-M_x^2}$.

4.2.1 Data Quality

In order to minimize the systematic uncertainties in a given measurement, the quality of the data needs to be ascertained. The data quality is parameterized in the μDST production, where all available information is combined into one data quality (DQ) hexadecimal number for each half of the spectrometer (top and bottom). The following is a list of the DQ constraints used for the single photon analysis.

- Run level DQ:

  - run stated analyzable by the shift crew

  - run used a hydrogen target

  - no high voltage trips in the tracking detectors

  - calorimeter working properly

  - hodoscope arrays (H0, H1, and H2) and luminosity monitor working properly

  - TRD working properly

- Burst level DQ:

  - beam polarization is within the range of 0.4 to 0.8

  - dead-time of the DAQ is less than 20% (live time > 80%)

  - length of burst is in the range of 8 - 11 seconds

  - beam current is in the range of 5.0 to 50.0 mA

  - first/last burst of run eliminated to reduce synchronization problems

For the data collected with the polarized target, the data were summed over the target polarization and combined with unpolarized target data. Therefore, no consideration was given to the quality of the target polarization.

4.2.2 Kinematic Constraints

The selected events with good data quality were further constrained by several kinematic considerations. Higher twist corrections scale with the inverse momentum transfer $1/Q^2$. The momentum transfer should therefore, be much greater than one ($Q^2 >> 1$) to ensure the interaction is in the region where hard scattering is taking place and factorization is valid. However, the cross section scales as $1/Q^4(1/Q^6)$ for the BH (DVCS) process so statistics are limited at high Q values. For the measurement to have some statistical precision, the data were constrained to have a momentum transfer of $Q^2 > 1$ GeV^2. In DIS, the structure functions were measured at HERMES kinematics scale using $Q^2 > 1$ GeV^2 and exhibit scaling behavior, it is assumed that a similar behavior exists for the single photon production.

The threshold on the calorimeter sums is 3.5 GeV for the unpolarized target data to reduce the background events and trigger rate of the higher density target, however, the threshold is 1.5 GeV for the polarized data. In order to combine the two data samples, a constraint was placed on the difference in the incoming and scattered positron energies ($\nu = E_{Beam} - E'$) to be less than 24 GeV. This ensures that all triggers originated from a positron with an energy greater than 3.57 GeV, which allows combining of the polarized and unpolarized target data.

4.2.3 Fiducial Constraints

Both the positron and untracked cluster were constrained to be within the nominal acceptance of the spectrometer (± 40 to 140 mrad in y, ± 0 to 170 mrad in x) to remove events reconstructed outside the spectrometer acceptance. The positron vertex, defined as the position along the beam line of the distance of closest approach of the positron track, was constrained to be within the target area. Although the target extends to ± 20 cm, the events were constrained at ± 18 cm, due to the resolution in the reconstructed interaction vertex which is ~ 1 cm. In addition, the transverse target positions, defined as the transverse distance from the beam to the track at the vertex, was constrained to be less than 0.75 cm. The central position of the untracked clusters was constrained to be above (below) the first row of calorimeter blocks at ± 33 cm for the top (bottom) detector halves so that the clusters near the beam pipe contained the full energy sum of nine blocks for an accurate accounting of the energy deposition.

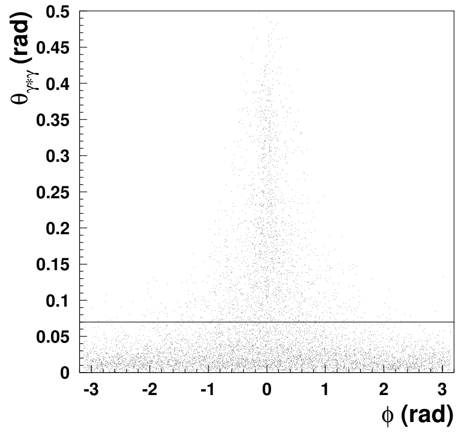

Figure 4.4: A scatter plot of the azimuthal angle (ϕ) versus the opening angle ($\theta_{\gamma * \gamma}$) for events in the exclusive region ($-1.5 < M_x < 1.7$ GeV) from the 96 and 97 datasets. The solid horizontal line demarcates the position of the maximum opening constraint at 0.07 radians.

The opening angle ($\theta_{\gamma * \gamma}$) between the virtual and real produced photon was constrained with both a lower and upper limit. A lower limit needs to be placed as the azimuthal angle ϕ becomes undefined when $\theta_{\gamma * \gamma} = 0$. A lower limit of 0.015 rad was placed on the opening angle, due to considerations of the position resolution of the real photon cluster which will be discussed in further detail in Sec. 4.6.5. The maximum opening angle was constrained since the acceptance in the azimuthal angle decreases with increasing $\theta_{\gamma * \gamma}$. Therefore, the opening angle was constrained to be less than 0.07 rad to ensure a more uniform acceptance with respect to the azimuthal angle (see Fig. 4.4).

4.2.4 Exclusivity Constraint

As the recoil proton is not detected, the missing mass is reconstructed and used to define a region containing predominantly exclusive events. Due to the finite resolution of the detector, exclusive events can not be unambiguously separated from non-exclusive events, however a primarily exclusive sample can be obtained by constraining the missing mass. Initially, the resolution of the detector was roughly estimated to be ≈ 0.5 GeV, and an exclusive region defined between 0.4 and 1.4 GeV. As the single photon analysis matured, it was realized that the definition of the exclusive region should be modified. Since the true value of the missing mass can be only 0.938 GeV or larger, the events with a reconstructed missing mass less than the proton mass (due to the limited detector resolution) should be enriched with exclusive events. Therefore, a lower constraint was placed on the missing mass of -1.5 GeV, which included nearly all low missing mass events. The upper constraint was placed at $+1.7$ GeV, which was determined from an MC simulation (described in the following section) to provide as many exclusive events while minimizing the non-exclusive background. For this analysis, events with a reconstructed missing mass in the region of -1.5 to $+1.7$ GeV were used to form the asymmetry measurement.

4.3 Monte Carlo Simulation

In order to better understand the experimental data obtained from the HERMES detector, a Monte Carlo simulation of the detector was implemented (HERMES Monte Carlo or HMC) [71]. The HMC program is useful to model detector responses, calculate the efficiency and acceptance of the spectrometer, and allow a comparison of physics models with the experimental data.

The HMC program consists of several distinct stages. The first stage is simulated event generation. An event generator will randomly select event kinematics for the process of interest, weighted by the appropriate cross section. For the single photon analysis, two generators were used. The first generator is the standard event generator used by HERMES to describe the deeply inelastic scattering process. This generator is an extension of the leptoproduction generator LEPTO [72] which simulates the polarized DIS process and is called PEPSI [73]. The generator uses the best known (un)polarized parton distribution functions in a simulation of the parton level interactions based on the leading order electro-weak cross sections of the standard model. The fragmentation and decay of unstable particles was simulated with JETSET [74] based on the LUND string model [75]. Radiative processes were included with RADGEN [76], a simulation of the QED lowest-order radiative effects for polarized and unpolarized DIS processes, which provide simulation of the BH process. The combination of the PEPSI, JETSET, and RADGEN programs results in a consistent simulation of the DIS process, including the BH process for exclusive events. However, this generator does not include the DVCS or other exclusive processes and therefore is primarily used to model the single photon data in the non-exclusive region.

For the exclusive region of the single photon analysis, an exclusive generator is used. The exclusive generator randomly selected events evenly distributed in the kinematic variables Q^2, ν, and t across the HERMES acceptance range. The remaining event kinematics for the exclusive single photon production are calculated to produce a positron, photon, and proton in the final state. The generated event is weighted using the parameterization model [31] discussed in Sec. 2.3.1, which includes both the DVCS and BH amplitudes. The BH process is calculated in conjunction with the DVCS process in order to include interference effects, hence the radiative modeling of RADGEN is not used in the exclusive generator. This generator does not include any non-exclusive processes, and therefore can only model the single photon data in the exclusive region.

The second stage of the HMC program consists of tracking the generated event through a computer model of the HERMES detector using the GEANT (Generation of Events ANd Tracks) detector simulation package [77]. The simulated responses of the detectors were converted into a digitized form to resemble actual experimental data. The measured experimental resolutions and efficiency functions of the individual detectors were used in the digitization of the signals for a realistic particle detection simulation.

The digitized simulated events were then used as input to the HERMES analysis chain, and produced simulated results in the same format as that from the experimental data. This allowed a direct comparison of the experimental and MC simulated analysis results. The MC simulation of the single photon process consisted of analyzing existing MC simulated DIS data. In addition, an exclusive MC simulation was produced and the resulting exclusive MC data analyzed.

The MC data were normalized to the total number of experimental single photon events. An absolute normalization of the MC and experimental data could be performed, which requires accounting for detector efficiencies and absolute luminosity measurements for the experimental data. However, the absolute normalization is not needed for an asymmetry measurement and was not carried out. A normalization to number of reconstructed DIS events in the MC simulation and the experimental data was completed, however, the ratio of single photon to DIS events is smaller ($\approx 30\%$) for the experimental data than for the MC simulation. The cause of this discrepancy between the ratios has not been discovered, although an efficiency or resolution problem in the cluster detection would cause a reduction in the number of single photon events as compared to DIS events.

For this analysis, the MC simulation of the DIS process is only used to estimate the missing mass resolution, and to make a qualitative estimate of the magnitude of the BH process in the exclusive region. Therefore, an absolute or DIS normalization should not be needed, and the MC simulation was normalized to the total number of single photon events in the experimental data. The MC simulation of the DIS process analyzed for single photons provides a fair description of the single photon data for the different kinematic distributions, even though no exclusive processes are included in the simulation (see Fig. 4.5). In particular, the behavior of the squared missing mass distribution is described by the MC simulation of the DIS process, and illustrates the dominant BH process in the exclusive region (see Fig. 4.6). The BH dominance indicates that the non-exclusive contribution or contamination is minimal in the exclusive region, and that the DVCS cross section is small compared to the BH cross section, as expected. Since the DVCS process is not included in the MC simulation of the DIS process, a separate exclusive simulation was completed.

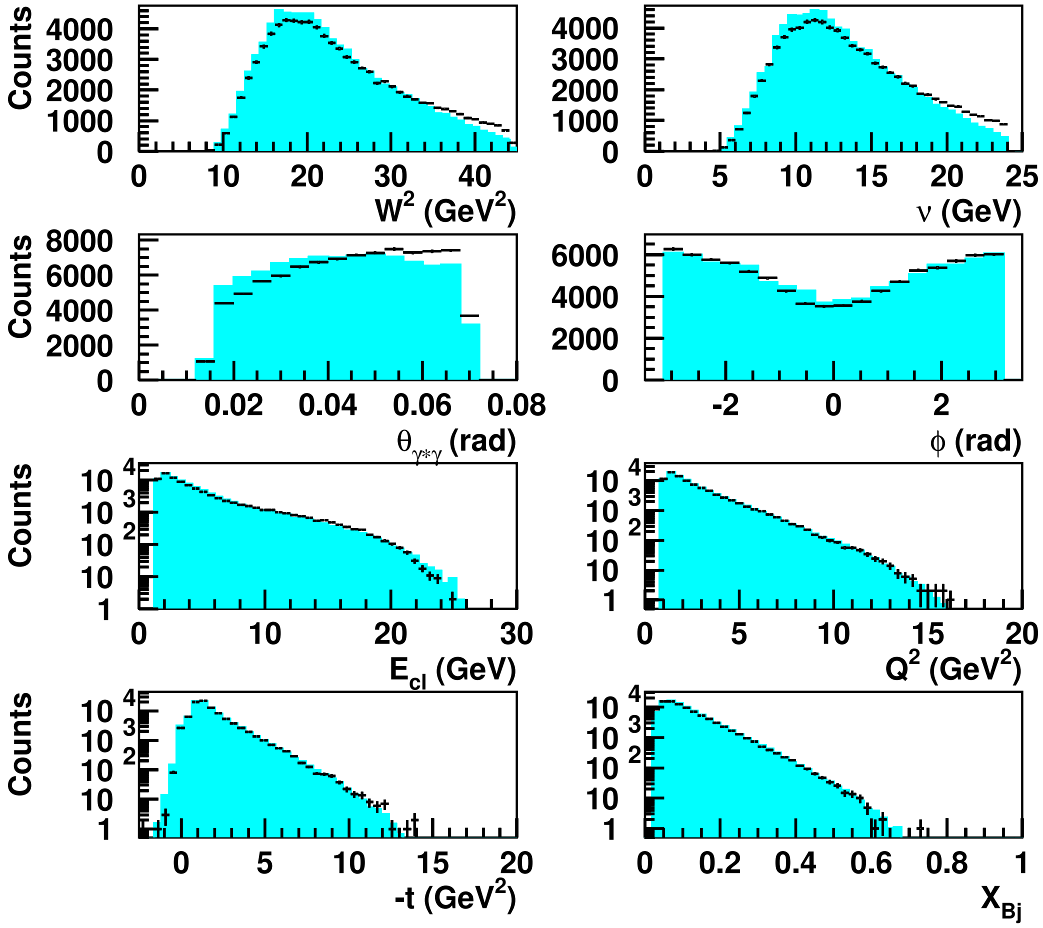

Figure 4.5: Comparison of the single photon data (points) to the DIS MC simulation (shaded area) for several kinematic variables. The MC simulation has been normalized to the total number of experimental single photons.

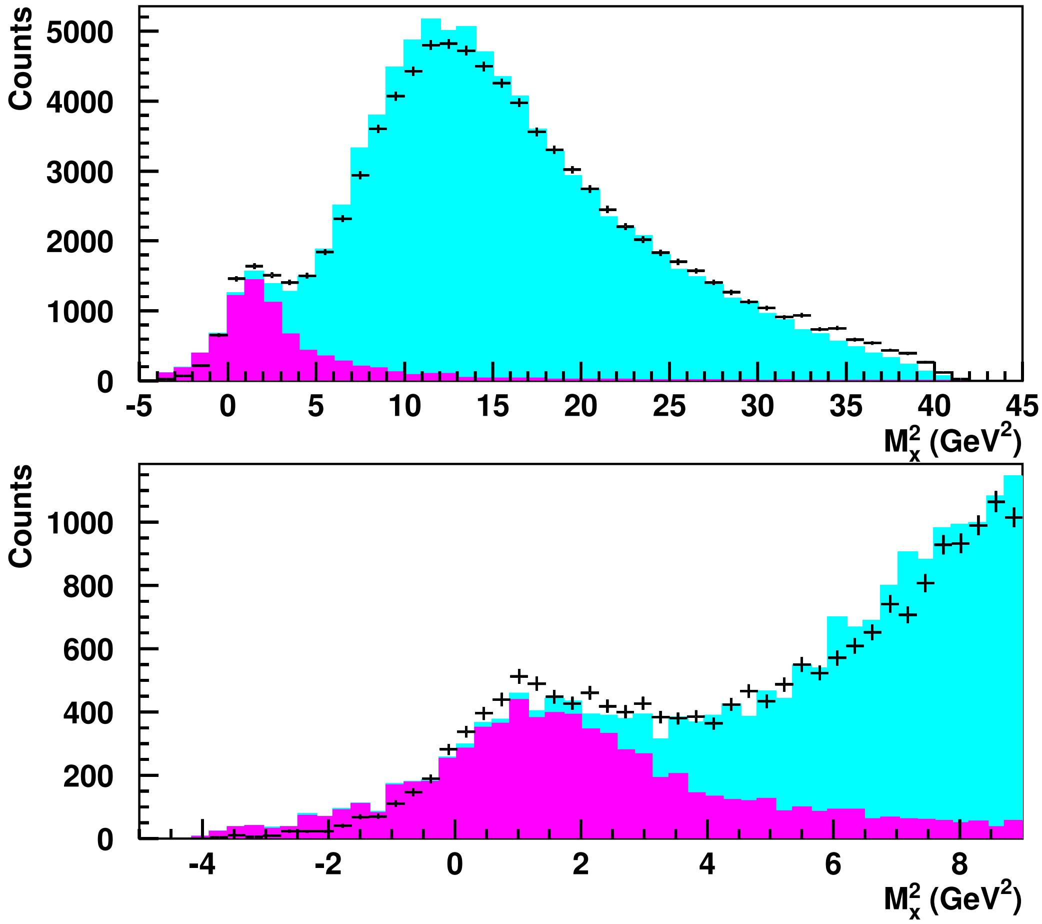

Figure 4.6: Comparison of the single photon data (points) to the MC simulation (shaded area) for the squared missing mass (M_x^2) distributions. The full kinematic range is displayed in the upper panel, while the low M_x^2 domain is shown in the lower panel. The light gray histogram represents the MC simulation of the DIS process including the BH process, while the dark-shaded histogram represent the BH contribution only. The full MC simulation has been normalized to the total number of experimental single photons, with the same normalization value used for the BH contribution.

The exclusive generator produced a random generation of events evenly distributed in the kinematic variables Q^2, ν, and t. The distribution at low Q^2 is therefore under-represented by the MC simulation, due to the $1/Q^4$ ($1/Q^6$) dependence of the BH (DVCS) cross section, and results in a less than optimal description of the experimental data. Also, the available exclusive MC dataset is limited as the calculation of the cross section from the parameterization model is time-consuming. However, the characterization of the exclusive region with a BH-DVCS model calculation in a MC simulation does describe the basic trends of the kinematic distributions (see Fig. 4.7).

4.4 Preliminary Consistency Checks

To ensure that the detected particles from the selected events are being produced from the interaction of the lepton beam and the target, and not from some background process, a number of checks were carried out on the final state particles.

4.4.1 Scattered Positron Checks

The charged track momentum resolution for the HERMES spectrometer has been shown to be $\sigma(P)/P < 1.5\%$ over all accessible momenta [62]. For the single photon analysis, the average positron momentum in the exclusive region is ~ 16 GeV which equates to an energy resolution for the positron (and hence for the virtual photon energy) of < 240 MeV. The angular resolution of a charged track is $\Delta\theta < 0.6$ mrad over the angular acceptance of the experiment.

The positron vertex is determined as the distance of closest approach of the positron track to the beam and hence may not reflect the true interaction vertex. Several checks were made to ensure the positron was being scattered by the target gas. The first check consisted of projecting the track parameters backwards to the location of the collimator directly in front of the target. The projected tracks from events in the exclusive region show a random behavior, consistent with a target interaction rather than a collision with the collimator (see Fig. 4.8). Another check is of the positron vertex distribution along the beam axis (z-axis). The distribution in both the exclusive and non-exclusive regions has a triangular shape (see Fig. 4.9) which is consistent with the density of the target gas along the target cell. The vertex distribution suggests the positrons in the beam are interacting with the target gas instead of scraping the cell walls or collimator edges.

The positron is identified as a lepton using the four particle identification chambers and the charge defined by the direction of the bend in the magnetic field. To minimize the contamination from hadrons, the log-likelihood PID (see Sec. 3.3.2) values were selected to be greater than a value of 2, which corresponds to a probability that the particle was 100 times more likely a lepton than a

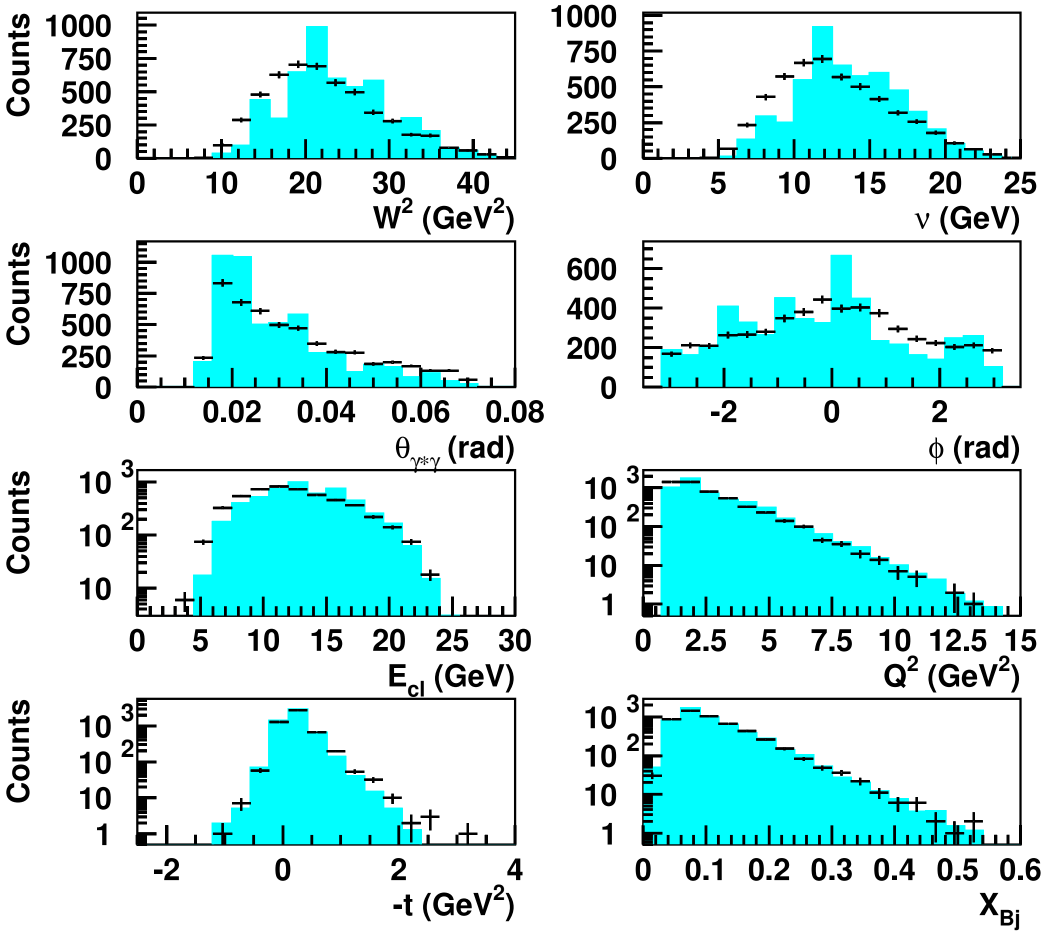

Figure 4.7: Comparison of the exclusive ($-1.5 < M_x < 1.7$ GeV) single photon data (points) to the exclusive MC simulation (shaded area) for several kinematic variables. The MC simulation has been normalized to the number of experimental single photons in the exclusive region.

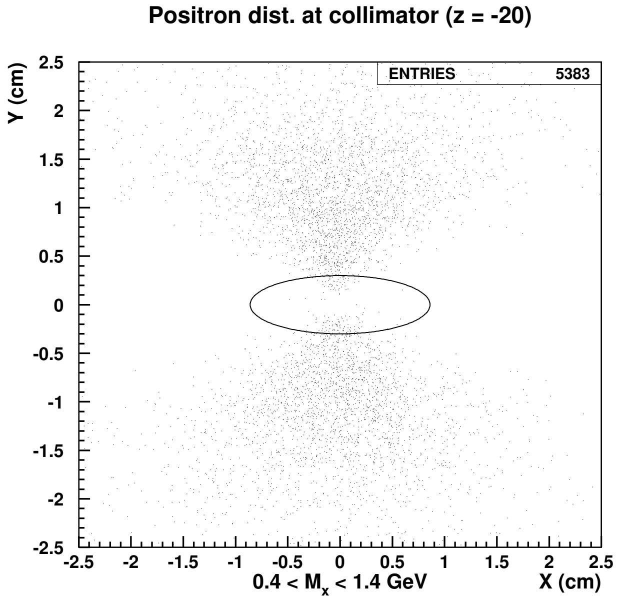

Figure 4.8: A scatter plot of the (x,y) position of the projected positron track at the C2 collimator ($z = -20$ cm). The distribution of single photon events in the exclusive missing mass region ($0.4 < M_x < 1.4$ GeV) is displayed along with the outline of the collimator opening (solid line).

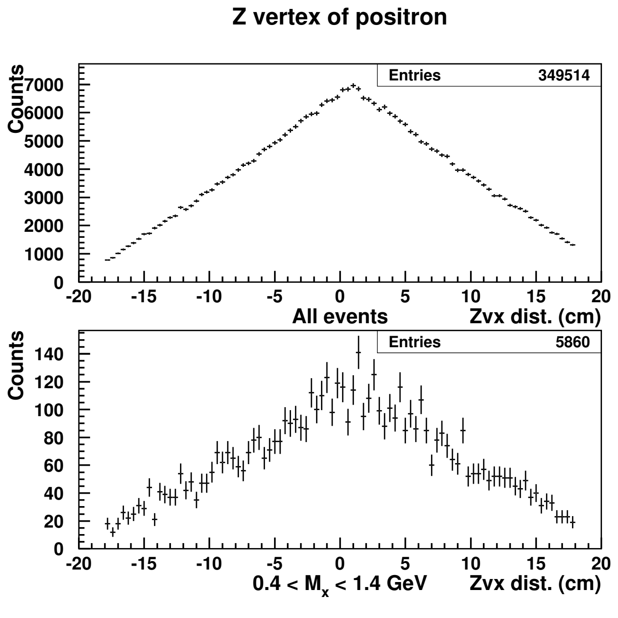

Figure 4.9: The z-vertex distribution of the positrons for all single photon events (top panel) and for the single photon events in the missing mass bin from 0.4 to 1.4 GeV (bottom panel).

hadron. To check that the hadron contamination was indeed small, a similar analysis was carried out for the charge conjugate reaction products (ie. e^-, p, and γ). These products should arise in only two cases, the first from lepton pair production, which is suppressed compared to the BH or DVCS process due to the extra vertex, and secondly from the misidentification of a hadron as an *electron*. This latter process would give an estimate of the hadron contamination to the positrons of the single photon analysis. As shown in Fig. 4.10, the events with an electron in the final state as opposed to a positron are suppressed by two orders of magnitude in the exclusive region ($M_x < 2$ GeV) indicating that the hadron contamination is less than 1% of the positrons in the exclusive events.

4.4.2 Photon Checks

The untracked cluster was studied in the exclusive region to ensure that the cluster originated from a photon. The average energy of the photon in the exclusive region is ~ 12 GeV with a minimum of ~ 5 GeV (see Fig. 4.11). The high average energy value reduces the possibility of the cluster originating from background noise in the calorimeter. Also, the efficiency of the track finding algorithm of the HRC program minimizes the possibility of untracked clusters arising from undetected charged particles. Finally, the energy of the charged track and untracked cluster for events of interest are constrained to yield a missing mass in the exclusive region. The combination of the above considerations results in a negligible probability that the untracked cluster in the exclusive region originated from a charged particle.

The possibility that an exclusive untracked cluster originated from a *backwards* moving particle was also studied. The proton beam moves in the opposite direction from the positron beam with the proton bunches traversing the spectrometer outside the DIS trigger window. However, it is possible that stray protons outside the bunch structure could produce a signal (and trigger) in the calorimeter without a detected track in the detectors. A check of the response rate in the hodoscope array H1 was made for the single photon events. Assuming the untracked cluster originated from a photon traveling in the same direction as the positron beam, the H1 hodoscope array should produce a limited response. If on the other hand, the untracked cluster originated from a backward moving charged particle, there should be a significant response in the H1 hodoscope array. The response rate using all the hodoscope paddles in one detector half containing the untracked cluster was measured. Events where the detector half contained both the positron and untracked cluster were excluded from this test to prohibit a positron response in the H2 hodoscope array. The number of paddles with a signal in the same half of the detector as the untracked cluster for the 1996 data sample are shown in Fig. 4.12. The majority of the events do not produce any response (number = 0) in the hodoscope

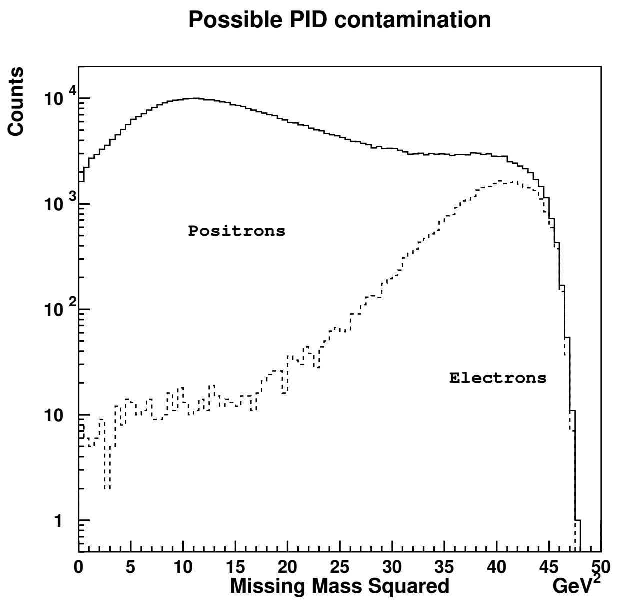

Figure 4.10: The missing mass distribution for single photon events reconstructed from $e^+\gamma$ events (solid line) and $e^-\gamma$ events (dashed line) from the 96 and 97 datasets.

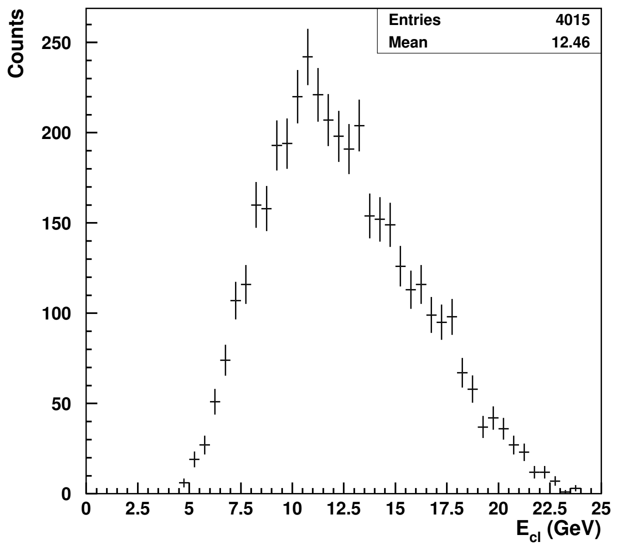

Figure 4.11: The reconstructed energy distribution for the untracked clusters in the exclusive missing mass region of $-1.5 < M_x < 1.7$ GeV.

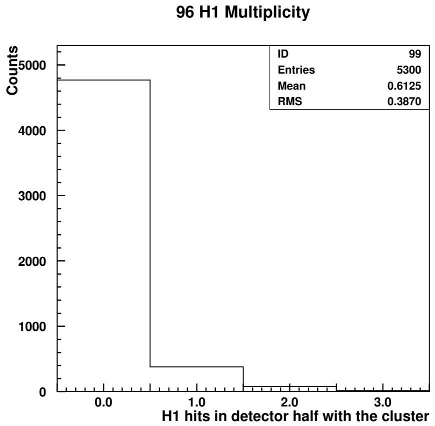

Figure 4.12: The number of H1 hodoscope paddles with a non-zero response for the detector half containing only the untracked cluster from the 1996 data sample.

paddles indicating that the cluster is arising from a neutral particle. There are a number of events which produce a response, however, these may be a result of noise, which has not been taken into account. As a further check, the multiplicity of calorimeter blocks with a response above a background threshold was investigated. If the cluster was being produced from a charged particle from the proton beam there should be many low energy accompanying particles. The calorimeter multiplicity for the 1997 data sample with the untracked cluster in the top detector (positron constrained to the bottom detector) is shown in Fig. 4.13 for a threshold of 0.035 GeV in both the exclusive and non-exclusive regions. The average multiplicity in the exclusive region is consistent with the expectation of the single cluster being contained in the central and eight surrounding blocks and inconsistent with a large number of low energy particles. There is a large tail in the calorimeter block multiplicity which arises from events where a large number of calorimeter blocks had a non-zero response, but did not form more than one cluster with energy greater than 0.8 GeV. This is attributed to the inherent noise of the PMT tubes, however, there is a possibility that another low-energy photon was produced in these events. This type of contamination has been estimated and will be presented in Sec. 4.7.2.2.

The above checks suggest that the exclusive untracked clusters originate from neutral particles and not from charged tracks. The HERMES reconstruction program is designed to associate the majority of clusters arising from external bremsstrahlung in the detector with the originating charged particle. Also, the neutral particle can not be produced from an adjoining positron bunch as the positron bunches are separated by a time span much greater than the calorimeter response time. Hence, the majority of the neutral particles should be produced from the event vertex given by the scattered positron kinematics. In the exclusive region, the missing mass constraint excludes the neutral

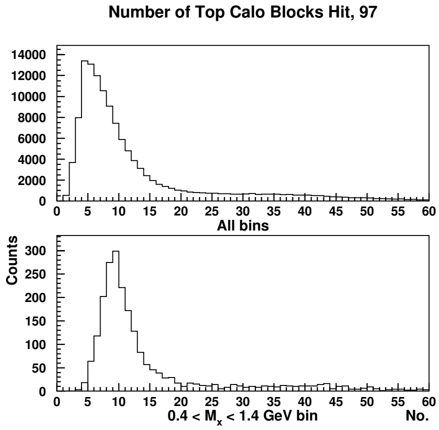

Figure 4.13: The distribution of calorimeter hits for all single photon events (top panel) and for events in the exclusive region ($0.4 < M_x < 1.4$ GeV) (bottom panel) for the 97 dataset for the sample of events in which the photon was observed in the top detector and the positron was observed in the bottom detector.

particle from being a neutron, therefore the neutral particle must be a photon. All indications of the experimental data suggest that the untracked clusters in the exclusive region are being produced from photons originating at (or near) the event vertex. The photons, however, may be produced from decays of neutral particles such as the π^0 or η instead of the desired BH and DVCS processes. An estimate of the photons produced in decays of neutral particles will be presented in Sec. 4.7.2.2.

The energy resolution of the photons has been studied by the calorimeter group [64] and found to be given by:

$$\frac{\sigma(E)}{E}[\%] = \frac{(5.1 \pm 1.1)}{\sqrt{E\ (GeV)}} + (2.0 \pm 0.5) + \frac{(10.0 \pm 2.0)}{E\ (GeV)}. \tag{4.6}$$

For the single photon production in the exclusive region, where the average photon energy is $\sim$ 12 GeV, the average energy resolution is ~ 0.52 GeV. An inconsistent calibration of the energy was discovered during this analysis, which is dependent on the preshower response. The energy for the calorimeter has been calibrated with positrons, to ensure that the average energy measured by the calorimeter has the same value as the momentum measured by the magnetic field of the HERMES spectrometer magnet ($\langle E/p \rangle = 1$). The positrons used in the calorimeter calibration are identified with conservative constraints on the PID detector responses. The preshower counter, using these conservative constraints, is required to have an energy deposition greater than minimum ionization, therefore, the calibration positrons all must have started a showering process in the lead sheet of the preshower.

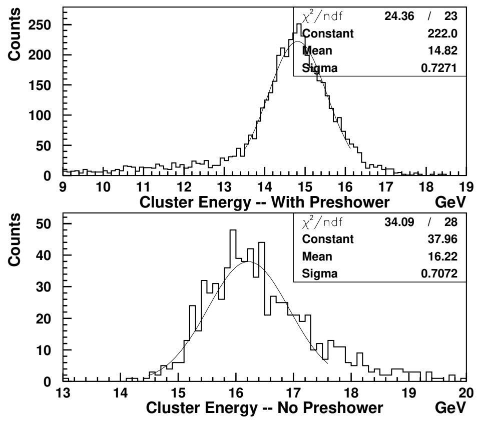

Figure 4.14: The distribution of the reconstructed calorimeter energy from a MC simulation using generated photons of 15 GeV in which there was a preshower response (top panel) and in which there was no response in the preshower (bottom panel).

The calibration of the photon energy is significantly different if the photon passes undisturbed through the preshower detector and starts the showering process in the calorimeter. A photon beam will be attenuated by $\sim$ 78% as it traverses the preshower as explained previously in Sec. 3.6. However $\sim$ 22% of the photons will pass un-hindered through the preshower, and will not start the showering process until entering the calorimeter block. The position of peak Čerenkov light emission for these photons will be at a closer distance to the calorimeter PMT tube and less attenuated by the lead-glass of the calorimeter. Therefore, the signal of the PMT will be larger, and since the same calibration is used for all photons, will be assigned a higher energy. An example is shown in Fig. 4.14, of a HERMES Monte Carlo simulation of the reconstructed energy using 15 GeV generated photons. The reconstructed energy of the photons with a preshower signal is consistent with the initial 15 GeV, however, the photons with no response in the preshower detector are reconstructed with a much larger average energy of $\sim$ 16 GeV. This $\sim$ 10% error will increase the resolution in missing mass, and result in a less exclusive measurement. In order to correct the 20% affected events, a detailed Monte Carlo study is needed. For this analysis, it was decided to remove the events which had no preshower signal for the untracked cluster, resulting in a more exclusive sample, but with a 20% loss in statistics.

The reconstructed cluster position has a resolution on the order of several centimeters which depends on the relative position in the calorimeter block. This dependence was investigated and shown to arise from an unsophisticated algorithm and will be discussed in greater detail in Sec. 4.6.5.

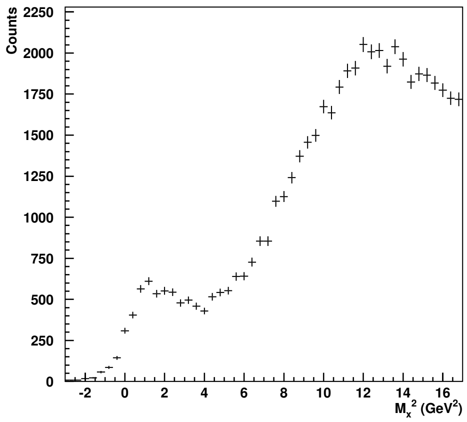

Figure 4.15: The distribution of reconstructed missing mass squared (M_x^2) for the 1996 and 1997 datasets.

4.4.3 Recoil Proton Checks

The recoil proton is seldom detected in the HERMES spectrometer as the angular acceptance of the spectrometer is limited to the forward angles. The recoil proton has a momentum on the order of the square root of the Mandelstam invariant $\sqrt{|t|}$, which for the single photon production data in the exclusive region has an average magnitude of $\sqrt{|t|} = 0.5$ GeV/c. The recoil proton has limited momentum therefore, and will not be focused in the forward direction in the lab, as are the positron and photon. The recoil protons which are in the HERMES angular acceptance do not have enough momentum to transverse through the entire spectrometer, and have limited momentum resolution and virtually no particle identification. A detector is being built for the HERMES spectrometer which will be mounted around the target and have good acceptance and momentum determination [78]. For the present analysis, the missing mass squared of the events is reconstructed (see Eq. 4.5). The distribution of the lower domain of the squared missing mass is displayed in Fig. 4.15 illustrating the exclusive peak. The detector has limited resolution which can give rise to negative values of M_x^2. In addition, the finite resolution does not allow a selection of purely exclusive events. The resolution of the missing mass has been estimated with a Monte Carlo simulation using the DIS generator PEPSI. The DVCS process is not included in the MC simulation so the single photon generation in the exclusive region arises mainly from the BH process. An estimation of the missing mass resolution arising from the detector can, however, be obtained from the BH process as it has the identical final state as DVCS. The MC simulated single photon data were analyzed using the identical constraints as in the experimental data extraction. The MC simulation describes the experimental data fairly well as illustrated in Fig. 4.16,

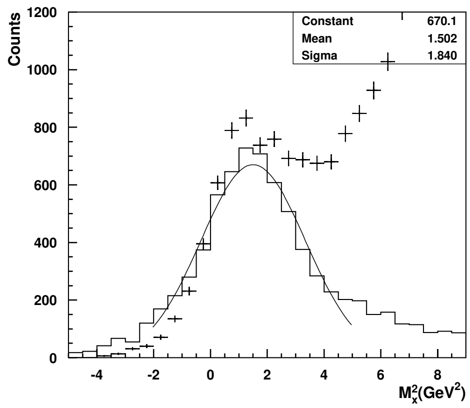

Figure 4.16: The distribution of reconstructed missing mass squared (M_x^2). The MC simulated BH events (histogram) along with a Gaussian fit of the central distribution are shown with the experimental data (points).

in particular the central peak position of the exclusive region (see also Fig. 4.6). A Gaussian fit to the BH process of the MC simulation gives the central value of 1.502 GeV^2 with a width (sigma) of 1.840 GeV^2. For an interaction which leaves the proton intact, the central peak position should be at 0.938^2 GeV^2 $= 0.880$ GeV^2. The offset in both the experimental data and MC simulation indicate that the reconstruction of the missing mass is not quite accurate. Since the HMC simulation has adequately described other DIS analyses for charged particles, the most likely problem is with the energy or position reconstruction of the photon. A problem with the photon energy has been noticed in HERMES analyses involving the π^0 mesons and is corrected for by an offset factor $(0.95 - 0.98)$ to the reconstructed photon energy [79,80]. However, a definite solution to the problem has not yet been developed.

The measured resolution estimate (sigma) of 1.840 GeV^2 was converted to a resolution in missing mass with the equation:

$$M_x = \sqrt{M_x^2}\,, \tag{4.7}$$

$$\delta(M_x) = \frac{dM_x}{dM_x^2}\delta(M_x^2) = \frac{1}{2M_x}\delta(M_x^2)\,, \tag{4.8}$$

where the MC reconstructed variables M_x and $\delta(M_x^2)$ are used. This results in an estimated missing mass resolution of ~ 0.75 GeV. However, this estimate may not accurately reflect the detector resolution, as the central missing mass value (MC and experimental) is not at the proton mass of 0.938 GeV. Another resolution check was made with the MC simulated data by correcting the reconstructed photon energy. For this check, a constraint was placed on the generated missing mass,

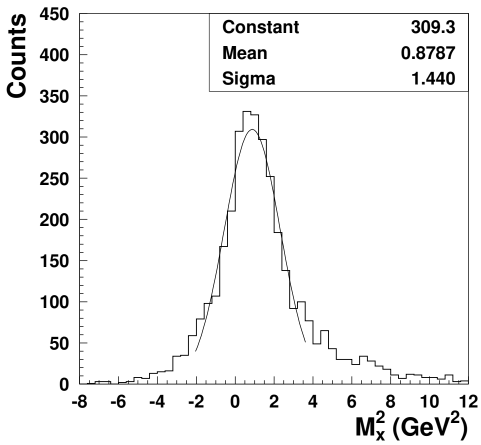

Figure 4.17: The distribution of reconstructed missing mass squared (M_x^2) for the MC simulated BH events along with a Gaussian fit of the central distribution.

so that it corresponded to the proton mass of 0.938 GeV. The photon energy was changed until the missing mass squared distribution was peaked at the correct value of 0.880 GeV^2 (see Fig. 4.17). The width of the central Gaussian fit (1.440 GeV^2) resulted in an estimated missing mass resolution of ~ 0.77 GeV, which is similar to the first estimate. Therefore, a missing mass resolution arising from the finite resolution of the detector is estimated to be ≈ 0.8 GeV for this single photon analysis.

4.5 Asymmetry Extraction

The observable of interest in this single photon analysis is the single spin asymmetry with respect to the azimuthal distribution. The single spin asymmetry has a $\sin\phi$ dependence in the leading-order formalism, where ϕ is the azimuthal angle of the produced photon with respect to the virtual photon direction. The value of the asymmetry can be extracted in several ways. The azimuthal distribution of the single spin asymmetry can be formed, and the resulting distribution fit with a $\sin\phi$ function. Or alternatively, a $\sin\phi$ moment can be formed which will extract the $\sin\phi$ dependence due to the orthogonality of the Fourier series. Both methods should provide good estimators of the asymmetry.

The azimuthal dependence of the single spin asymmetry is defined as:

$$A_{LU}(\phi) = \frac{1}{\langle|P_l|\rangle} \cdot \frac{N^+(\phi) - N^-(\phi)}{N^+(\phi) + N^-(\phi)}. \tag{4.9}$$

Here N^+ and N^- represent the luminosity normalized yields of events in the two beam helicity states, $\langle|P_l|\rangle$ is the magnitude of the average beam polarization, and the subscripts L and U denote a longitudinally polarized beam and an unpolarized target. The luminosity for a burst was calculated as the product of the luminosity rate obtained from the luminosity monitor, the live time percentage, and the burst length. The total luminosity was a sum over all bursts which satisfied the data quality constraints. The total luminosity was calculated separately for each helicity state of the beam, and used to normalize the number of events in the single spin asymmetry equation of Eq. 4.9. The average beam polarization over both helicity states is taken into account so the result can be more easily compared to model calculations and different experiments. For the 1996 and 1997 datasets, the average polarization was $\sim 0.53 \pm 0.02$ with very similar polarization averages for each helicity state. The single spin asymmetry as a function of the angle ϕ has a definite $\sin\phi$ dependence in the exclusive region (see Fig. 4.18). The simple $\sin\phi$ dependence is not present in the higher missing mass regions as illustrated by Fig. 4.19. In order to extract the $\sin\phi$ dependence in the exclusive as well as the non-exclusive region, the $\sin\phi$-weighted moments have been determined:

$$A_{LU}^{\sin\phi\pm} = \frac{2}{N^{\pm}} \sum_{i=1}^{N^{\pm}} \frac{\sin\phi_i}{|P_l|_i}, \tag{4.10}$$

where the superscript $\pm$ refers to the helicity of the positron beam. The moment is the average value of $\sin\phi$ which is one-half the amplitude of the $\sin\phi$ distribution. The factor of 2 in Eq. 4.10 converts the moment into an amplitude which can be directly compared to the fit of the azimuthal distribution of the single spin asymmetry. The $\sin\phi$ moments show a non-zero value in the exclusive region and are consistent with zero in the non-exclusive regime (see Fig. 4.20). One can also see that the sign of the moments is opposite for the two beam helicities in agreement with the expectation for the helicity dependence of the BH-DVCS interference term. Also, the beam-spin averaged data are consistent with zero, which is expected from an unpolarized beam and target.

The data in the two beam-helicity states contain the same physics information and can be combined into the beam-spin analyzing power $A_{LU}^{\sin\phi}$:

$$A_{LU}^{\sin\phi} = \frac{2}{N} \sum_{i=1}^{N} \frac{\sin\phi_i}{(P_l)_i}, \tag{4.11}$$

where $N = N^{+} + N^{-}$. Here the sign of the beam polarization is not suppressed as in Eq. 4.10. The beam-spin analyzing power has a negative value in the exclusive region and approaches zero for larger missing mass values as shown in Fig. 4.21. Due to the finite resolution of the spectrometer, the beam spin asymmetry is non-zero for the missing mass bins to the left and right of the exclusive bin of $0.4 < M_x < 1.4$ GeV. The single photon data show the same behavior as the expectations for the interference term of the BH and DVCS processes, a non-zero value in the exclusive region which approaches zero at higher missing mass, and the difference in the sign of the moments for the two

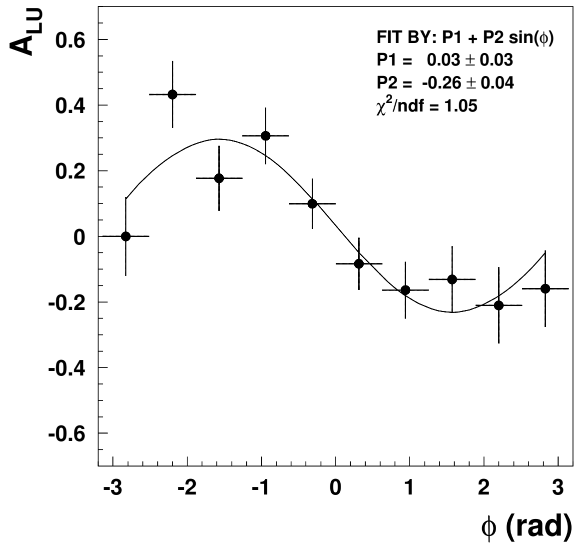

Figure 4.18: The beam spin asymmetry A_{LU} for the hard electroproduction of photons as a function of the azimuthal angle ϕ in the exclusive region. The data correspond to the exclusive missing mass region between -1.5 and +1.7 GeV. The error bars represent the statistical uncertainty only.

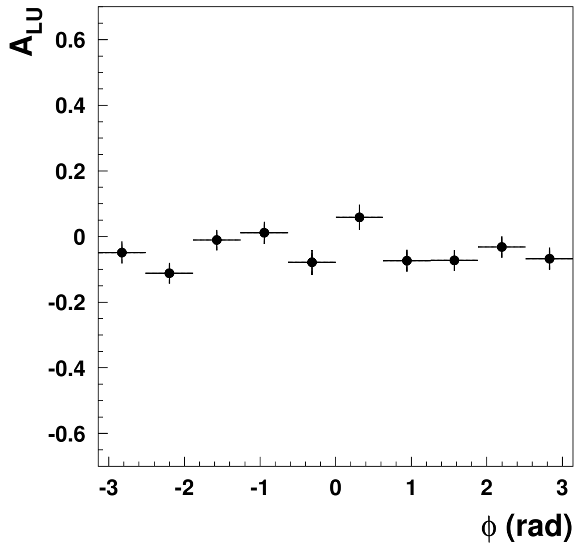

Figure 4.19: The beam spin asymmetry A_{LU} for the hard electroproduction of photons as a function of the azimuthal angle ϕ in the non-exclusive region. The data correspond to the exclusive missing mass region between 3.4 and 4.4 GeV (highest statistics bin). The error bars represent the statistical uncertainty only.

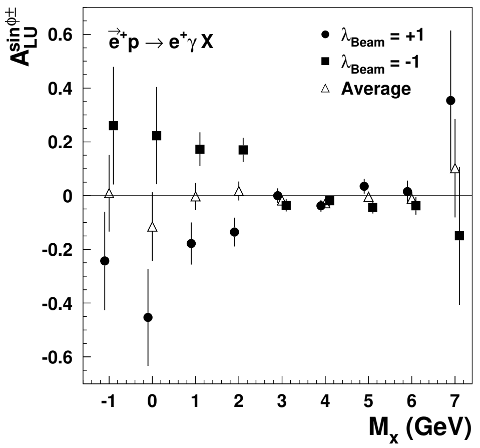

Figure 4.20: The $\sin\phi$-moment $A_{LU}^{\sin\phi\pm}$ as a function of the missing mass for positive beam helicity (circles), negative beam helicity (squares) and the averaged helicity (open triangles). The error bars represent the statistical uncertainty only.

beam helicities. To ensure the asymmetry is arising from the BH and DVCS interference term, a number of checks were undertaken.

4.6 Preliminary Asymmetry Checks

The asymmetry was formed and checked for stability against different divisions of the data. The data were divided into different time periods, and different groupings of the detected photon position. Also, to check for the stability of the detector over the long period between the beam helicity rotations, an unpolarized-beam, polarized-target asymmetry was formed. Finally, the possible effect on the asymmetry due to the constraint on the preshower detector was investigated.

4.6.1 Division of the Data by Year

The single spin asymmetry for the 1996 data (positive beam helicity only) was compared to the asymmetry for the 1997 positive beam helicity data, to ensure that the data were consistent between the years. As the 1997 event sample for the positive helicity state has limited statistics, a more relaxed constraint of the opening angle $\theta_{\gamma*\gamma}$ of 0.005 rad was used for this check, which does not have a significant effect on the asymmetry as will be discussed in Sec. 4.6.5. In Fig. 4.22 the two single spin asymmetries for the positive helicity state are shown, which are consistent within the statistical uncertainties. This check indicates that there are no major differences between the two data taking periods, although the statistical precision is limited.

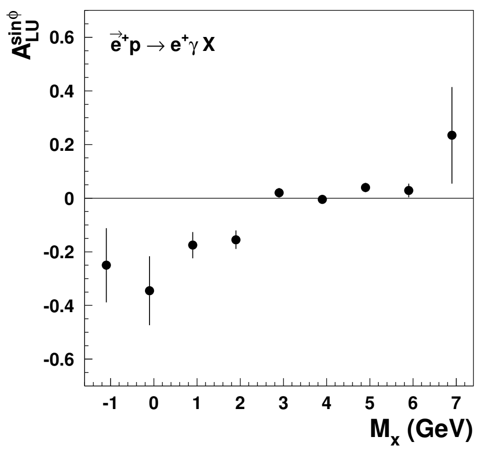

Figure 4.21: The beam-spin analyzing power $A_{LU}^{\sin\phi}$ for the hard electroproduction of photons as a function of the missing mass. The error bars represent the statistical uncertainty only.

4.6.2 Division of the Data by Photon Position

The data were divided into groups using the centroid position of the photon cluster for the exclusive region of -1.5 to 1.7 GeV to ensure the asymmetry was consistent in all regions of the detector. The data were divided into groups where the photon was detected in the top and bottom detector halves, as well as the positive x direction (left) and negative x direction (right). The asymmetry was constructed from a fit of the azimuthal distribution as well as from a $\sin\phi$ moment. The asymmetry is consistent against divisions of the detector within the statistical uncertainty as shown in Fig. 4.23. The asymmetry constructed from two different methods is also consistent, indicating that the uncertainty due to the acceptance of the spectrometer is small compared to the statistical precision (the acceptance issue is discussed in more detail in Sec. 4.7.2.5).

4.6.3 Polarized target asymmetry

Most of the asymmetries analyzed at HERMES require a rotation in either the target or the beam helicity. The target helicity is most easily changed, and is randomly flipped every 1-2 minutes. The beam helicity can be changed at the HERMES experiment by changing the direction of the spin rotators. However, the beam helicity change requires an access to the accelerator tunnel, and is therefore not often changed. The beam helicity remained $+1$ for the entire 1996 data taking period. The beam helicity was changed 3 times in 1997 with a beam helicity of -1 maintained for the majority of the time. Since the time scale for changing the beam helicity is rather large, a check was made taking advantage of the hydrogen data obtained from a polarized target.

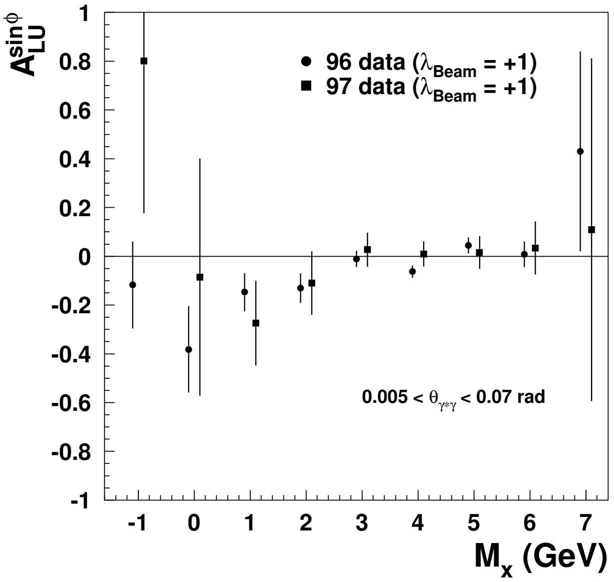

Figure 4.22: The comparison of the positive helicity single spin asymmetry for the 1996 and 1997 data sets versus the missing mass.

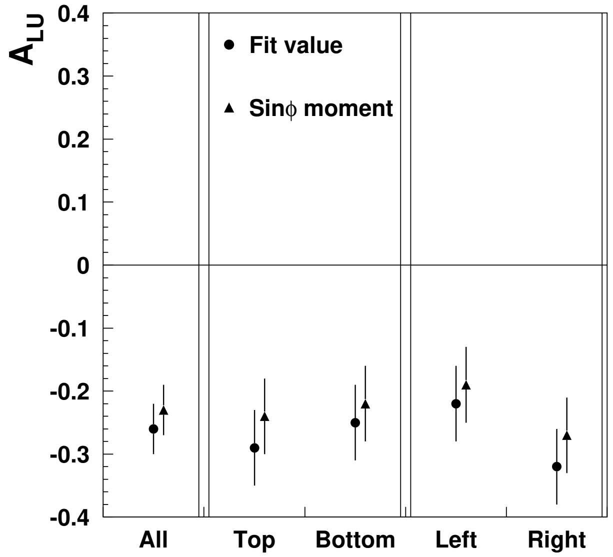

Figure 4.23: The asymmetry from a $\sin\phi$ fit to the azimuthal distribution as well as the $\sin\phi$ moment, versus divisions of the data with respect to the detected photon position.

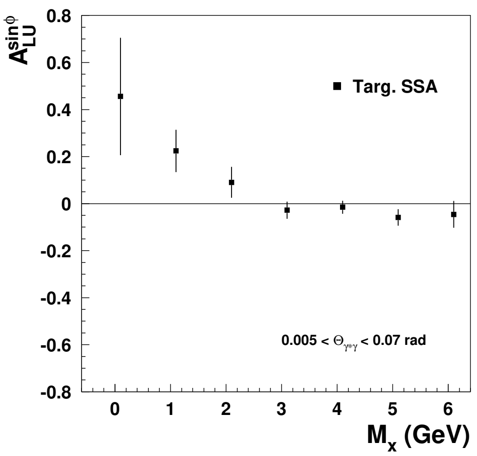

Figure 4.24: The target single spin asymmetry from the 1997 hydrogen polarized target data, where the sample has been beam-helicity balanced to ensure an average beam polarization of zero.

Following the formalism of Ref. [47], a difference of helicity cross sections (asymmetry) for an unpolarized beam and longitudinally polarized target can be formed:

$$\begin{aligned} d\sigma_{\uparrow} - d\sigma_{\downarrow} &= \frac{16(2-2y+y^2)\sqrt{1-x_{Bj}}}{\sqrt{1-y}yx_{Bj}\sqrt{tQ^2}}\sqrt{1-\frac{t_{min}}{t}}\sin\phi \\ &\times \Im m \left\{ \begin{array}{c} \frac{x_{Bj}}{2-x_{Bj}}(F_1+F_2)\left(\mathcal{H}_1 + \frac{x_{Bj}}{2}\mathcal{E}_1\right) + F_1\widetilde{\mathcal{H}}_1 \\ +\frac{x_{Bj}}{2-x_{Bj}}\left(\frac{x_{Bj}}{2}F_1 - \frac{t}{4M^2}F_2\right)\widetilde{\mathcal{E}}_1 \end{array} \right\} d\mathcal{M}\,, \end{aligned} \tag{4.12}$$

using the same definitions as in Eq. 2.103 of Sec. 2.4.1.

The hydrogen data obtained from a polarized target are a subset of the total 96/97 hydrogen dataset, and can be used to form a single target-spin asymmetry. However, an unpolarized beam is needed for a single target-spin asymmetry (since the beam-spin asymmetry also has a non-zero $\sin\phi$ dependence) therefore the polarized target data have to be helicity balanced with respect to the beam polarization. These constraints dramatically reduce the available statistics and the precision of this type of asymmetry. However, the asymmetry can still be used as a check to ensure that the observed single spin asymmetry arises from the interference of the BH and DVCS processes, and not from a time-dependent detector effect. The polarized target asymmetry does not have the same amplitude as the single beam-spin asymmetry due to different kinematic dependences, and should be of opposite sign according to Eqs. 2.103 and 4.12. Shown in Fig. 4.24 is the asymmetry from the beam-helicity balanced data from the 1997 polarized hydrogen target data set. The asymmetry has the opposite sign from the beam-spin asymmetry and is on the same order of magnitude in the exclusive region, approaching a value consistent with zero in the non-exclusive region. The consistency of the target-

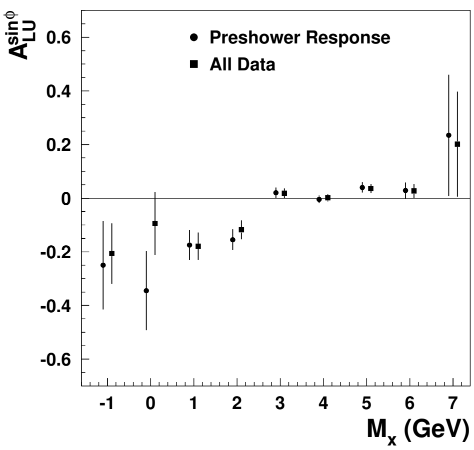

Figure 4.25: The single spin asymmetries for the data having a preshower response compared to all single photon data versus the missing mass.

spin asymmetry with the expectation indicates that the time scale of the beam helicity changing does not have a significant effect for the beam-spin asymmetry.

4.6.4 Preshower Constraint

The single photon events where the untracked cluster did not produce in a response in the preshower were not used in the data selection process, as the energy of these photons were reconstructed with the incorrect energy as was explained in Sec. 4.4.2. The constraint reduces the event statistics by $\sim 20\%$, and so could have only a minor possible effect on the asymmetry. To check for a possible effect, the asymmetry was constructed with and without the constraint on the preshower detector. The results are consistent within the statistical precision or the measurement (see Fig. 4.25). The asymmetry in the $1.4 - 2.4$ GeV missing mass bin is reduced without the constraint on the preshower response, confirming the expected increased contribution of non-exclusive events.

4.6.5 Calorimeter Position Reconstruction

The calorimeter was commissioned primarily as a particle identification detector (PID) as the charged particle energies are measured more accurately by reconstructing the bending of the tracks in the magnetic field, using the tracking detectors. The momentum of the particles is extracted from the bending angle and, with the particle identification from the HERMES four PID detectors, the energy can be obtained. The energy obtained using the tracking detectors and the magnet is more accurate than the energy obtained from the calorimeter. Therefore, the energy measured using the calorimeter is only used for analyses of neutral particles. As the main HERMES analysis focus is with charged particle events, the algorithms used to reconstruct the position and energy of the cluster in the calorimeter were not optimized for neutral particles. For neutral particle analyses, such as the single photon analysis, the position and energy reconstruction of the calorimeter needs to be as precise as possible.

The centroid of the clusters is reconstructed in the HERMES ReConstruction program (HRC) as discussed in Sec. 4.1.2. The reconstructed centroid position is calculated separately for each direction (x and y) using a square root energy weight (w_i)

$$x_{rec} = \frac{\sum_{i=1}^{9} w_i x_i}{\sum_{i=1}^{9} w_i} \quad \text{with} \tag{4.13}$$

$$w_i = \sqrt{E_i}\,, \tag{4.14}$$

where x_i is the center of each block in the sum, obtained from the geometry of the calorimeter, and the sum is over the peak energy block and the eight surrounding blocks. The square root weighting does not reproduce the true position, but biases the position toward the center of the peak block. This is shown in Fig. 4.26, where the random distribution of clusters has reconstructed cluster positions concentrated in the middle of the calorimeter blocks. To illustrate the effect in a different manner, charged particle tracks and their associated clusters were compared. Ten runs from the 1997 dataset were used to extract the difference of the cluster position and the projected track position at the z-position of the calorimeter of 745 cm for both the x and y directions (see Fig. 4.27). The difference in the track and cluster positions appears to be two smeared Gaussian distributions for the horizontal (x) case and a more complicated distribution in the vertical (y) case, most likely due to the vertical separation of the two halves of the calorimeter.

To investigate this behavior further, a simple Monte Carlo generator was used to generate a single 15 GeV photon at a fixed vertical (y) position and randomly across a single block in the horizontal (x) direction. The generated photon was input into the HERMES Monte Carlo (HMC) and the HRC programs to obtain the central x and y positions of the reconstructed cluster. The generated and reconstructed x positions are compared in Fig. 4.28. Here the well known "S-curve" behavior is shown arising from the nonlinear dependence of the reconstructed position. The lateral shower profile has an exponential shape, but the reconstruction uses a square root energy weighting, which causes the nonlinear behavior. The variation of the reconstructed position about the center of the S-curve has a half width of ~ 0.5 cm. The nonlinear behavior causes a position bias which, in addition to the variation, results in an increased uncertainty of the position of the reconstructed cluster. The

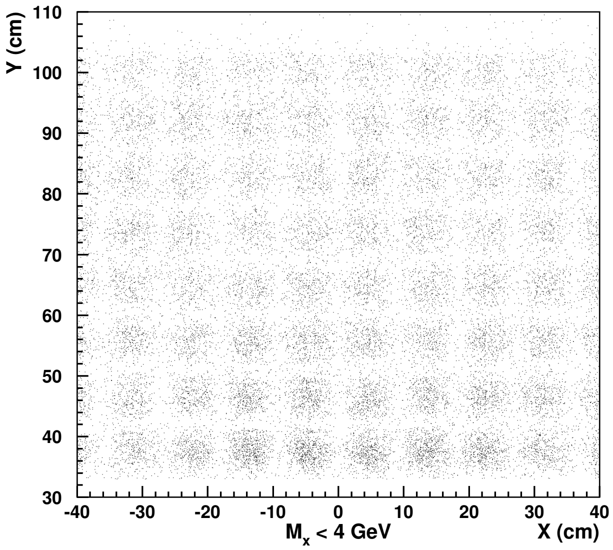

Figure 4.26: The cluster position in the central section of the top calorimeter. Data are from the 96/97 single photon analysis with a reconstructed missing mass M_x less than 4 GeV.

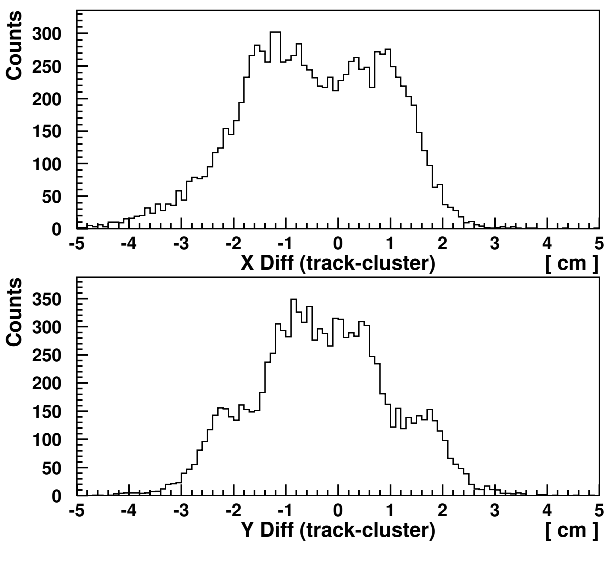

Figure 4.27: The difference in the track and cluster positions for charged tracks taken from 10 runs of the 1997 dataset.

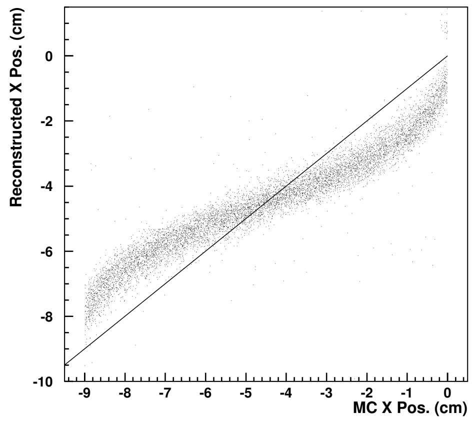

Figure 4.28: A scatter plot of the calorimeter x position reconstructed by HRC versus the generated (true) x position for a single calorimeter block. The line represents the perfect case (reconstructed x = generated x).

position bias can be as large as several centimeters which may effect the single photon analysis in several ways. First, the position of the cluster may affect the reconstructed missing mass. The missing mass resolution is, however, dominated by the energy resolution of the calorimeter; the uncertainty in the position has a negligible effect. Secondly, the uncertainty may affect the single spin asymmetry. The asymmetry is a beam-spin asymmetry with respect to the azimuthal angle between the scattering and production plane (around the virtual photon direction). Smearing of the cluster position affects the calculation of the correct azimuthal angle, and may affect the asymmetry. The effect should be minimal in a $\sin\phi$ moment, as the moment suppresses the event weight at $\phi = 0,\ \pi$. However, to ensure that the effect would be negligible, a lower bound was placed on the opening angle between the virtual photon and the produced photon ($\theta_{\gamma^*\gamma}$) at 0.015 radians. The value of 0.015 radians was chosen using a simple geometric argument and the observed resolution of the cluster positions. The 0.015 radian constraint corresponds to approximately 11 cm at the z-position of the calorimeter (745 cm). For the present cluster position reconstruction algorithm the position bias can be several centimeters, as shown in Fig. 4.27. If one assumes an average position shift of 2 cm, the corresponding uncertainty in the azimuthal angle ϕ is roughly $2/11 \approx 0.18$ radians. If all events were at $\theta_{\gamma^*\gamma} = 0.015$ and all events with $|\phi| < 0.18$ or $|\phi| > \pi - 0.18$ shift in such a way to form a zero asymmetry, then the fraction of events contributing zero asymmetry would $\sim 2 \cdot 0.18/\pi \approx 11\%$. This would cause an undesirable dilution of the measured asymmetry. Both of the above are extreme assumptions corresponding to a maximum upper limit, however, the limit was set to ensure minimal dilution of the asymmetry. A decrease in the position bias of the cluster reconstruction would allow a reduction in the lower $\theta_{\gamma^*\gamma}$ constraint and more events could be available for the analysis.

There are several methods of reducing the position bias. The most effective method is to correct for the position bias using the true shower profile for the energy and impact angle of the cluster [81–83]. However, the true shower profile must be known or obtainable. The shower profile can usually be described by a sum of two exponentials dependent on the energy of the showering particle, and which can be parameterized by large statistical studies of shower profiles. Alternatively, a shower profile can be estimated at first order and the position bias correction iterated [81]. Another method incorporates the exponential shape of the shower in the position reconstruction itself, by using logarithmic weighting schemes [81, 82]. This type of method is attractive as no extra bias correction is needed, and no information on the shower profile is needed a priori. A simple type of logarithmic weighting described in Ref. [82], was studied and implemented for the cluster reconstruction for the beam pipe calorimeter of the ZEUS experiment [83], and produces little bias. It requires no previous knowledge of the shower profile, and has less energy and angle dependence than other methods.

The weight used to determine the cluster position in this method is defined as

$$w_i = max\{0,\ W_0 + ln\frac{E_i}{\sum E_i}\}. \tag{4.15}$$

This weight is then used in the reconstructed position equation,

$$x_{rec} = \frac{\sum w_i x_i}{\sum w_i}. \tag{4.16}$$

The threshold cutoff parameter W_0 reduces background by excluding signals with an energy below a certain threshold. The cutoff parameter is optimized through MC simulation and is a balance between the bias and the variation due to fluctuations. As the cutoff parameter becomes smaller, fewer blocks are allowed to contribute in the position reconstruction and the background fluctuation variance will reach a minimum, but the position bias will increase. Increasing the cutoff parameter allows more blocks in the sum and the average position is more accurate (reduced bias), but the fluctuation variance becomes larger.

A MC study was performed to investigate the dependence of the cutoff parameter W_0 on the position bias and variance of the reconstructed cluster position. A simple single photon generator of various energies was used to produce the initial events for the HMC and HRC programs. The cluster positions were reconstructed using the logarithmic weighting method of Eq. 4.16, for different values of the cutoff parameter. An S-curve plot was made for each cutoff value similar to Fig. 4.28. The maximum position bias was measured as the maximum perpendicular distance from the center of the

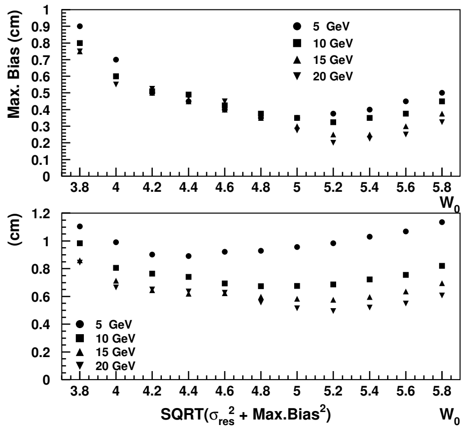

Figure 4.29: The dependence on the cutoff parameter W_0. The top plot shows the position bias as a function of W_0 while the bottom plot shows the dependence on the quadratic sum of the position bias and variance.

S-curve to the perfect value line at 45°. This is the maximum amount the S-curve would have to be shifted to remove the position bias. The variance, on the other hand, was measured as the variance (σ) of a Gaussian fit to a perpendicular slice of the S-curve. It is the estimate of the variance that would remain if the position bias was totally removed. The position bias is minimized for the studied photon energies using a cutoff parameter W_0 between 5.0 and 5.4 (see Fig. 4.29). The variance is minimized at a much lower value of $W_0 \sim 2.5$ (not shown). Combining the position bias and the variance quadratically results in minima for a W_0 between 4.3 and 5.2 (see bottom plot of Fig. 4.29). This quadratic combination is an estimate of the true resolution of the cluster position reconstruction, and approaches a minimum of 0.5 cm for the higher energy photons. The W_0 dependence on this "resolution" is not strong therefore a constant value of $W_0 = 4.8$ was selected.

For a more accurate position reconstruction, the incident angle of the photon was taken into account empirically. A simple linear equation for the possible position offset arising from the incident angle was formed as:

$$X_{\text{offset}} = A_x \cdot z \cdot \theta + B_x \ , \tag{4.17}$$

$$Y_{\text{offset}} = A_y \cdot z \cdot \theta + B_y \ , \tag{4.18}$$

where z is the calorimeter position at 745 cm, θ is the polar angle of the photon, and the A's and B's are constant parameters. The constants are obtained by minimizing the width of the distribution of the differences in the charged track and the cluster positions. The angle correction is made by adding

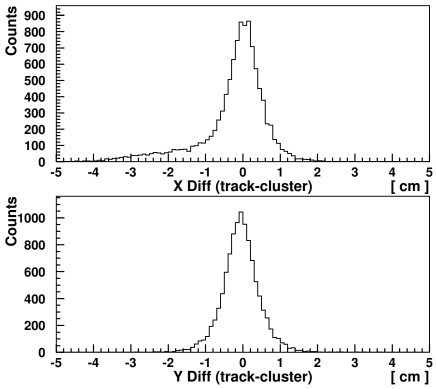

Figure 4.30: The difference in the track and cluster positions for charged tracks taken from same 10 runs of the 1997 dataset as in Fig. 4.27 using the new calorimeter reconstruction algorithm.

the offset to the reconstructed position to obtain the corrected values

$$X_{\rm cor} = X_{\rm rec} + X_{\rm offset} \ , \tag{4.19}$$

$$Y_{\rm cor} = Y_{\rm rec} + Y_{\rm offset} \ . \tag{4.20}$$

The minimized logarithmic weighted distributions of the differences in the charged track and the cluster positions are shown in Fig. 4.30. The peak in each plot is now a single peak unlike the peaks of Fig.4.27, and the widths are much narrower. The asymmetric tail in the differences of the x positions is due to the positron radiating in the magnetic field. Since the positrons are all bent in one direction, the cluster positions will all be offset to one side of the positron track, if the radiated photon was produced inside the magnetic field. The half width of the peaks (σ) is approximately 0.5 cm, which is a great improvement over the energy square root weighting scheme. The improvement can also be seen in Fig. 4.31, the same plot as in Fig. 4.26, where now the cluster position are approaching a truly random pattern. There is some small bias present as illustrated by the still visible lines. These lines are in the center of the blocks, and represent clusters where the majority of the surrounding blocks are discarded due to a low energy. For these low energy clusters a different cutoff parameter W_0 is needed, suggesting W_0 should be energy dependent and not a constant.

To illustrate the possible effect on the asymmetry of the different weighting schemes, the asymmetry was calculated for both position reconstruction methods and two different values of the lower opening angle constraint. In Fig. 4.32, the single spin asymmetry was formed for both cluster position reconstruction methods, using a $\theta_{\gamma^*\gamma} > 0.015$ radian constraint. The results are consistent within

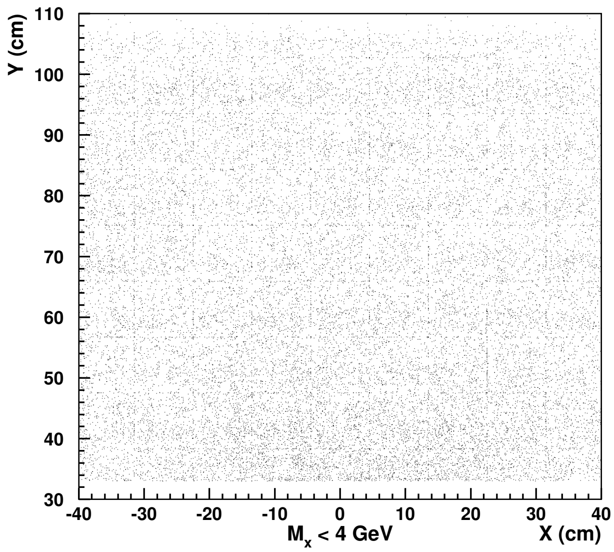

Figure 4.31: The cluster position in the central section of the top calorimeter. Data are from the 96/97 single photon analysis with a reconstructed missing mass less than 4 GeV. Cluster position reconstruction using the logarithmic weighting and angle correction.

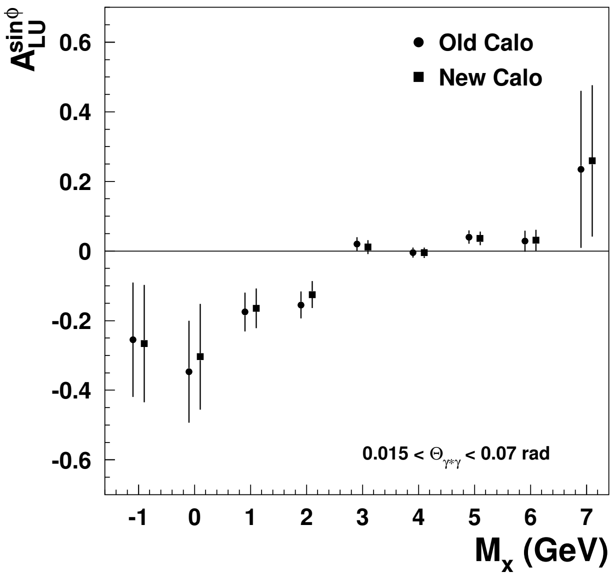

Figure 4.32: The single spin asymmetry as a function of the missing mass (M_x) from the single photon analysis for the square root weighting (Old Calo) and logarithmic weighting (New Calo) cluster position algorithms for a lower bound on the opening angle ($\theta_{\gamma^*\gamma}$) of 0.015 radians.

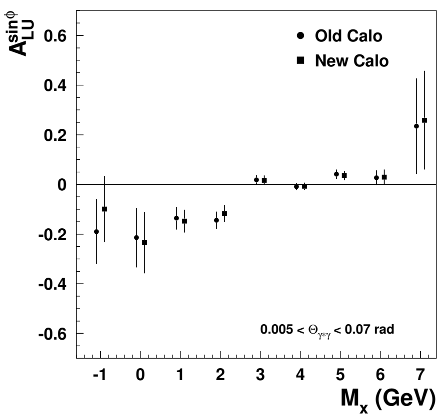

Figure 4.33: The single spin asymmetry as a function of the missing mass (M_x) from the single photon analysis for the square root weighting (Old Calo) and logarithmic weighting (New Calo) cluster position algorithms for a lower bound on the opening angle ($\theta_{\gamma^*\gamma}$) of 0.005 radians.

the statistical uncertainties, which confirms the assumption that the constraint on $\theta_{\gamma^*\gamma}$ minimizes the effect of the cluster position resolution. The same plot is shown in Fig. 4.33, with a constraint on the lower limit of 0.005 radians for the opening angle. This plot shows that the asymmetries for both reconstruction methods are still consistent within the statistical uncertainties. This is perhaps an indication that the position smearing effect on the asymmetry was over-estimated, and the lower constraint of 0.015 mrad on $\theta_{\gamma^*\gamma}$ is too conservative for the single photon analysis. The improvement in the cluster position reconstruction algorithm does not affect the single spin asymmetry when decreasing the lower bound on the opening angle to 0.005 radians, however, the selected number of events (and hence measurement precision) will increase. The improved calorimeter reconstruction algorithm is planned to be included into the HRC program, and a new production of the data completed in the future. With the new production, the reduction of the lower opening angle constraint to a value of 0.005 rad will increase the data sample by $\approx$ 25%, reducing the statistical uncertainty by from $0.042 \rightarrow\sim 0.035$.

4.7 Corrections to the Asymmetry and Estimation of Uncertainties

The purpose of a measurement is to obtain a value of a physical quantity. The best measurement would be infinitely precise and correspond to the true value of the physical quantity. Unfortunately, in the real world, the measurement is only a best estimate of the true value, and is characterized by some uncertainty. The uncertainty is usually divided into two sources, one arising from the number of observations (statistical) and the other from the limited precision of the experimental measurement itself (systematic). The statistical uncertainty arises from random variations in the results of repeated observations under identical conditions. These uncertainties (usually) become negligible when the number of observations becomes very large. Systematic uncertainties, on the other hand, can only be reduced by improving the measurement apparatus or technique. In most cases, the statistical and systematic uncertainties are considered uncorrelated and ultimately added together in quadrature.

4.7.1 Statistical Uncertainty of the Asymmetry

The limited number of observations (events) of the single photon production lead to a random statistical uncertainty in the measurement of the asymmetry. When the asymmetry is obtained from a fit to the azimuthal distribution as in Fig. 4.18, the calculation of the statistical uncertainty is straightforward, although two calculations are required. First, the statistical uncertainty in the single spin asymmetry for each ϕ bin is calculated, then the statistical uncertainty of the fit is determined. The first calculation follows from a simple derivative of the asymmetry equation (Eq. 4.9):

$$A_{LU}(\phi) = \frac{1}{\langle|P_l|\rangle} \cdot \frac{N^+(\phi) - N^-(\phi)}{N^+(\phi) + N^-(\phi)}, \tag{4.21}$$

$$\delta A_{LU}(\phi) = \frac{1}{\langle|P_l|\rangle} \cdot \frac{1 - A_{LU}^2}{2} \sqrt{\left(\frac{1}{N^+(\phi)} + \frac{1}{N^-(\phi)}\right)}, \tag{4.22}$$

assuming the events are Poisson distributed ($\delta N = \sqrt{N}$). The uncertainty on the fit process depends on the minimization procedure and the number of parameters (or bins in the azimuthal angle) used in the fit. For this analysis, the least squares method of minimization was used and the usual one standard deviation of the fit determines the uncertainty. The azimuthal asymmetry was divided into ten bins, optimized by balancing the limited statistics with a precise estimate of the distribution shape. No correlations between the bins were taken into account for the statistical uncertainty. Any correlations should be small as the angular resolution in the azimuthal angle is approximately one order of magnitude smaller than the bin size. The uncertainty in the fit is assumed here to be dominated by statistics and not by the choice of the fit function, and is therefore used as the final statistical uncertainty.

For the $\sin\phi$ moment asymmetry evaluation, the statistical uncertainty is not a straightforward differentiation of the $\sin\phi$ function but the definition of a variance must be used:

$$s^2 = \frac{\sum(x_i - \bar{x})^2}{N - 1}, \tag{4.23}$$

where the sum is over all x_i events, N is the number of events, and the estimate of the mean ($\bar{x}$) is given by:

$$\bar{x} = \frac{\sum x_i}{N} . \tag{4.24}$$

For the $\sin\phi$ moment, this equates to:

$$\langle \sin\phi \rangle = \frac{1}{N} \sum \sin\phi_i \, , \tag{4.25}$$

with the uncertainty:

$$\delta\langle \sin\phi \rangle^2 = \frac{1}{N-1} \sum \left(\frac{\sin\phi_i}{N} - \frac{\langle \sin\phi \rangle}{N} \right)^2 . \tag{4.26}$$

With a little mathematical manipulation, the above can be transformed into an equation requiring only a single sum over the data:

$$\delta\langle \sin\phi \rangle^2 = \frac{N}{N-1} \sum \left(\frac{\langle \sin^2\phi_i \rangle}{N} - \frac{\langle \sin\phi \rangle^2}{N} \right) = \frac{1}{N-1} \sum \left(\langle \sin^2\phi_i \rangle - \langle \sin\phi \rangle^2 \right) . \tag{4.27}$$

In the above formulation, the beam polarization and the factor of 2 have been omitted for clarity, and must be included.

The formalism of D. Besset *et al.* [84], can also be used, where a set of estimators and the associated statistical uncertainties are investigated for extracting asymmetries using the method of moments. Three different approaches are used to define the variance in the estimators, a maximum likelihood, a Fourier, and a weighted sums method. All three methods reduce to the same value when the asymmetry is zero, but have slightly different dependences with respect to the asymmetry. The maximum likelihood variance of Ref. [84] was used in the single photon analysis for a consistency check of Eq. 4.27 and is given by:

$$\delta\langle \sin\phi \rangle^2 = \frac{2}{N} \left(1 - \frac{3}{4} \langle \sin\phi \rangle \right) . \tag{4.28}$$

Both calculations of the statistical uncertainty are consistent. The maximum likelihood method yields a slightly larger uncertainty and therefore was used in this analysis for a more conservative estimator of the statistical uncertainty. There are 4015 selected events for the single photon analysis in the exclusive region of $-1.5 < M_x < 1.7$ GeV, resulting in a statistical uncertainty of 0.0422 for the asymmetry.

4.7.2 Systematic Corrections and Uncertainties

The limited precision of the HERMES detector can give rise to systematic uncertainties in the asymmetry measurement, which need to be defined in order to evaluate the precision of the measurement. The systematic uncertainties can arise from several sources including the beam polarization measurement, the amount of background events in the exclusive region, kinematic constraints, and detector effects. The kinematic constraints which may affect the asymmetry include the positron vertex constraint, the opening angle constraints, and the choice of the exclusive region between -1.5 and 1.7 GeV. The detector effects consist of the limited acceptance, and uncertainties in the azimuthal angle ϕ due to external bremsstrahlung and finite detector resolution, as well as detector inefficiencies.

4.7.2.1 Beam Polarization

The uncertainty in the beam polarization has been estimated from the polarimeter group to be 3.8% of the measured value [85,86]. The uncertainty is dominated by the uncertainty in the calibration obtained from the polarization rise-time curves. The average beam polarization for the 96/97 dataset is $\sim 0.53 \pm 0.02$, which contributes a systematic uncertainty of 0.02 to the single spin asymmetry.

4.7.2.2 Contamination From Neutral Particle Decay

The single photon production in the non-exclusive (high missing mass) region is observed from the MC simulation to be primarily a result of the decay of π^0 mesons, where only one decay photon is detected. The single photons may also arise from other neutral particle decay, but are greatly suppressed ($< 1\%$) at the kinematics of HERMES compared to the contribution from π^0 decay, and are therefore neglected. One of the decay photons from the π^0 may not be detected and the event selected in the single photon analysis for several reasons. First, the granularity of the calorimeter is finite, as the face of a calorimeter block is 9×9 cm^2. As mentioned in Sec. 4.1.2, two decay photons which are separated by less than ~ 10 cm at the calorimeter face can not be distinguished as two distinct photons and therefore appear as a single photon. There is not a hard cutoff for the separation distance, as the algorithm considers the number of calorimeter blocks involved along with their respective energies and decides if there are one or two clusters. However, at a larger separation distance, the algorithm can distinguish two clusters with high efficiency, and these events are not considered part of the single photon candidates. In addition, if one decay photon of a π^0 meson has an energy less than the calorimeter threshold of 0.8 GeV, the photon will not be reconstructed as an independent cluster and assumed to be inherent noise from the calorimeter PMT's. This type of decay photon may, however, be associated with another cluster if the (low energy) photon is incident on one of the nine cluster blocks. Finally, one decay photon could be outside the physical acceptance of the spectrometer. These limits of the spectrometer allow for a large contribution from π^0 decay photons in the high missing mass region of the single photon analysis. In the exclusive region, the contribution from the π^0 mesons is reduced due to the energy conservation constraint for exclusive processes, since

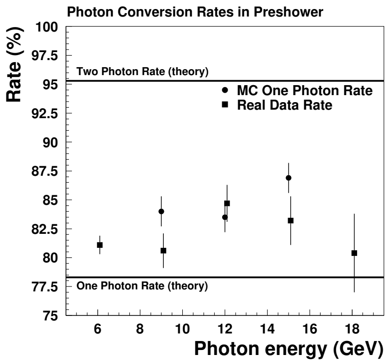

Figure 4.34: The response rate (percentage) of the preshower detector for the exclusive ($0.4 < M_x <$ 1.4 GeV) region of the single photon production. The squares indicate the experimental data, while the circles represent the MC simulation. The theoretical limits for the conversion process in a 2-radiation length material for single and double photons are also shown.

the detected decay photon must contain the majority of the π^0 momentum or the event could not have a reconstructed missing mass in the exclusive region.

The observed photons in the exclusive region are largely explained to be from the BH process, calculated using a MC simulation. There may be contamination from the decay of π^0 mesons, however. The amount of possible contamination was estimated by several methods. The response of the preshower detector can be used to estimate the ratio of the rate of one photon and two (close) photons, and so can be used as a check of the contamination arising from two decay photons being reconstructed as a single photon. The preshower detector consists of a 11 mm thick lead sheet which corresponds to two radiation lengths. The probability that a traversing photon produces a electron-positron pair, and starts the showering process is $\sim 78\%$. However, if there are two photons close together, which mimic one photon in the calorimeter, the probability that *at least* one photon starts to shower is $1 - (1 - 0.78)^2 \approx 96\%$. The actual rate also depends on the efficiency of the preshower detector and background noise and so was modeled using a simple MC simulation. The MC simulation used a single generated photon of three different initial energies (9, 12, and 15 GeV) as input to the HMC program. The experimental data are in fair agreement with the single photon MC simulation (within the statistical uncertainties), indicating the contamination from two close photons in the exclusive region is marginal (see Fig. 4.34). A simple calculation yields a maximum estimate of 5% possible contamination from two (close) photons of π^0 meson decay which are reconstructed as a single cluster in the exclusive region of $0.4 < M_x < 1.4$ GeV.

The preshower check however, will only give an estimate of the contamination from two photons which are minimally separated, and therefore is a valid check for only one of the several ways a photon from a π^0 decay might be selected in the single photon analysis. To estimate the total contamination from π^0 decay, the HERMES MC simulation was used. As the DIS generator used in the HERMES Monte Carlo simulation does not contain exclusive processes, a combination of the two generators (exclusive photon and DIS) were used.

The contamination from the decay photons of non-exclusive π^0 mesons which appears in the exclusive missing mass region in the single photon analysis was estimated using the MC simulation with the DIS generator. The BH process is the dominant single photon production process in the exclusive region from -1.5 to 1.7 GeV, however, the simulation indicates that $\sim$ 6% of the photons arise from a (DIS produced) π^0 meson decay. The simulation showed negligible contamination from other production mechanisms but does not account for exclusive π^0 mesons, which could also contribute.

The calculation of the amount of exclusive π^0 proceeded in two steps. First, the ratio of the number of detected single photons to double photons from exclusive π^0 decay was estimated. Then this ratio was multiplied by an estimate of the number of exclusive π^0 mesons detected in the 1996 and 1997 data sets, resulting an estimate of the number of single photons arising from exclusive π^0 production. This two step process included a MC simulation and analysis of real data.

The number of exclusive π^0 mesons which might be reconstructed as single photon events was estimated with an exclusive π^0 MC generator and the HMC program. The exclusive π^0 was generated uniformly in the kinematic variables Q^2, ν, and t, and weighted with a simple $1/Q^6$ weighting. The exclusive π^0 MC data were analyzed for both the "single photon" and "double photon" events, yielding a 12.5% single to double photon detection ratio for the missing mass region of -1.5 to 1.7 GeV.

Having the ratio of single to double photons, an estimate of the number of exclusive π^0 mesons detected in the 96/97 experimental dataset was obtained from the ratio of exclusive to non-exclusive π^+ mesons in the π^+ analysis [87], which amounts to $\sim$ 20% in the missing mass region of -1.5 to 1.7 GeV. This assumes that π^+ and π^0 mesons have the same ratio of exclusive to non-exclusive production. In fact, the exclusive π^+ cross section is enhanced by the π^+ pole which should yield an overestimate of the ratio (20%) of exclusive to non-exclusive π^0 production. However, to be conservative, a ratio of 20% was used for the exclusive to non-exclusive production for the π^0 meson.

The 12.5% (single/double photon) ratio was used in combination with the 20% (exclusive/non-exclusive π^0) ratio, resulting in an estimated 2.5% of the "single photon" π^0 events in the exclusive missing mass region arising from exclusive π^0 mesons. Combining the estimates for the exclusive and non-exclusive π^0 mesons in the exclusive missing mass region of the single photon analysis results in a contribution of 8.5%.

Although the π^0 meson single spin asymmetry has been shown to have azimuthal dependence [88], the photons from the decay of π^0 mesons which are reconstructed as single photon events should have little azimuthal angle dependence since only one of the decay photons is detected. However, to be reconstructed in the exclusive region, the single decay photon must carry a majority of the π^0 momentum, and so may retain some residual azimuthal dependence. The contribution to the single spin asymmetry from the decay photons of π^0 mesons in the exclusive region was estimated by performing a single beam-spin analysis for the π^0 meson production. This two photon analysis was performed in a similar manner as the single photon analysis, with the added constraint on the π^0 invariant mass of 0.115 to 0.150 GeV, and resulted in an estimate of $\approx -0.15 \pm 0.12$ for the π^0 single beam-spin asymmetry in the missing mass region of -1.5 to 1.7 GeV. The single spin π^0 asymmetry extracted from experimental data contains exclusive as well as non-exclusive production π^0 production. Combining the π^0 asymmetry estimate with the 8.5% contamination can give an indication of the uncertainty in the single spin asymmetry arising from the π^0 meson

$$A_{meas} = 0.915 A_{int} + 0.085 A_{\pi^0} \,, \tag{4.29}$$

where A_i is the measured (meas) asymmetry arising from the actual BH-DVCS interference (int) and the contribution from the decay of the π^0 meson. This is assuming the exclusive and non-exclusive π^0 mesons have the same asymmetry, which may not be true. Varying the π^0 asymmetry from -0.02 to -0.27 results in a maximum variation of the asymmetry of -0.0188 at the minimal π^0 asymmetry estimate of -0.02. A value of 0.019 is therefore assigned the systematic uncertainty of the single spin asymmetry arising from the decay photons of π^0 meson in the missing mass region of -1.5 to 1.7 GeV.

4.7.2.3 Contamination From Associated Exclusive Production

Another source of contamination in the exclusive region may be the associated DVCS and BH processes, where the interaction proceeds as $\gamma^* p \ \rightarrow \ \gamma \Delta^+$. The production of the Δ^+ can not be distinguished from the truly exclusive process with the HERMES spectrometer, as the difference in the Δ^+ and proton masses is $1.232 - 0.938 = 0.294$ GeV, and the resolution of the detector ~ 0.77 GeV. It has been argued by Frankfurt *et al.* [89], that the contributions may not significantly affect the single spin asymmetry. The BH process of $N \rightarrow \Delta$ is suppressed compared to the $N \rightarrow N$ process at low values of the momentum transfer t as the former cross section has a simple t^1 dependence, while the latter behave as $1/t$. The DVCS process of $N \rightarrow \Delta$, however, has been argued in the quark soliton model to be on the same order as the $N \rightarrow N$ DVCS process. The interference term of the associated BH and DVCS should be suppressed for the kinematic range of this analysis as compared to the BH-DVCS interference term of $\gamma^* p \rightarrow \gamma p$, since the BH cross-section is roughly an order of magnitude larger than the DVCS cross section. Assuming the DVCS and associated DVCS amplitudes are equal, a rough estimate of the contribution can be made using the t dependence of the BH and associated BH processes. The average value of t for the single photon production in the exclusive region of -1.5 to 1.7 GeV is -0.25 GeV^2, therefore, the contribution to the measured asymmetry from the associated process should be roughly $\frac{t}{1/t} = t^2 = 0.0625$ or $1/16$. Assuming equal asymmetries, the associated processes would contribute ~ -0.014 to the single spin asymmetry of -0.23. Accordingly, a systematic uncertainty from the possible associated process ($\gamma^* p \rightarrow \gamma \Delta^+$) is estimated as 0.014.

4.7.2.4 External Bremsstrahlung and Detector Effects

The finite resolution of the HERMES detector may result in a variance or smearing of the reconstructed kinematic variables in relation to the true values. A variance may also arise if the positron interacts with the detector material and emits an external (not from the target interaction) bremsstrahlung photon. Photons produced from bremsstrahlung in the target interaction region (internal bremsstrahlung) constitute the BH process and are part of the observed signal. The azimuthal angle ϕ is the only variable directly used in the construction of the single spin asymmetry, and a variance in ϕ may lead to a shift in the asymmetry value. Smearing due to the finite resolution of the detector tends to flatten out any structure in the azimuthal distribution, reducing the amplitude of the asymmetry. External bremsstrahlung tends to shift the reconstructed virtual photon closer to the beam line as the scattered positron is reconstructed with less energy. This in turn causes a shift of events to larger (absolute) values of ϕ. Since the event distribution is peaked at $\phi = 0$, external bremsstrahlung tends to flatten out the distribution. Therefore, both detector smearing and external bremsstrahlung effects tend to smear the central peak to larger absolute values of the azimuthal angle.

The effects of external bremsstrahlung and detector smearing was studied using a MC simulation. Events were generated using the standard DIS generator, tracked through the simulated detector with the Monte Carlo program (HMC) and reconstructed. Events which are reconstructed in the detector (accepted events) are used to compare the generated and reconstructed variables. The effect of the external bremsstrahlung and detector effects can be seen in Fig. 4.35, where the azimuthal distribution of the MC simulated accepted and reconstructed events is shown. The events tend to shift from the peak at zero radians in ϕ to larger (absolute) values of the azimuthal angle as expected.

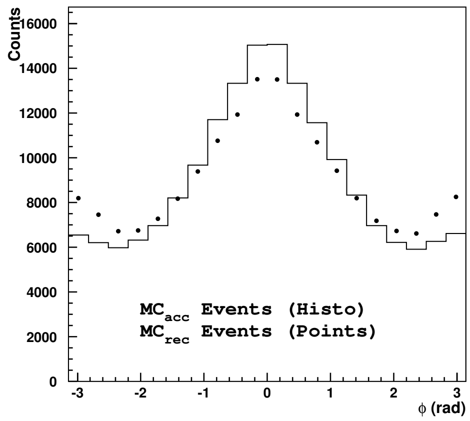

Figure 4.35: The azimuthal distribution of the accepted and reconstructed MC events.

The MC simulation does not contain the same $\sin\phi$ components observed in the experimental data therefore an additional weight was applied to the MC simulation:

$$1 + B\sin\phi\,.$$

The difference in the generated (gen) and reconstructed (rec) azimuthal distributions was then used to estimate the effect on the experimental asymmetry.

$$\begin{aligned}
\delta B &= B_{gen} - B_{rec} && (4.30)\\
&= 2\langle\sin\phi_{gen}\rangle - 2\langle\sin\phi_{rec}\rangle && (4.31)\\
&= \frac{\sum_{i=1}^{N}\sin\phi^i_{gen}(1+B\sin\phi^i_{gen})w_i - \sin\phi^i_{rec}(1+B\sin\phi^i_{rec})w_i}{\sum_{i=1}^{N} w_i}\,. && (4.32)
\end{aligned}$$

The sum is over the number (N) of MC events labeled by i, with the original MC weight denoted with w_i. For the exclusive region of $-1.5 - 1.7$ GeV, the experimentally measured single spin asymmetry value of -0.23 is used for the B parameter. The difference in the reconstructed and generated asymmetry is -0.00187, leading to an effect of $\sim 0.8\%$ on the asymmetry value. The external bremsstrahlung and detector effects therefore, have a small effect in comparison to the statistical accuracy of the asymmetry (± 0.04) and are included in the acceptance correction.

4.7.2.5 Acceptance Corrections and Uncertainties

Since the HERMES spectrometer consists of a top and bottom rectangular detectors, the acceptance is not spherically uniform, which may affect the measured asymmetry. A simple two box

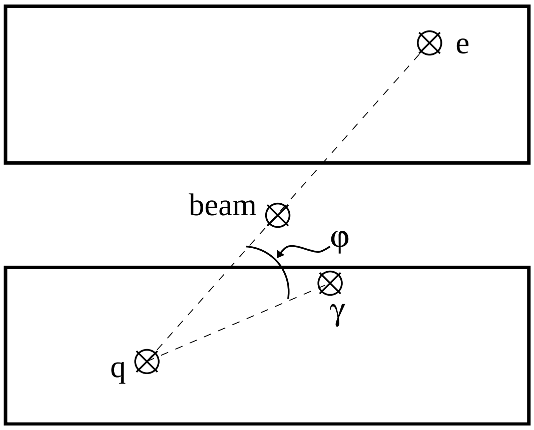

Figure 4.36: A diagram illustrating the acceptance of the HERMES spectrometer.

diagram representing the HERMES top and bottom detectors is shown in Fig. 4.36. The projected vectors of the incoming beam, the scattered positron (e), the virtual photon (q) and the produced real photon (γ) are represented with the $\otimes$ symbol. Undetected photons scattered into the gap between the two halves will have azimuthal ϕ angles near zero. Photons which are scattered outside the the two detector halves will have values of ϕ near $\pm\pi$ (rad). This simple geometric argument implies that the acceptance has a predominant $\cos\phi$ dependence. This acceptance effect should, in principle, cancel out in an asymmetry of the beam spin, as long as the acceptance is constant over time and the luminosity in both beam states is equal. However, there is a non-trivial complication which arises from convolution of the acceptance and cross section. The measured cross section is composed of two contributions, one from the true cross section and another contribution from the acceptance:

$$\frac{dN}{d\phi} = \frac{d(\sigma L)}{d\phi} \times \epsilon(\phi)\,, \tag{4.33}$$

with L representing the measured luminosity, and $\epsilon(\phi)$ the acceptance function, assumed here to be only a function of the azimuthal angle ϕ. The true cross section can be expressed in a Fourier series, hence it is convenient to expand the acceptance function in a Fourier series also, rewriting the measured cross section as a product of the two:

$$\begin{aligned} \frac{dN}{d\phi} &= \frac{\sigma L}{2\pi}[1 + \sum_m (a_m \cos m\phi + b_m \sin m\phi)] \\ &\times \frac{\int \epsilon(\phi) d\phi}{2\pi}[1 + \sum_n (A_n \cos n\phi + B_n \sin n\phi)]\,, \end{aligned} \tag{4.34}$$

where a_m and b_m are the cross section coefficients and A_n and B_n are the acceptance coefficients. The multiplication of the two Fourier series results in a new single Fourier series, where the coefficients are complicated expressions of the original coefficients (see Appendix A). The new series is the experimentally measured cross section which can be represented as:

$$\frac{dN}{d\phi} = \frac{N}{2\pi}[1 + \sum_m (\alpha_m \cos m\phi + \beta_m \sin m\phi)] , \tag{4.35}$$

where an explicit example of the β_1 coefficient of the $\sin\phi$ term is:

$$\beta_1 = N_F \left(b_1 + B_1 + \frac{1}{2} \sum_n (A_n b_{n+1} - b_n A_{n+1} - B_n a_{n+1} + a_n B_{n+1}) \right) . \tag{4.36}$$

with N_F representing a normalization factor which arises from the multiplication of the two Fourier series (see Appendix A) having the value of:

$$N_F = \frac{1}{1 + \frac{1}{2}\sum_n (A_n a_n + B_n b_n)} . \tag{4.37}$$

Since the acceptance function has a predominant $\cos\phi$ dependence, the largest contribution to the measured moment from the acceptance should be the value of $A_1 b_2$, where the $\sin 2\phi$ moment of the cross section couples to the $\cos\phi$ moment of the acceptance. Eq. 4.36 can also be written in matrix form:

$$\beta_m = N_F \sum_n M_{mn} b_n , \tag{4.38}$$

where M_{mn} is a matrix element composed of the acceptance values. The acceptance corrected moments can be obtained by inverting the matrix equation:

$$b_m = \frac{1}{N_F} \sum_n M^{-1}_{mn} \beta_n . \tag{4.39}$$

The statistical uncertainty of the acceptance corrected moments is calculated using experimentally measured moments and the (MC determined) acceptance matrix elements:

$$\delta(b_m) = \frac{1}{N_F} \sum_n \left[M^{-1}_{mn} \delta(\beta_n) + \delta(M^{-1}_{mn}) \beta_n \right] . \tag{4.40}$$

The uncertainty is difficult to calculate in this form due to the variance in the inverted matrix elements $\delta(M^{-1}_{mn})$, which is unknown, and is therefore expanded into a more useful form. The inverse of a matrix is related to its cofactor and determinant:

$$a^{-1}_{ij} = \frac{C_{ji}}{|a|} , \tag{4.41}$$

where C_{ji} is $(-1)^{j+i}$ times the cofactor of the matrix element a_{ij}. The relationship is used to expand the statistical uncertainty (Eq. 4.40) as:

$$\delta b_m = \frac{1}{N_F} \sum_n \left[M^{-1}_{mn} \delta\beta_n + \beta_n \left(\frac{|\delta M|}{|M|} \delta M^{-1}_{mn} - M^{-1}_{mn} \left[\sum_{k,l} \left(M^{-1}_{lk} \delta M_{kl} \right)^2 \right]^{\frac{1}{2}} \right) \right] , \tag{4.42}$$

where δM is the matrix composed of the uncertainties in the M elements.

The variance of Eq. 4.42 is squared yielding squared terms as well as covariant terms. For this calculation, the uncertainties in the acceptance matrix elements (from MC acceptance coefficients) and the statistical uncertainties in the measured moments (from experimental data) are uncorrelated. However, the acceptance matrix is symmetric, and furthermore, several elements in the matrix are composed of the same acceptance coefficient. These covariances, of maximum correlation value (+1), are included in the statistical uncertainty calculation.

In order to ascertain the coefficients of the HERMES acceptance function, a MC simulation was used. The MC simulated data were produced using the exclusive photon generator described in Sec 4.3 for the exclusive region of -1.5 to 1.7 GeV. The BH process has a large inherent $\cos\phi$ dependence, therefore a weight was assigned to the event by using the DVCS cross section calculation in the parameterization model of Ref. [31]. Only the DVCS cross section was used as it has a relatively small $\cos\phi$ dependence in the model. This $\cos\phi$ dependence is also relatively constant in the parameterization model with an average value of 0.06 ± 0.03 over the HERMES kinematic range, and was taken into account in the extraction of the acceptance coefficients. All MC acceptance coefficients were derived from the reconstructed variables, and so contain the simulated detector smearing and external bremsstrahlung. Using the reconstructed variable allows a correction of the acceptance, detector smearing, and external bremsstrahlung effects in a single calculation. The acceptance coefficients of the azimuthal dependence were extracted from the MC simulation:

$$A^{\cos_m \phi} = \frac{2}{N} \sum_i^N \frac{\cos(m\phi_i)}{(1 + 0.06 \cos\phi_i)} , \tag{4.43}$$

$$A^{\sin_m \phi} = \frac{2}{N} \sum_i^N \frac{\sin(m\phi_i)}{(1 + 0.06 \cos\phi_i)} . \tag{4.44}$$

The acceptance coefficients were also extracted using a varied range (0.03 to 0.09) of the DVCS $\cos\phi$ amplitudes, which showed negligible variation to the acceptance correction value. The first four acceptance coefficients are shown in Table 4.1. The value of the $\cos\phi$ coefficient is non-zero and the higher $\cos(m\phi)$ and the $\sin(m\phi)$ coefficients of the MC data (mostly) consistent with zero as expected from the simple geometric argument. The acceptance coefficients are assumed to have only ϕ dependence, although most likely they have other kinematic dependences. The effect of other

$A^{\cos\phi}$	$A^{\cos 2\phi}$	$A^{\cos 3\phi}$	$A^{\cos 4\phi}$
-0.4320 $\pm$ 0.04	0.0231 $\pm$ 0.04	0.0379 $\pm$ 0.04	-0.0519 $\pm$ 0.04

$A^{\sin\phi}$	$A^{\sin 2\phi}$	$A^{\sin 3\phi}$	$A^{\sin 4\phi}$
0.0214 $\pm$ 0.04	-0.0593 $\pm$ 0.04	0.0426 $\pm$ 0.04	0.0383 $\pm$ 0.04

Table 4.1: The MC simulated acceptance coefficients for the exclusive region of -1.5 to 1.7 GeV.

kinematic dependences should be minimal, as the acceptance coefficients and the measured moments are both formed from data summed over all kinematic quantities.

The acceptance corrected $\sin\phi$ moment was then calculated using the measured moments, the acceptance coefficients, and a matrix inversion routine. The acceptance correction for the $\sin\phi$ moment reduces the magnitude of the asymmetry by 0.0097.

As a cross-check of the above acceptance correction method, the data sample was also acceptance corrected on an event by event basis using the same MC simulated acceptance coefficients:

$$b_1^{acc} = \frac{2}{N}\sum_i^N \frac{\sin\phi_i}{N_f[1+\sum_n(A_n\cos n\phi + B_n\sin n\phi)]}\,. \tag{4.45}$$

When the acceptance is corrected on an event by event basis, not only ϕ, but also other kinematic dependences of the acceptance coefficients probably should to be taken into account as each individual event is being acceptance corrected before summing over the kinematic quantities. Also, the statistical uncertainty is not easily calculated in this method, and has been omitted. Therefore, this method is only used as a cross-check of the inversion method.

Another check of the acceptance can be done by forming an asymmetry as a function of ϕ:

$$A(\phi) = \frac{\sum([N^+(\phi) - N^-(\phi)]\cdot\epsilon(\phi))}{\sum([N^+(\phi) + N^-(\phi)]\cdot\epsilon(\phi))}\,, \tag{4.46}$$

where the $N^{\pm}(\phi)$ are the number of luminosity weighted events in each helicity state. The acceptance function can be factored out of the sum if the acceptance is constant over the ϕ range and will cancel in the numerator and denominator. Although the acceptance does change for the number of ϕ bins used in the single photon analysis, and in principle can not be factored from the sum, it is assumed that the major acceptance effects cancel. Another concern is the uncertainty in the luminosity for the luminosity balancing of the helicity states which contributes to the overall uncertainty of the fit method. Finally, the denominator in Eq. 4.46 has some ϕ dependence which may result in an incorrect asymmetry from the fit method. For these reasons, the fit asymmetry is only used as a cross-check of

M_x (GeV)	b_1	b_1^{acc}	b_1^{fit}
(-1.5) - 1.7	-0.2210 $\pm$ 0.0409	-0.2212	-0.2639 $\pm$ 0.0433

Table 4.2: Acceptance corrected $\sin\phi$ moments from three different extraction methods.

the magnitude of the acceptance correction, and is not considered a valid estimate of the acceptance correction in this analysis.

The acceptance corrected values obtained from all three methods are displayed in Table 4.2. The inversion method (b_1) and the event-by-event method (b_1^{acc}) yield similar acceptance corrected asymmetry moments. The fit method (b_1^{fit}) results in an asymmetry, which although consistent within the statistical precision of the measurement, is different from the other methods. However, all three methods illustrate the acceptance correction is relatively small. The fit method was used to estimate the order of magnitude of the acceptance correction, therefore only the inversion and event-by-event method were considered in estimating the value of the acceptance correction. A value of $0.0097 \approx 0.01$ is used for the estimate of the acceptance correction of the single spin asymmetry in the exclusive region. Since the correction is not large for the measured asymmetry value of -0.23, the acceptance correction is not applied to the data, but instead added in the systematic uncertainty.

4.7.2.6 QED Radiative Corrections

The QED radiative correction are cross section corrections to electromagnetic interactions of order $\alpha_{em} \approx 1/137$ as discussed in Sec. 2.5.1. The QED radiative corrections to the BH and DVCS handbag diagrams have been studied in Ref. [54]. Some of the first order QED radiative corrections to the BH and DVCS processes are one-loop corrections, which include vertex, lepton self-energy, and vacuum polarization corrections (shown previously in Fig. 2.21). In the QED radiative calculation of Ref. [54] inherent ultraviolet (UV) divergences were removed using dimensional renormalization. The dimensional renormalization process leads to infrared (IR) divergences in the vertex corrections which can be cancelled at the cross section level by including soft-photon emission processes. These processes involve an emission of an (undetected) low energy photon as shown in Fig. 4.37 which can arise due to the limited resolution and acceptance of the detector. The diagrams for the initial (b1i-b3i) and final state (b1f-b3f) of the BH process are shown, along with the corresponding diagrams for the DVCS process (b4, b5). The radiative tail, which consists of the emission of a photon on the order of the lepton energy, was also calculated.

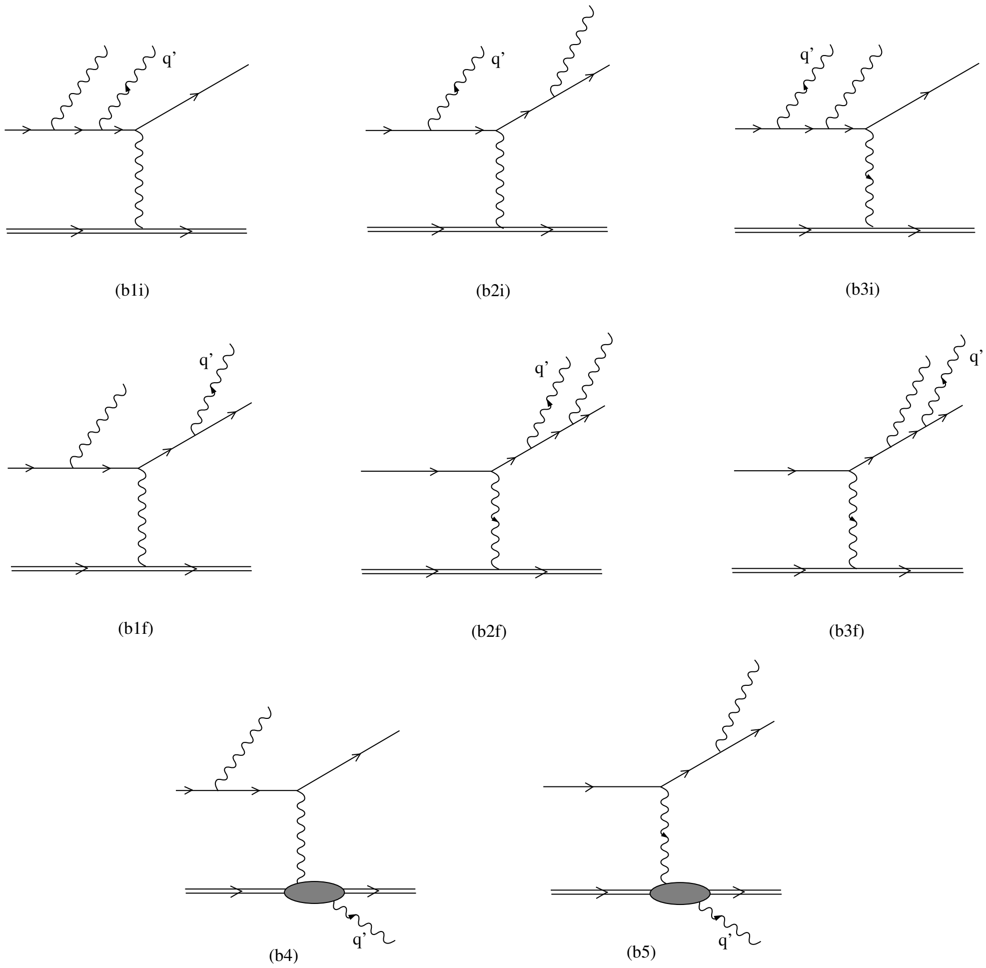

Figure 4.37: First order soft photon emission contributions to the $ep \to ep\gamma$ reaction.

The corrections to the cross section have been estimated for the BH and DVCS processes for kinematics relevant at the JLAB facility and are shown in Fig. 4.38. The kinematics used for this calculation are: Lepton Beam Energy = 6 GeV, $Q^2 = 2$ GeV^2, and $x_{Bj} = 0.3$. The corrections reduce the total (BH plus DVCS) cross section by $\approx 20\%$, and therefore can be quite significant for a cross section measurement. The same calculation was completed for the single beam-spin asymmetry, for the kinematics of JLAB, shown in Fig. 4.39. The radiative corrections have a small effect on the asymmetry, reducing the asymmetry by $\approx 5\%$.

The radiative corrections are inversely proportional to the beam energy and hence are smaller at HERMES kinematics than they are at JLAB kinematics. Therefore, the radiative corrections to the single spin asymmetry of the HERMES measurement should be marginal ($< 5\%$) compared to the present statistical accuracy. A systematic uncertainty of $0.05 \times -0.23 = 0.0115$ is estimated for the QED radiative effects, given the lack of a calculation at the HERMES kinematics.

4.7.2.7 Stability of Asymmetry

In addition to the above systematic checks, the asymmetry was investigated for stability with respect to changes in the kinematic constraints. These constraints include the positron vertex, the maximum and minimum missing mass, and the upper and lower opening angle constraints.

To decrease any contamination from interactions other than the gas target, a constraint was placed on the vertex position of the positron to be within ± 18 cm of the center of the target cell. To investigate the effect of the vertex position on the asymmetry, the asymmetry was formed for different minimum and maximum constraints (see Fig. 4.40 and 4.41). The asymmetry is quite stable against variations in the positron vertex constraint between $\pm(16 - 21)$ cm. Although this is a rather large variation (5 cm), the majority of the events originate from the center of the target (see Fig. 4.9), so the statistics are not significantly affected. The maximum asymmetry variation from this vertex study is used for the estimated systematic uncertainty of 0.0058 for the minimum constraint and 0.0088 for the maximum constraint.

The opening angle $\theta_{\gamma*\gamma}$ between the virtual and real photon was constrained with a lower and upper limit. The lower limit was implemented at 0.015 rad, to ensure minimal effect on the azimuthal angle calculation arising from the variance in the cluster position reconstruction. The upper limit was placed at 0.07 rad to have a more uniform azimuthal distribution for the exclusive region. The change in the asymmetry with respect to these opening angle constraints was investigated by varying each constraint. The results for the lower constraint show some small variance of the single spin asymmetry (see Fig. 4.42). The difference in the asymmetry values over the investigated lower constraints has a

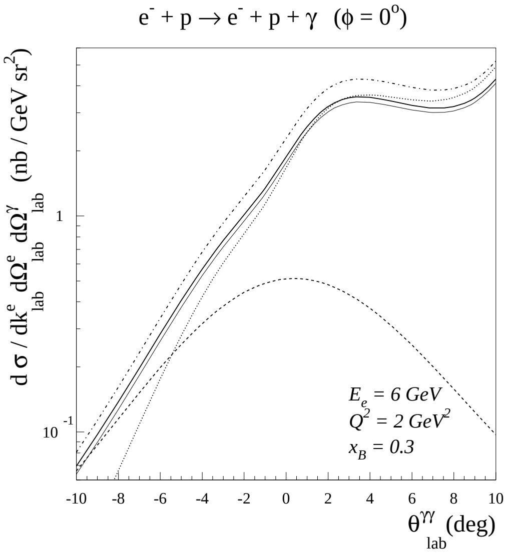

Figure 4.38: Differential $ep \to ep\gamma$ cross section in the lab frame for kinematics relevant at JLAB [54]. Dotted curve represents the BH process, dashed curve for the DVCS, dashed-dotted curve for the combined BH + DVCS, thin full curve for the BH + DVCS + virtual radiative corrections. The thick full curve represents the BH + DVCS + virtual and real radiative corrections, where the real radiative corrections are calculated with $\Delta E_s = 0.1$ GeV, which corresponds with a cut in the missing mass spectrum of M_{m1}^2 - $M_N^2 \simeq 0.21$ GeV^2.

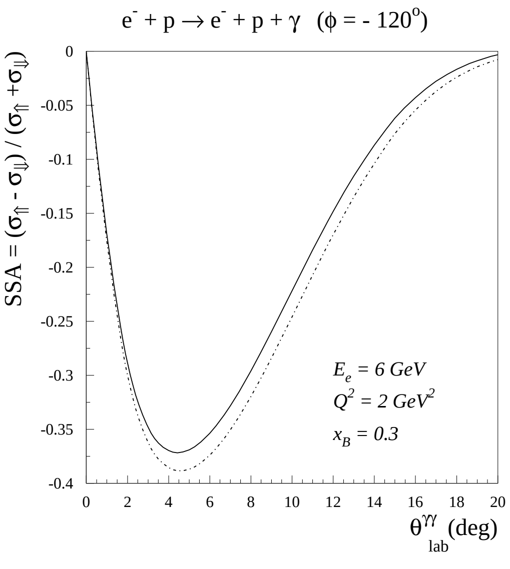

Figure 4.39: Electron single spin asymmetry (SSA) for the kinematics relevant at JLAB [54]. The dashed-dotted curve represents the BH + DVCS, and the full curve represents the BH + DVCS + radiative corrections.

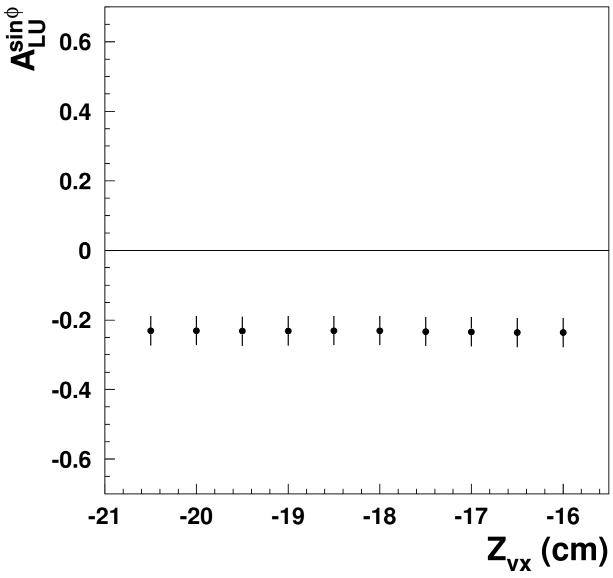

Figure 4.40: The single spin asymmetry for the exclusive region as a function of the minimum positron vertex constraint from -20.5 to -16 cm.

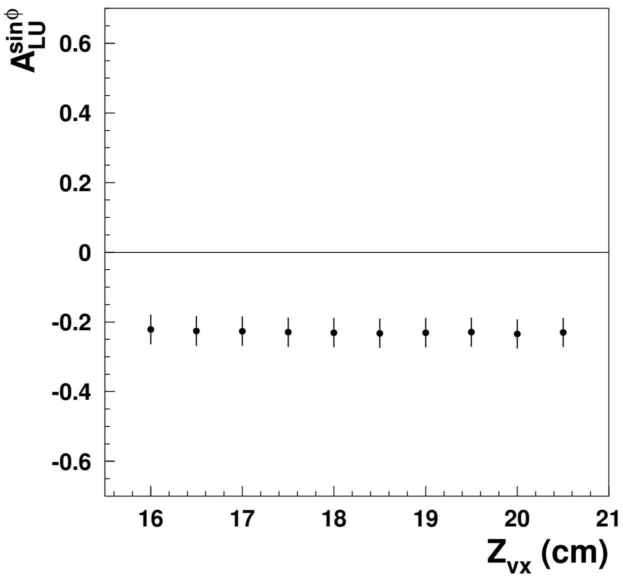

Figure 4.41: The single spin asymmetry for the exclusive region as a function of the maximum positron vertex constraint from 16 to 20.5 cm.

maximum of ≈ 0.05. The effect of the upper constraint is shown in Fig. 4.43 and is less dramatic than the lower opening angle constraint, having a maximum deviation of ≈ 0.03 over the investigated range.

The variance of the single spin asymmetry for the exclusive region as a function of the opening angle $\theta_{\gamma * \gamma}$ is most likely due to the changing of the ratio of the BH to DVCS process. The acceptance of the HERMES spectrometer only allows events with near zero azimuthal angle to be detected for large values of the opening angle, which are dominated by the BH process (in-plane angles). Therefore, the upper opening angle constraint reduces the amount of BH compared to the DVCS. The lower opening angle constraint also changes the BH-DVCS ratio, by removing a larger percentage of DVCS compared to BH events. The change in the asymmetry from the opening angle constraint is most likely due to physics and not a systematic uncertainty from the measurement precision. The systematic uncertainty associated with the opening angle constraint was therefore derived by using the values of the asymmetry obtained by small variations of the constraints. For the minimum opening angle study, the average deviation of the asymmetry using a lower constraint between 0.012 and 0.018 radian, yields an average uncertainty of 0.0205. An average asymmetry deviation with respect to variation of the opening angle was 0.0084 for with upper limits of 0.06 to 0.08 radian.

The exclusive region was defined by constraining the reconstructed missing mass to be between -1.5 GeV and 1.7 GeV. The lower bound was chosen to remove the few extraneous events which might have a large negative value of missing mass and is approximately 3 times the estimated missing mass resolution of 0.8 GeV. Since the actual value of the missing mass can be only 0.938 GeV or larger, the events with a reconstructed missing mass less than the proton mass due to the limited detector resolution should be enriched with exclusive events. The investigation of the lower missing mass constraint has a small effect producing a maximum asymmetry variance of 0.0033 (see Fig. 4.44).

The effect of the upper limit constraint on the single spin asymmetry was also investigated (see Fig. 4.45). The upper limit missing mass constraint was placed at 1.7 GeV which is a $\sim 1\ \sigma$ value of the missing mass resolution above the mass of the proton. The upper limit was chosen to include as many statistics as possible without introducing a large background contamination to the event sample. As the upper constraint is moved to higher values of the missing mass, more background from the non-exclusive processes is included in the data sample. The magnitude of the asymmetry appears to have the expected decrease with the increase of the upper missing mass constraint. Using a smaller variation of the constraint between 1.5 to 1.9 GeV, the average asymmetry deviation is ≈ 0.0258, which is assigned to the systematic uncertainty.

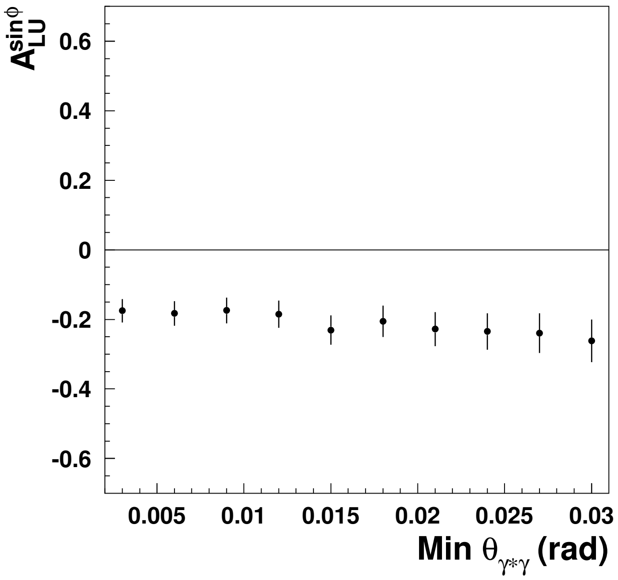

Figure 4.42: The single spin asymmetry for the exclusive region as a function of the minimum opening angle in the range of 0.003 to 0.03.

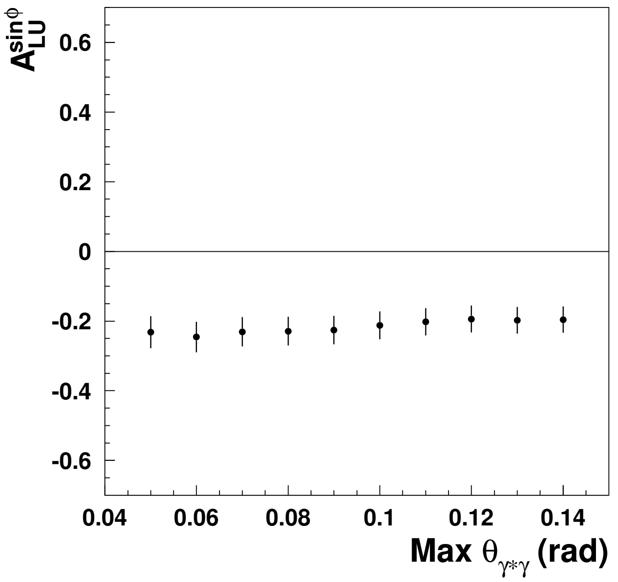

Figure 4.43: The single spin asymmetry for the exclusive region as a function of the maximum opening angle in the range of 0.05 to 0.014 rad.

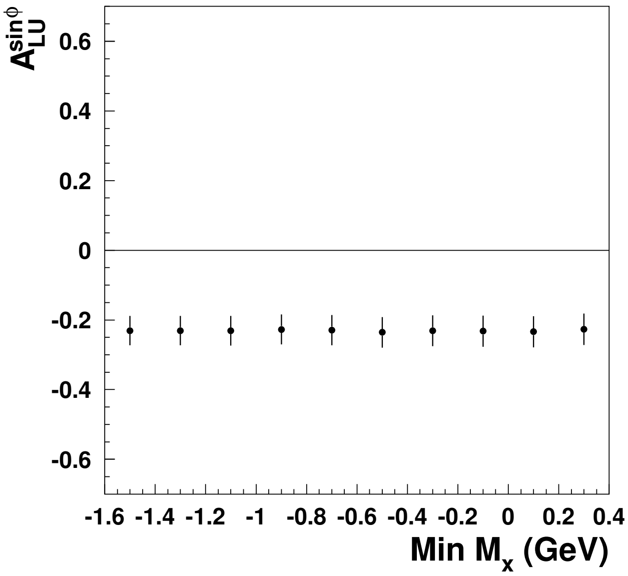

Figure 4.44: The single spin asymmetry for the exclusive region as a function of the maximum missing mass constraint in the range of -1.6 to 0.4 GeV.

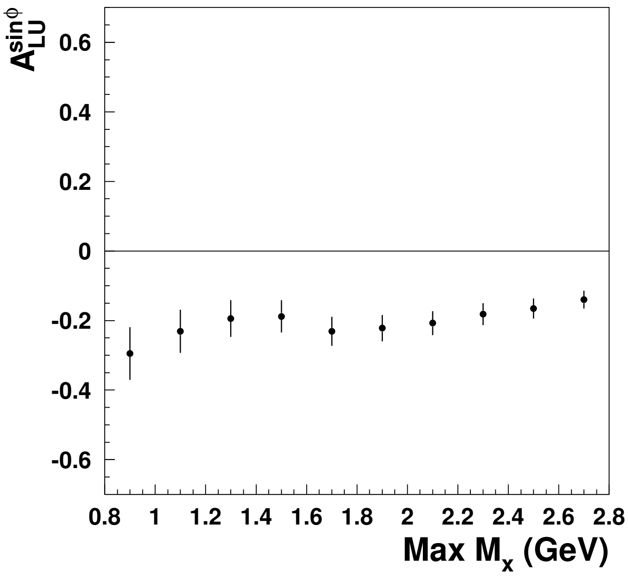

Figure 4.45: The single spin asymmetry for the exclusive region as a function of the maximum missing mass constraint in the range of 0.8 to 2.8 GeV.

Source of Uncertainty	
Beam Polarization	0.020
π^0 background	0.019
$p \to \Delta^+$ contribution	0.014
Acceptance, smearing and external bremsstrahlung	0.01
QED radiative effects	0.0115
Positron vertex minimum constraint	0.0058
Positron vertex maximum constraint	0.0088
$\theta_{\gamma * \gamma}$ minimum constraint	0.0205
$\theta_{\gamma * \gamma}$ maximum constraint	0.0085
M_x minimum constraint	0.0033
M_x maximum constraint	0.0258

Table 4.3: Absolute systematic uncertainties to the single spin asymmetry measurement.

4.7.2.8 Systematic Uncertainty Summary

The systematic uncertainty of the single spin asymmetry measurement has been investigated for the background contributions, detector effects, and the effects of constraints on the data. The estimated uncertainty contributions to the asymmetry value are summarized in Table 4.3. The largest the systematic uncertainty of the single spin asymmetry arises from the estimate of the background contributions. The uncertainty in the beam polarization also has a significant contribution. Finally, the constraints on the minimum opening angle and maximum missing mass have significant effects also.

There are several possible ways to combine the uncertainties into a single value. Assuming the systematic uncertainties are uncorrelated, combining all of the estimates quadratically results in a total systematic uncertainty of 0.05. Assuming maximum correlation (not very probable), the uncertainties can be added linearly, resulting in an uncertainty value of 0.15, which is the maximum possible uncertainty. As discussed before, the ratio of the DVCS to BH events is probably governed by the opening angle constraints. Also, the amount of background contamination in the event sample is mainly controlled by the missing mass constraint of the exclusive region. Neither of these considerations is strictly a systematic uncertainty, as the asymmetry variation with these constraints would remain even with a very precise measurement of the asymmetry (assuming the background processes remained constant). Therefore, neglecting the variances in the missing mass and opening angle should yield an estimate which is more reflective of the true systematic uncertainty. This results in a systematic uncertainty of 0.04 (0.09) for a quadratic (linear) sum. Assuming little correlation between the uncertainties, a value of 0.04 has been assigned to the systematic uncertainty associated with the single beam-spin asymmetry obtained in this analysis.

Chapter 5

Results

5.1 Single Spin Asymmetry

The single beam-spin asymmetry for the photon leptoproduction has been measured at the HERMES experiment from hydrogen data collected during 1996 and 1997. The single photon data, constrained by various kinematic and phase space considerations, amounted to 4015 events in the selected exclusive region. This region, as described in Sec. 4.2.4, constrained the reconstructed missing mass to be between -1.5 to 1.7 GeV where the non-physical region of negative missing mass arises from the finite resolution of the calorimeter. The values of the kinematic variables for the selected events ranged as follows:

$$1 < Q^2 \lesssim 10 \ \ \mathrm{GeV}^2 \,,$$
$$-2 \lesssim t \lesssim 0.5 \ \ \mathrm{GeV}^2 \,,$$
$$0.02 < x_{Bj} \lesssim 0.4 \,,$$

with average values of:

$$\begin{aligned} \langle Q^2 \rangle &= 2.6 \ \mathrm{GeV}^2 \,, \\ \langle t \rangle &= -0.25 \ \mathrm{GeV}^2 \,, \\ \langle x_{Bj} \rangle &= 0.11 \,. \end{aligned}$$

Here, the positive values of t (which are unphysical) arise from the limited detector resolution. The asymmetry value in the exclusive region was estimated using the method of moments to be -0.23 ± 0.04 (stat) ± 0.04 (syst).

5.2 Model Comparison

The single beam-spin asymmetry was compared to a DVCS-BH calculation using a parameterization [1] for the GPD's and the average kinematics for the HERMES measurement. The model for the GPDs included in the DVCS calculation were based on the MRST98 parton distribution functions [35], and included the D-term calculated in the soliton model (described in Sec. 2.3.1) needed to fulfill the polynomial conditions. The calculation contained the leading-twist description as well as the kinematic twist-3 contributions which were added using Wandzura-Wilczek type relations. The parameterization calculation maintained gauge invariance by an added heuristic term as described in (Sec. 2.3.1). The azimuthal distribution of the experimental data can be described by this parameterization, but the azimuthal distribution is more consistent with a simple $\sin\phi$ dependence (see Fig. 5.1). The leading-twist formalism predicts the simple $\sin\phi$ dependence, with a $\sin 2\phi$ behavior entering from twist-3 effects. The data suggest that the twist-3 contributions may be smaller than the contribution predicted in this parameterization calculation, but the precision of the measurement does not allow a definite conclusion.

For a more complete prediction including the effects of the detector, the exclusive MC simulation was used in combination with the parameterization model cross section calculation (see Fig. 5.2). The parameterization model for this simulated production included only the leading-twist contributions, the D-term, and the heuristic gauge restoring term. No twist-three contributions were included. For each MC generated event, a BH + DVCS cross section weight was calculated. The generated events were input into the HMC simulation program and the HRC reconstruction program, and an asymmetry extracted in the same manner as the experimental one. The MC simulated azimuthal distribution is consistent with a simple $\sin\phi$ leading-twist prediction, and provides a fair description of the experimental data. The experimental asymmetry appears to display a smaller amplitude of the $\sin\phi$ distribution. This discrepancy may be the result of dilution from underestimated background events, such as decay photons from π^0 mesons, or underestimated QED radiative corrections, or may be due to incorrect assumptions in the parameterization calculation.

Recently, the observation of a non-zero single spin asymmetry has been confirmed at the CLAS experiment at JLAB [90]. The single photon data were collected from a 4.25 GeV electron beam in 1999 with the detection of the scattered electron and recoiled proton. The background due to the π^0 meson was removed from the data sample using a fit technique. The resulting exclusive data are used to form the same asymmetry as at HERMES, which due to the opposite charge of the lepton beam, has a positive value. The value of the single spin asymmetry of 0.202 ± 0.028 is obtained via a fit of a two component Fourier $\sin\phi$ series. The data are shown in Fig. 5.3 and compared with several calculations of the model of Ref. [1]. Here, as in the HERMES measurement, the model calculation predicts a larger asymmetry than is observed.

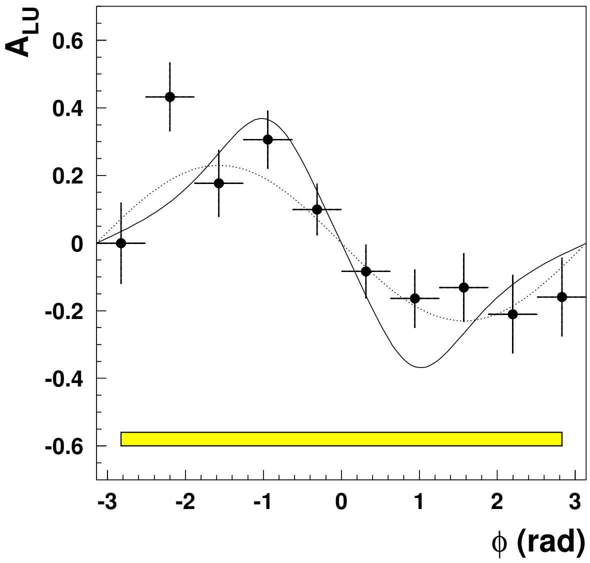

Figure 5.1: Azimuthal dependence of the single spin asymmetry. The data show a clear $\sin(\phi)$ -type dependence, as is illustrated by the dashed curve of amplitude -0.23 obtained by the method of moments. The solid curve represents a parameterization model calculation [1]. The error bars are statistical, and the error band represents the systematic uncertainty.

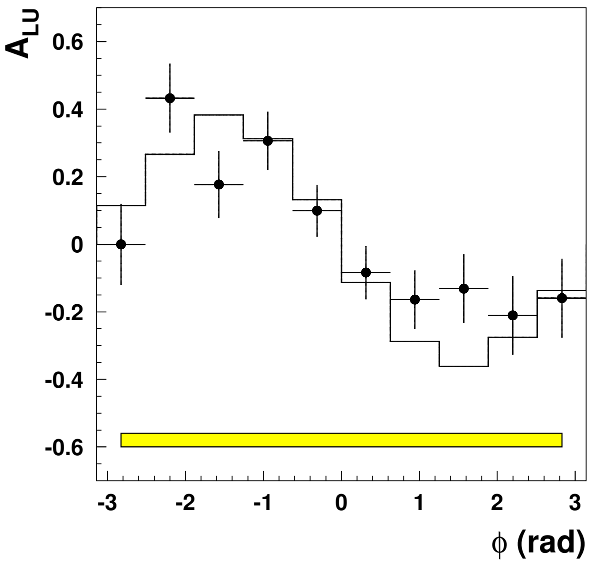

Figure 5.2: Azimuthal dependence of the single spin asymmetry. The histogram represents a MC simulation using the parameterization model calculation [1]. The error bars are statistical, and the error band represents the systematic uncertainty.

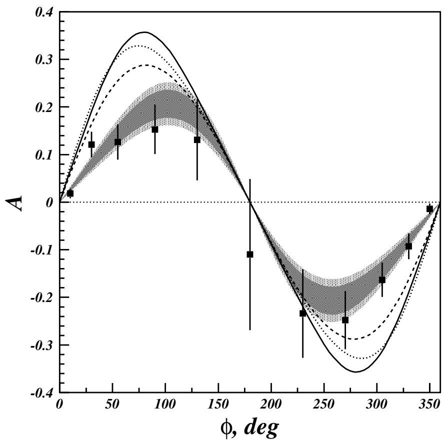

Figure 5.3: The single spin asymmetry as a function of ϕ from the CLAS experiment [90]. The dark shaded area represents the best fit function, while the curves represent model calculations of Ref. [1].

5.3 Kinematic Dependence of the Asymmetry

The kinematic dependences of the single spin asymmetry are interesting to investigate. In particular, the Q^2 dependence can be indicative of the type of the scattering regime. For the handbag diagram to be the dominant mechanism of the interaction, the scattering should be in the hard regime, that is, a vanishing of the Q^2 dependence as in DIS (except at low x_{Bj} values). The limited statistics of this single photon analysis in the selected exclusive region does not allow a precise determination of the kinematic dependences of the asymmetry. In addition to the limited statistics, the acceptance correction was calculated using integrated acceptance coefficients, and may not reflect the acceptance correction for different kinematic regions. Therefore, only a qualitative investigation of the kinematic dependences can be carried out. The single spin asymmetry was divided in five Q^2 bins having approximately the same statistics. The asymmetry does not exhibit much dependence on the asymmetry within the available statistical precision (see Fig. 5.4). This Q^2 independence is also seen in the MC simulation, although the magnitude of the predicted asymmetry is larger than the experimental one. The MC simulation assumes factorization (ie, no Q^2 dependence in the underlying parton distribution functions in this x_{Bj} region) and only includes the leading twist contributions. There is no indication that the experimental events from this analysis are *not* produced via hard scattering.

The asymmetry, as calculated, is a normalized difference in helicity states of the BH-DVCS cross sections, and therefore contain extra kinematic dependences. Following the formalism of Belitsky *et al.* in Ref. [47] the difference in the BH and DVCS cross sections (see Eq. def-SSA-SL in Sec. 2.4.1) can be written as:

$$d\sigma^{\uparrow} - d\sigma^{\downarrow} = -\frac{16(2-y)\sqrt{1-x}}{\sqrt{1-yx}\sqrt{-tQ^2}}\sqrt{1-\frac{t_{min}}{t}} \times \sin(\phi)\mathrm{Im}\left\{F_1\mathcal{H}_1 + \frac{x}{2-x}(F_1+F_2)\widetilde{\mathcal{H}}_1 - \frac{\Delta^2}{4M^2}F_2\mathcal{E}_1\right\}d\mathcal{M}. \tag{5.1}$$

The difference in the cross sections is normalized by a sum of the cross sections which is a combination of the squared BH and DVCS amplitudes, as well as the interference between the two. Since the BH process dominates at the kinematics of the HERMES experiment, the BH cross section:

$$d\sigma_{BH} = \frac{2(2-2y+y^2)}{(1-y)(-t)} \times\left\{4\frac{1-x}{x^2}\left(1-\frac{t_{\min}}{t}\right)F_1^2 + 2(F_1+F_2)^2 + \left(\frac{t}{t_{\min}}-1\right)F_2^2\right\}d\mathcal{M}\,, \tag{5.2}$$

can be used to represent the normalization term of the asymmetry. Neglecting the kinematic dependence of the form factors F_1 and F_2, the kinematic dependence of the asymmetry (K) can be approximated as:

$$K \approx \frac{16(2-y)\sqrt{1-x}}{\sqrt{1-yx}\sqrt{-tQ^2}}\sqrt{1-\frac{t_{min}}{t}} \times \frac{(1-y)(-t)}{2(2-2y+y^2)}\,. \tag{5.3}$$

A reduced asymmetry and statistical uncertainty was formed by dividing the asymmetry by K, and should more accurately reflect the actual kinematic dependences (see Fig. 5.5). Since the value of the the kinematic factor K is on the order of 10, the vertical axis on the reduced plots has been changed from $-0.5 \to 0.5$ to $-0.08 \to 0.08$ in order to illustrate the asymmetry behavior. The reduced asymmetry has more dependence on Q^2, with the magnitude of the asymmetry increasing for larger Q^2. This trend is also observed in the MC simulation, indicating that the reduced asymmetry should have a Q^2 dependence if factorization is valid. The data for the reduced asymmetry shows a better qualitative agreement to the MC simulation, which suggests the kinematic dependences in the simulation are somewhat different than in the experimental data. The kinematic dependence on t and x_{Bj} for the single spin asymmetry, as well as the respective reduced asymmetries has also been investigated. The dependence on the invariant momentum transfer t will be important in order to extrapolate the GPD functions $E(x, \xi, t)$ to the forward limit to obtain the angular momentum information, and also can be used to differentiate between GPD models. The t dependence is rather weak for the experimental asymmetry (see Figs. 5.6 and 5.7). The MC simulation does not predict much t dependence for the asymmetry, but does predict t dependence for the reduced asymmetry. The x_{Bj} dependence may help to constrain the different models of the generalized parton distributions, some of which have strong x_{Bj} dependences. The x_{Bj} dependence of the experimental asymmetry has some structure, although

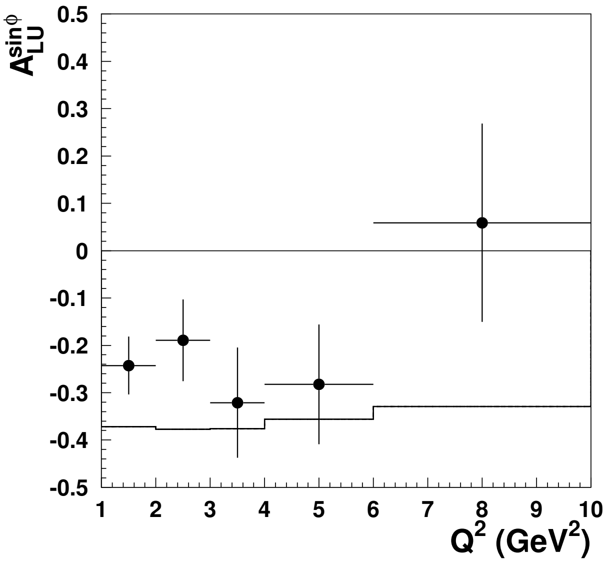

Figure 5.4: The single beam-spin asymmetry as a function of Q^2 for the exclusive region of -1.5 to 1.7 GeV. The horizontal error bars represent the bin width and the vertical error bars the statistical uncertainty. The histogram represents a MC simulation using the parameterization model calculation [1].

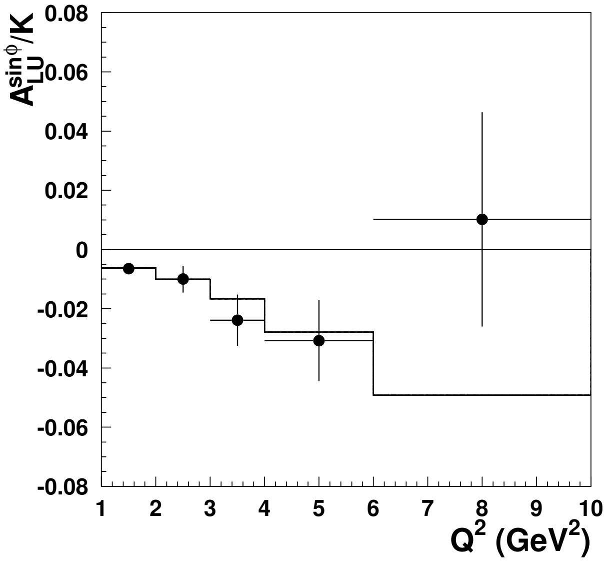

Figure 5.5: The reduced single beam-spin asymmetry as a function of Q^2 for the exclusive region of -1.5 to 1.7 GeV (see text for details). The horizontal error bars represent the bin width and the vertical error bars the statistical uncertainty. The histogram represents a MC simulation using the parameterization model calculation [1].

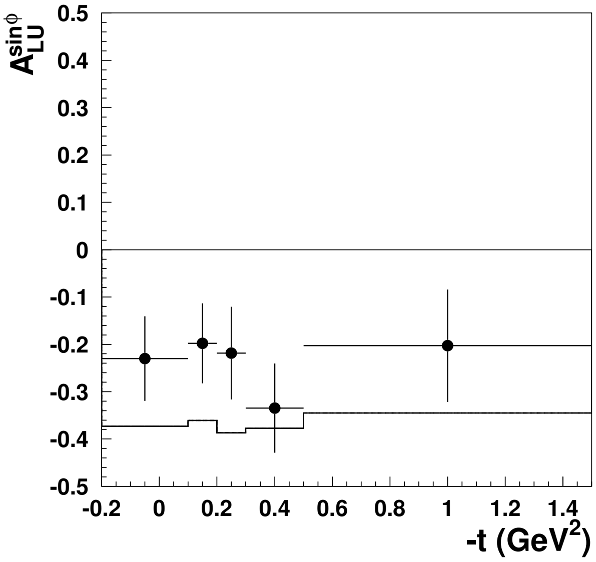

Figure 5.6: The single beam-spin asymmetry as a function of t for the exclusive region of -1.5 to 1.7 GeV. The horizontal error bars represent the bin width and the vertical error bars the statistical uncertainty. The histogram represents a MC simulation using the parameterization model calculation [1].

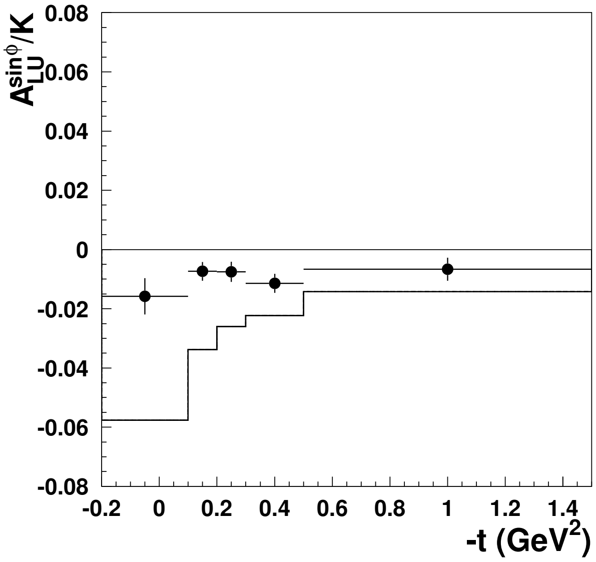

Figure 5.7: The reduced single beam-spin asymmetry as a function of t for the exclusive region of -1.5 to 1.7 GeV. The horizontal error bars represent the bin width and the vertical error bars the statistical uncertainty. The histogram represents a MC simulation using the parameterization model calculation [1].

not predicted by the MC simulation as shown in Fig. 5.8. The reduced asymmetry (see Fig. 5.9) appears to increase for larger values of x_{Bj} in both the experimental data and the MC simulation, and there appears qualitatively better agreement between the reduced asymmetries.

Although the dependence on the various kinematic variables will be useful to help define the GPDs, the kinematic dependences in this analysis are of a qualitative nature only due to the limited statistical precision. Some study is also required to determine any correlations between the kinematic variables arising from the limited acceptance of the spectrometer. In addition, the systematic uncertainty of the asymmetry as functions of the different kinematic variables has not been taken into account.

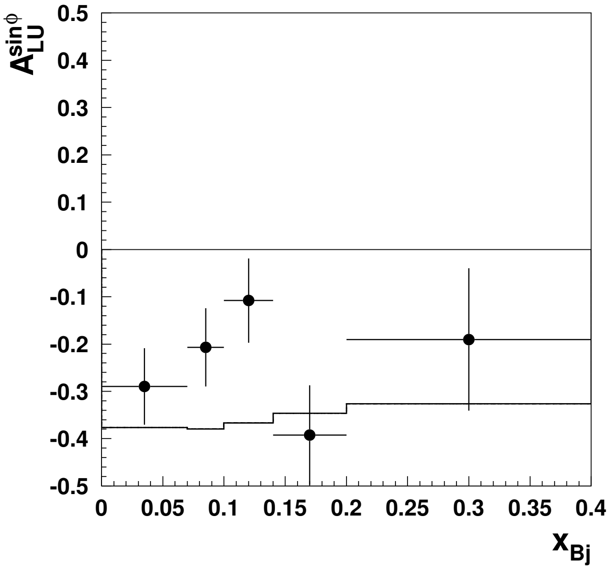

Figure 5.8: The single beam-spin asymmetry as a function of x_{Bj} for the exclusive region of -1.5 to 1.7 GeV. The horizontal error bars represent the bin width and the vertical error bars the statistical uncertainty. The histogram represents a MC simulation using the parameterization model calculation [1].

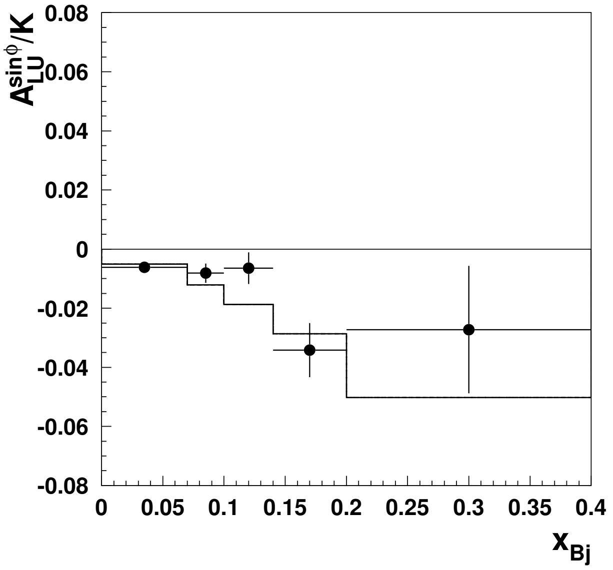

Figure 5.9: The reduced single beam-spin asymmetry as a function of x_{Bj} for the exclusive region of -1.5 to 1.7 GeV. The horizontal error bars represent the bin width and the vertical error bars the statistical uncertainty. The histogram represents a MC simulation using the parameterization model calculation [1].

Chapter 6

Summary, Conclusions, and Future Outlook

The first observation of a single beam-spin asymmetry associated with the interference of the Bethe-Heitler and the deeply virtual Compton scattering processes has been made at the HERMES experiment [96]. With more precise DVCS measurements and data from other exclusive processes, one can extract the generalized parton distributions, which should yield new information on the nucleon structure. In particular, the connection of the GPDs to the total angular momentum could increase the understanding of the spin composition of the nucleon.

With the recent theoretical factorization work, the generalized parton distributions can be used to describe the soft components of hard scattering off-forward virtual Compton-like scattering processes. At leading twist there are four independent GPDs differing from the parton distributions of DIS by having an extra degree of freedom which describes the momentum transfer to the nucleon final state. Since momentum transfer is involved, the struck or active quark has a change of momentum, and therefore the GPDs describe the correlations between quarks of different momentum. The GPDs also provide a link between elastic scattering and the parton distributions of DIS.

When the momentum transfer is large, the GPDs resemble meson distributions amplitudes. On the other hand, when the momentum transfer is zero, the GPDs collapse to the usual parton distribution functions. These two limits, along with symmetry considerations, greatly constrain the modeling of the GPDs. Several model calculations have been performed including the MIT bag and quark soliton model. These models, constructed at low scale, need to be evolved to the hard scattering region where factorization holds and a description in terms of the GPDs can be made. Evolution equations which are interpolations of the DGLAP and ERBL type equations have been investigated, but do not have simple solutions. A simple parameterization can be used to calculate the GPDs using the constraints and the measured parton distributions and elastic form factors. This parameterization allows a calculation of observables at the appropriate hard scattering scales through the use of the DGLAP evolution equations.

The simplest observable reaction which can be described in terms of the GPD formalism is the deeply virtual Compton scattering process. However, the DVCS process has the identical final state as the Bethe-Heitler process. In most present experiments, the BH process dominates over the DVCS process. In these regions an indirect extraction of the DVCS amplitude can be made by taking advantage of the interference term between the BH and DVCS processes. The appropriate observable to access the interference term is an asymmetry of the azimuthal distribution of the produced photon with respect to the spin of the beam (or target) or with respect to the charge of the beam. The single spin asymmetry is sensitive to the imaginary part of the interference term while the charge asymmetry is sensitive to the real part.

The DVCS asymmetries can be written as a sum of the four leading-twist GPDs convoluted with the hard scattering propagator. In order to extract the individual GPDs a combination of the DVCS and exclusive meson measurements will need to be used. The deconvolution of the GPDs from the hard scattering propagator will be challenging since the GPDs are functions of more than one variable and an analytical decomposition similar to the DIS situation impossible. The practical way to determine the GPDs will be to model them, evolve them to the appropriate scale, calculate an observable, and compare the calculation to the measured value.

The DVCS process, along with exclusive meson production, will allow access to the GPDs which can provide new information on the structure of the nucleon, including insight into the total angular momentum. The asymmetry measured by HERMES changes sign with the beam polarization as expected and the analyzing power of $-0.23 \pm 0.04(\text{stat})$ $\pm 0.04(\text{sys})$ agrees in magnitude and sign with that of the predictions. The single-beam spin asymmetry has also been confirmed at the CLAS experiment [90], which due to the use of an electron beam, has the expected opposite sign of the asymmetry. The observation provides support for a unique method to extract the DVCS amplitude in challenging but presently attainable kinematic regimes. The measurement of the DVCS process using the asymmetry method is currently being proposed for several experiments, and precise data should become available in the relatively near future.

The HERMES experiment has begun to investigate exclusive processes in terms of the GPDs. For the DVCS process, data has been collected from an unpolarized hydrogen target in 2000, and will increase the statistical precision of the single beam-spin asymmetry when the analysis has been completed. The uncertainty in the beam polarization measurement is reduced for data taken in 1999 and later [86], and other systematic studies are underway, which will improve the systematic precision. In 1998, data were collected using an electron beam and an analysis of a charge asymmetry is in progress. Data from a polarized deuterium target were taken in 1999 and 2000, and can provide access to the BH-DVCS interference term through single beam-spin and target-spin asymmetries. Although the theoretical expectation of asymmetries from such nuclear targets is not yet available, it is assumed that the framework would involve the same GPDs as for the proton. HERMES is also building a detector to measure the recoiled proton to improve the exclusivity of the reactions [78]. The recoil detector will greatly improve the separation of the exclusive events not only for the BH-DVCS analysis, but for other exclusive measurements as well.

In addition to DVCS, exclusive pseudo-scalar and vector meson production has been investigated at HERMES [88, 97, 98] with regards to the GPD formalism. As with the DVCS process, there are more data to be included which will increase the precision of these measurements.

The experiments at HERA continue to improve the measurement of DVCS and other exclusive processes. Spin rotators [23] have been installed on the positron beam line at the collider experiments ZEUS and H1, with the intent of exploring polarized measurements, including exclusive reactions. The investigation of the DVCS process at the collider experiments will contribute to the low-x_{Bj} region of phase space. A direct extraction of the DVCS cross section can be made in addition to polarized asymmetry measurements, which can be of considerable use in differentiating between GPD models.

With the observation of DVCS at JLAB, two experiments are approved to continue the measurement at the beam energy of 6 GeV [99]. In addition, the measurement of DVCS and other exclusive processes are a significant part of the 12 GeV upgrade at JLAB [100]. Assuming the measurements at JLAB are in the appropriate scaling regime and factorization is valid, a significant contribution to the mapping of the GPDs in the relevant kinematic variables (Q^2, t, x, and ξ) will be achieved in the proposed JLAB experiments.

The COMPASS experiment at CERN [21] will use a high energy (up to 200 GeV) muon beam to measure DIS processes. One of the main physics goals is to extract the gluon polarization Δg through the photon-gluon fusion process, detectable in open charm production. In addition, a major exclusive program is proposed at COMPASS to access the GPDs. In particular, DVCS should be directly obtainable, as the BH process is significantly suppressed by the use of a high energy muon beam. Therefore, the COMPASS experiment should be able to help increase our knowledge of the DVCS and other exclusive reactions.

Other proposed experiments, including ELFE [101], TESLA-N [102], and EIC [103], have the potential to study exclusive reactions and are including them as significant parts of their scientific programs. With the inclusion of the present and planned experiments, a major increase in the understanding of the nucleon structure through the GPDs will be obtained, and perhaps aid in the search for a final solution to the spin and flavor structure of the nucleon.

Bibliography

[1] N. Kivel, M. V. Polyakov, and M. Vanderhaeghen, Phys. Rev. D **63** (2001) 114014.

[2] E. Rutherford, Phil. Mag. **21** (1911) 669.

[3] EMC, J. Ashman *et al.*, Phys. Lett. B **206** (1998) 364; Nucl. Phys. B **328** (1989) 1.

[4] P. R. Saull, Zeus Collaboration, hep-ex/0003030.

[5] H1 Collaboration, C. Adloff *et al.*, Phys. Lett. B **517** (2001) 47.

[6] F.E.Close, An Introduction to Quarks and Partons (Academic Press Inc. (London) Ltd., 1979).

[7] N. C. R. Makins [for the HERMES collaboration]. Talk presented at the 8th International Workshop on Deep Inelastic Scattering and QCD (DIS 2000).

[8] K. Goeke, M. V. Polyakov and M. Vanderhaeghen, Prog. Part. Nucl. Phys. **47** (2001) 401.

[9] J. C. Collins, L. L. Franfurt, and M. Strickman, Phys. Rev. D **56** (1997) 2982.

[10] X. Ji, and J. Osborne, Phys. Rev. D **58** (1998) 094018.

[11] A. V. Radyushkin, Phys. Rev. D **58** (1998) 114008; Phys. Rev. D **55** (1997) 7114.

[12] J. C. Collins, and A. Freund, Phys. Rev. D **59** (1999) 074009.

[13] X. Ji, Phys. Rev. Lett. **78** (1997) 610; Phys. Rev. D **55** (1997) 7114.

[14] S. A. Anikin and O. I. Zavialov, Ann. Phys. **135** (1978) 135; B. Geyer *et al.*, Z. Phys. C **28** (1985) 591.

[15] M. Burkardt, Phys. Rev. D **62** (2000) 071503.

[16] P. Kroll, M. Schurmann, and P. A. M. Guichon, Nucl. Phys. A **598** (1996) 435.

[17] A. V. Radyushkin, To be published in the Boris Ioffe Festschrift “At the Frontier of Particle Physics / Handbook of QCD”, edited by M. Shifman (World Scientific, Singapore, 2001) [hep-ph/0101225].

[18] X. Ji, J. Phys. G **24** (1998) 1181.

[19] X. Ji, Phys. Rev. Lett. **78** (1997) 610.

[20] R. L. Jaffe and A. Manohar, Nucl. Phys. B **337** (1990) 509.

[21] “The COMPASS Proposal” G. Baum *et al.*, CERN/SPSLC/96-14 (1996), *http://wwwcompass.cern.ch/compass/publications/ps/proposal.ps.gz.*

[22] G. Bunce, N. Saito, J. Soffer, and W. Vogelsang, Ann. Rev. Nucl. Part. Sci. **50** (2000) 525.

[23] "The Upgraded Interaction Regions of HERA" M. Seidel (2000), *http://desyntwww.desy.de/~ willeke/ir_report.ps.*

[24] R. L. Jaffe, Phil. Trans. Roy. Soc. Lond. A **359** (2001) 391.

[25] P. Hagler and A. Schafer, Phys. Lett. B **430** (1998) 179.

[26] A. Harindranath and R. Kundu, Phys. Rev. D **59** (1999) 116013.

[27] S. V. Bashinsky and R. L. Jaffe, Nucl. Phys. B **536** (1998) 303.

[28] X. Ji, W. Melnitchouk, and X. Song, Phys. Rev. D **59** (1997) 5511.

[29] V. Petrov *et al.*, Phys. Rev. D **57** (1998) 4325.

[30] M. Diehl, T. Feldmann, R. Jakob, and P.Kroll, Eur. Phys. J. C **8** (1999) 409; Nucl.Phys. B **596** (2001) 33; Erratum-ibid. B **605** (2001) 647.

[31] M. Vanderhaeghen *et al.*, Phys. Rev. D **60** (1999) 094017.

[32] A. V. Radyushkin, Acta Phys. Polon. B **30** (1999) 3647.

[33] A. V. Radyushkin, Phys. Lett. B **380** (1996) 417.

[34] M. V. Polyakov and C. Weiss, Phys. Rev. D **60** (1999) 114017.

[35] A.D. Martin, R.G. Roberts, W.J. Stirling, and R.S. Thorne, Eur. Phys. J. C **4** (1998) 463.

[36] M. Penttinen, M. V. Polyakov and K. Goeke, Phys. Rev. D **62** (2000) 014024.

[37] A. Chodos, R. L. Jaffe, K. Johnson, C. B. Thorn, and V. Weisskopf, Phys. Rev. D **9** (1974) 3471.

[38] R. L. Jaffe and X. D. Ji, Phys. Rev. Lett. **67** (1991) 552; X. Song and J. S. McCarthy, Phys. Rev. C **46** (1992) 1077.

[39] I.V. Anikin, *et al.*, hep-ph/0109139.

[40] D. Diakonov, M. Polyakov and C. Weiss, Nucl. Phys. B **461** (1996) 539; D. Diakonov, V. Petrov, P. Pobylitsa, M. Polyakov and C. Weiss, Nucl. Phys. B **480** (1996) 341; P. Pobylitsa and M. Polyakov, Phys. Lett. B **389** (1996) 350; D. Diakonov, V. Petrov, P. Pobylitsa, M. Polyakov and C. Weiss, Phys. Rev. D **56** (1997) 4069.

[41] V. N. Gribov and L. N. Lipatov, Sov. J. Nucl. Phys. **15** (1972). 78; L. N. Lipatov, Sov. J. Nucl. Phys. **20** (1975) 94; G. Altarelli and G. Parisi, Nucl. Phys. B **126** (1977) 298; Yu. L. Dokshitser, Sov. Phys. JETP **46** (1977) 641.

[42] A. V. Efremov and A. V. Radyushkin, Theor. Math Phys. **42** (1980) 97; S. J. Brodsky and G. P. Lepage, Phys. Lett. B **87** (1979) 359.

[43] F. M. Dittes *et al.*, Phys. Lett. B **209** (1988) 325; Fortschr. Phys. **42** (1994) 101; B. Geyer, D. Robaschik, M. Bordag, and J. Horejsi, Z. Phys. C **26** (1985) 591; T. Braunshweig, B. Geyer, J. Horejsi, and D Robaschik, Z. Phys. C **33** (1987) 275; I. Balitsky and V. Braun, Nucl. Phys. B **311** (1989) 541; A. V. Radyushkin, Phys. Lett. B **385** (1996) 333; X. Ji, Phys. Rev. D **55** (1997) 7114.

[44] L. L. Frankfurt, A. Freund, and M. Strickman, Phys. Rev. D **58** (1998) 114001.

[45] P. R. Saull [for the ZEUS Collaboration]. Talk presented at the International Europhysics Conference on High Energy Physics, (EPS HEP01).

[46] A. Donnachie and H. G. Dosch, Phys. Lett. B **502** (2001) 74.

[47] A. V. Belitsky and D. Müller, L. Niedermeier, and A. Schäfer, Nucl. Phys. B **593** (2001) 289.

[48] X. Ji and J. Osborne, Phys. Rev. D **58** (1998) 094018.

[49] A. V. Belitsky, A. Schäefer, Nucl.Phys. B **527** (1998) 235; A. V. Belitsky *et al.*, Phys. Lett. B **474** (2000) 163.

[50] I. V. Anikin, B. Pire and O. V. Teryaev, Phys. Rev. D **62** (2000) 071501.

[51] S. Wandzura and F. Wilczek, Phys. Lett. B **72** (1977) 195.

[52] A. V. Belitsky and D. Müller, Nucl. Phys. B **589** (2000) 611.

[53] N. Kivel and M. V. Polyakov, Nucl. Phys. B **600** (2001) 334.

[54] M. Vanderhaeghen *et al.*, Phys. Rev. C **62** (2000) 025501.

[55] A. V. Belitsky and D. Müller, Phys.Lett. B **507** (2001) 173.

[56] A. A. Solokov and I. M. Ternov, Sov. Phys. Doklady **8** (1964) 1203.

[57] D. P. Barber *et al.*, Nucl. Instr. Meth. A **338** (1994) 166.

[58] D. P. Barber *et al.*, Phys. Lett. B **343** (1995) 436.

[59] D. De Schepper *et al.*, Nucl. Instr. and Meth. A **419** (1998) 16.

[60] J. Stewart, Proc. of the 7th International Workshop on Polarized Gas Targets and Polarized Beams, Urbana-Champaign, AIP Conf. Proc **421** (1997) 96.

[61] C. Baumgarten *et al.* Nucl. Instr. and Meth. A, NIMA 41274 (in press); C. Baumgarten *et al.* Eur. Phys. J. D **18** (2002) 37; H. Kolster, *The HERMES Gaseous Internal Polarized Proton Target and its use in the HERA Positron Storage Ring*, PhD thesis, Ludwig-Maximilians-Universität München (1998).

[62] Hermes Collaboration, K. Ackerstaff, *et al.*, Nucl. Instr. and Meth. A **417** (1998) 230.

[63] M. Kobayashi *et al.*, KEK Internal Report **93-178** (1993).

[64] H. Avakian, *et al.*, Nucl. Instr. and Meth. A **417** (1998) 69.

[65] T. Benisch *et al.*, Nucl. Instr.and Meth. A **471** (2001) 314; T. Benisch, "Polarisierte Bhabha-Streuung und Luminositätsmessung im HERMES-Experiment", PhD thesis, Universität Erlangen-Nürnberg (1998).

[66] CERN-CN Division, *EPIO-Experimental Physics Input Output Package*, CERN Program Library, Long Writeup I101, CERN (1993).

[67] W. Wander et al., *DAD-Distributed Adamo Database System at HERMES*, Proc. of the International Conference on Computing in High Energy Physics, CHEP 95, Rio de Janeiro, (1995).

[68] CERN-CN Division, CERN PTG, Programming Techniques Group, *ADAMO-Entity-Relationship Programming System, Version 3.3*, CERN (1993), *http://www1.cern.ch/Adamo/*.

[69] W. Wander, *Reconstruction of High Energy Scattering Events in the HERMES Experiment*, PhD thesis, Friedrich-Alexander-Universität Erlangen-Nürnberg, Translated by M. Averesch and R. Kaiser, (1996).

[70] H. Avakian, *et al.*, HERMES Internal Report **97-038** (1997).

[71] M. Dueren, P. Geiger, N. Makins, E. Volk *et al.*, *The HERMES Monte Carlo Program*, *http://hermes.desy.de/hmc/*.

[72] G. Ingelman, A. Edin, and J. Rathsman, Comp. Phys. Comm. **101** (1997) 108.

[73] M. Maul, *The PEPSI Page - Polarized Electron-Proton Scattering Interactions*, *http://shakespeare.thep.lu.se/~ maul/pepsi.html*.

[74] T. Sjöstrand, Comp. Phys. Comm. **82** (1994) 74.

[75] B. Andersson, G. Gustafson, G. Ingelman, and T. Sjöstrand, Phys. Rep. **97** (1983) 31.

[76] I. Akushevich, H. Boettcher, and D. Ryckbosch, *RADGEN 1.0. Monte Carlo Generator for Radiative Events in DIS on Polarized and Unpolarized Targets* Talk presented at the Workshop "Monte Carlo Generators for HERA Physics", Hamburg, hep-ph/9906408, (1999).

[77] CERN-CN Division, *GEANT - Detector Description and Simulation Tool*, CERN Program Long Writeup W5013, CERN (1993).

[78] "A Large Acceptance Recoil Detector for HERMES", DESY PRC 01-01 (2001), *http://www-hermes.desy.de/~ kai/recoil/recoil/recoil.html*.

[79] M. Tytgat, *Diffractive Production of ρ^0 and ω Vector Mesons at HERMES*, PhD Thesis, Universiteit Gent (2001).

[80] P. Di Nezza and N. Bianchi, *Pion Electroproduction in Deep Inelastic Scattering*, HERMES Internal Report 99-047 (1999).

[81] L. Bugge, Nucl. Instr. and Meth. A **242** (1986) 228.

[82] T.C. Awes, *et al.*, Nucl. Instr. and Meth. A **311** (1992) 130.

[83] B. Surrow, DESY Thesis **1998-004** (1998).

[84] D. Besset *et al.*, Nucl. Instr. and Meth. **166** (1979) 515.

[85] HERMES Collaboration, A. Airapetian *et al.*, Phys. Lett. B **422** (1998) 484.

[86] M. Beckmann *et al.*, Nucl. Instr. Meth. (2001), in press, [physics/0009047].

[87] E. Thomas, *Single Spin Azimuthal Asymmetries in Electroproduction of Exclusive* π^+, 9th International Workshop on Deep Inelastic Scattering and QCD (DIS 2001), Bologna, Italy (2001).

[88] HERMES Collaboration, A. Airapetian *et al.*, Phys. Rev. D **64** (2001) 097101.

[89] L.L. Frankfurt, M.V. Polyakov, and M. Strikman, *$N \to$ Delta DVCS, exclusive DIS processes and skewed quark distributions in large N_c limit* ,
Contribution to the Workshop "Jefferson Lab Physics and Instrumentation with 6-12 GeV Beams", Newport News, VA, hep-ph/9808449, (1998).

[90] CLAS Collaboration, S. Stepanyan *et al.*, Phys. Rev. Lett. **87** (2001) 182002.

[91] R. Mertig and W. L. van Neerven, Z. Phys. C **70** (1996) 637; W. Vogelsang, Nucl. Phys. B **475** (1996) 47.

[92] N. Mathur, S. J. Dong, K. F. Liu, L. Mankiewicz, and N. C. Mukhopadhyay, Phys. Rev. D **62** (2000) 114504.

[93] I. I. Balitsky, and X. Ji, Phys. Rev. Lett. **79** (1997) 1225.

[94] HERMES Collaboration, K. Ackerstaff *et al.*, Phys. Lett. B **464** (1999) 123.

[95] Y. Goto, *et al.*, Phys. Rev. D **62** (2000) 034017.

[96] HERMES Collaboration, A. Airapetian, *et al*, Phys. Rev. Lett. **87** (2001) 182001.

[97] HERMES Collaboration, A. Airapetian *et al.*, Phys. Rev. Lett. **84** (2000) 4047.

[98] HERMES Collaboration, A. Airapetian *et al.*, Phys. Lett. B **513** (2001) 301.

[99] "Deeply Virtual Compton Scattering with CLAS at 6 GeV", (2001),
http://www.jlab.org/exp_prog/proposals/01/PR01-113.pdf.

[100] "The Science Driving the 12 GeV Upgrade of CEBAF" (2000),
http://www.jlab.org/div_dept/physics_division/GeV.html.

[101] "ELFE at CERN" ed. H. Burkhardt, CERN 99-10 (1999),
http://hbu.home.cern.ch/hbu/Elfe/Elfe.html;
"ELFE@DESY" (1997), *http://www.desy.de/lc-cdr/elfe.ps.*

[102] Chapter 3 of the Tesla TDR Appendices, eds. R. Kaiser and W.-D. Nowak, (2001),
http://tesla.desy.de/new_pages/TDR_CD/PartVI/append.html/chapter3.pdf.

[103] "The Electron Ion Collider", BNL 68933 (2002),
http://www.phenix.bnl.gov/WWW/publish/abhay/Home_of_ EIC.

Appendix A

Multiplication of Fourier Series

Assuming only azimuthal angle (ϕ) dependence, the normalized cross-section and acceptance function can each be expanded in a (normalized) Fourier series:

$$\begin{aligned}
\sigma(\phi) &= 1 + \sum_m \left(a_m \cos m\phi + b_m \sin m\phi\right) , \\
\epsilon(\phi) &= 1 + \sum_m \left(A_m \cos m\phi + B_m \sin m\phi\right) .
\end{aligned}$$

The product of the two normalized Fourier series can then be written as a single Fourier series:

$$\begin{aligned}
\sigma\epsilon =& \\
& 1 + \frac{1}{2}\sum_m \left(A_m a_m + B_m b_m\right) + \\
& \cos\phi \left[a_1 + A_1 + \frac{1}{2}\sum_m \left(A_m a_{m+1} + a_m A_{m+1} + B_m b_{m+1} + b_m B_{m+1}\right) \right] + \\
& \cos 2\phi \left[\begin{array}{c} a_2 + A_2 + \frac{1}{2}\sum_m \left(A_m a_{m+2} + a_m A_{m+2} + B_m b_{m+2} + b_m B_{m+2}\right) \\ +\frac{1}{2}(A_1 a_1 - B_1 b_1) \end{array} \right] + \\
& \cos 3\phi \left[\begin{array}{c} a_3 + A_3 + \frac{1}{2}\sum_m \left(A_m a_{m+3} + a_m A_{m+3} + B_m b_{m+3} + b_m B_{m+3}\right) \\ +\frac{1}{2}(A_1 a_2 + A_2 a_1 - B_1 b_2 - B_2 b_1) \end{array} \right] + \\
& \sin\phi \left[b_1 + B_1 + \frac{1}{2}\sum_m \left(A_m b_{m+1} - b_m A_{m+1} - B_m a_{m+1} + a_m B_{m+1}\right) \right] + \\
& \sin 2\phi \left[\begin{array}{c} b_2 + B_2 + \frac{1}{2}\sum_m \left(A_m b_{m+2} - b_m A_{m+2} - B_m a_{m+2} + a_m B_{m+2}\right) \\ +\frac{1}{2}(A_1 b_1 + B_1 a_1) \end{array} \right] + \\
& \sin 3\phi \left[\begin{array}{c} b_3 + B_3 + \frac{1}{2}\sum_m \left(A_m b_{m+3} - b_m A_{m+3} - B_m a_{m+3} + a_m B_{m+3}\right) \\ +\frac{1}{2}(A_1 b_2 + A_2 b_1 + B_1 a_2 + B_2 a_1) \end{array} \right] + \\
& \ldots
\end{aligned}$$